CIRCUIT AND NEURON TYPE-SPECIFIC ROLES FOR UBE3A IN THE VISUAL CORTEX

Michael L. Wallace

A dissertation submitted to the faculty at the University of North Carolina at Chapel Hill in partial fulfillment of the requirements for the degree of Doctor of Philosophy in the Curriculum of Neurobiology of the School of Medicine.

Chapel Hill
2014

Approved by:

Thomas L. Kash

Paul B. Manis

A. Leslie Morrow

Benjamin D. Philpot

Richard J. Weinberg

ABSTRACT

Michael L. Wallace: Circuit and neuron type-specific roles for Ube3a in the visual cortex
(Under the direction of Benjamin D. Philpot)

Balanced excitation and inhibition is critical for normal circuit function and disruptions in excitation-to-inhibition (E/I) balance have been shown to exist in many neurological disorders. One such disorder, autism, has been hypothesized to result from genetic and/or environmental insults that cause an E/I imbalance in key neural circuits/systems. Angelman syndrome (AS) is an autism spectrum disorder distinguished by severe intellectual disabilities, EEG abnormalities, gait disturbances, disrupted sleep patterns, profound language impairment, and seizures. AS is caused by deletions or loss-of-function mutations in the maternally inherited allele of *UBE3A*. Similar to humans with AS, AS model mice lacking the maternal *Ube3a* allele exhibit behavioral changes mirroring the hallmarks of the syndrome, including abnormal EEG patterns, elevated seizure susceptibility, and difficulty with movement and balance. Seizures are believed to be extreme manifestations of E/I imbalance, therefore we hypothesized that there existed an E/I imbalance in cortical circuits in AS model mice.

We investigated excitatory and inhibitory neurotransmission in the visual cortex and found an inhibitory deficit that may arise from defective presynaptic vesicle cycling in multiple interneuron populations. The inhibitory defect is specific to inputs into excitatory neurons as neurotransmission onto inhibitory neurons is normal. Excitatory

neurotransmission onto excitatory neurons are also decreased but to a smaller degree leading to an E/I imbalance in cortical circuits.

We then sought to determine the neuron type-specific requirements for Ube3a in regulating E/I imbalance. We used mice harboring a conditional *Ube3a* allele to show that deleting Ube3a from all inhibitory neurons resulted in none of the synaptic phenotypes observed when *Ube3a* was deleted from all neurons. Furthermore, when we deleted *Ube3a* from cortical excitatory neurons we observed only defects in evoked inhibition. These findings suggest Ube3a loss is required both pre and postsynaptically for several synaptic phenotypes contributing to E/I imbalance observed in AS model mice.

Together, these studies identify a synaptic mechanism underlying E/I imbalance in cortical circuits and may lead to more effective treatments for seizures in AS.

To my parents who have always encouraged me to be creative and use my imagination.

ACKNOWLEDGEMENTS

First and foremost I would like to thank my advisor and mentor Ben Philpot. Ben has the unique ability to create a working environment that is fun as well as scientifically rigorous. Ben has always encouraged me when I have proposed difficult experiments and even more so when the data comes back without the result I was hoping for. Ben also implored me to apply to the Marine Biological Lab for a summer course. Attending the Neural Systems and Behavior course at MBL truly expanded my scientific knowledge base and inspired me to pursue a postdoc position in a completely different brain region. It has been a pleasure working in Ben's lab and learning how to become a scientist.

Additionally, the Philpot lab has been an integral part of my growth as a scientist. Working closely with Matt Judson, Rylan Larsen, Adam Roberts, Hsien-Sung Huang, Janet Berrios, Thorfinn Riday, Portia Kunz, Maile Henson, Jaya Miriyala, Hanji Han, Andy Burns, Courtney Thaxton, Angie Mabb, Kelly Jones, Kelly Carstens, and Bram Kuijer has been fun and rewarding, I thank you for all of your support.

I would also like to thank the members of my committee Richard Weinberg, Paul Manis, Leslie Morrow, and Tom Kash. Our discussions and meetings have always been extremely fruitful and have helped steer my research in the best direction. Additionally, the faculty of the Neural Systems and Behavior course especially Michael

Brecht, Ron Calabrese, Michael Dickenson, and Gaby Maimon. You all showed me how fun and creative science can be.

I also thank my family, Mom, Dad, Bri, Katie and Kristen for all of their support and encouragement over the years. Finally, I would like to thank Janet Berrios for all of her support and encouragement during the many long days and nights of graduate school. It would have been way less fun without you by my side.

TABLE OF CONTENTS

LIST OF FIGURES

LIST OF TABLES

LIST OF ABBREVATIONS

AMPA	α-Amino-3-hydroxy-5-methyl-4-isoxazolepropionic acid
Arc	Activity-regulated cytoskeleton-associated protein
AS	Angelman syndrome
CCV	Clathrin-coated vesicles
DNA	Deoxyribonucleic acid
E/I	Excitatory-to-inhibitory
ECoG	Electrocorticograph, Electrocorticography
EEG	Electroencephalograph, Electroencephalography
eIPSC	evoked inhibitory postsynaptic current
FMR1/Fmr1	Fragile X mental retardation 1 gene
FMRP/Fmrp	Fragile x mental retardation protein
FS	Fast-spiking
FXS	Fragile X syndrome
GABA	Gamma-aminobutyric acid
GABAR	Gamma-aminobutyric acid receptor
GFP	Green fluorescent protein
KO	Knockout
L2/3	Layer 2/3
L4	Layer 4
L5	Layer 5
M1	Primary motor cortex
MECP2/Mecp2	Methyl CpG binding protein 2

mEPSC	miniature excitatory post-synaptic current
mIPSC	miniature inhibitory postsynaptic current
PV	Parvalbumin
RNA	Ribonucleic acid
RTT	Rett syndrome
S1	Primary somatosensory cortex
UBE3A/Ube3a	Ubiquitin protein ligase 3A
V1	Primary visual cortex
VGAT	Vesicular gamma-aminobutyric acid transporter
WT	Wild-type

CHAPTER 1: EXCITATORY/INHIBITORY BALANCE IN NEURODEVELOPMENTAL DISORDERS

1.1 Introduction

The neurodevelopmental disorder autism is characterized by impaired social interactions and communication, and by restricted or repetitive/stereotyped behaviors (American Psychiatric Association, 2013). There is no single genetic cause of autism; therefore neurobiologists have searched for common neural mechanisms that may encompass much of the genetic heterogeneity. A leading hypothesis suggests that autism results from genetic and/or environmental insults that cause an imbalance in the excitation-to-inhibition (E/I) ratio in key neural circuits and systems (Rubenstein and Merzenich, 2003). Balance between excitation and inhibition in neural circuits is essential for efficient and accurate information transfer and processing. In highly interconnected circuits, excess excitation can lead to seizure or epileptic activity, while excess inhibition can halt the exchange and propagation of a signal. To limit these two extremes, powerful homeostatic mechanisms exist to keep the E/I balance in a restricted range (Marder and Goaillard, 2006; Turrigiano and Nelson, 2004). Therefore, in order for an E/I imbalance to become manifest, there must be an insult(s) so severe that homeostatic mechanisms cannot overcome the initial circuit imbalance or, the insult impairs the homeostatic mechanisms directly.

In support of the E/I imbalance hypothesis, several mouse models of autism have

E/I imbalance in neural circuits (Bateup et al., 2013; Dani et al., 2005; Gibson et al., 2008; Tabuchi et al., 2007; Wallace et al., 2012). Also, recent studies have shown that disrupting E/I balance alone in cortical circuits can produce social behavior abnormalities in mice (Yizhar et al., 2011). Cortical circuits in particular are believed to control the higher order cognitive processes and behaviors several of which are affected in autism (Dichter, 2012). Finally, seizures are commonly comorbid with autism diagnosis suggesting an elevated E/I ratio (Leung and Ring, 2013; Tuchman et al., 2010). Here I will review the evidence for E/I imbalance in several mouse models of autism spectrum disorder with a primary focus on cortical circuits. Specifically, I will discuss Fragile X, Rett, and Angelman syndromes which are all monogenetic neurodevelopmental disorders on the autism spectrum. I will then compare common cellular and synaptic mechanisms that lead to E/I imbalance and what may be their effects on behavior.

1.2 Fragile X Syndrome

Fragile X syndrome (FXS) is the most common monogenetic form of autism and is caused by transcriptional silencing of the *FMR1* gene (Bassell and Warren, 2008). *FMR1* codes for FMRP, a RNA binding protein involved in translational regulation of specific target RNAs. FXS patients are characterized by cognitive and social defects, seizures, hypersensitivity and hyperactivity (Hagerman et al., 2009). Many of these characteristics are reproduced in the mouse model for FXS, the *Fmr1* knockout (KO) mouse (Musumeci et al., 2000; Nielsen et al., 2002; Spencer et al., 2005). Most of the studies I will discuss here were performed on male *Fmr1* knockout mice (*Fmr1*$^{-/y}$), which lack *Fmr1* from all neurons (Bakker et al., 1994).

Defects in excitatory synaptic structure and transmission were some of the first synaptic defects to be described in *Fmr1* KO mice (Bureau et al., 2008; Comery et al., 1997; Nimchinsky et al., 2001). L5 pyramidal neurons have supernumerary spines in *Fmr1* KO mice and they are also longer than spines from controls (Comery et al., 1997). It is hypothesized that long, thin spines arise from excessive long-term depression in *Fmr1* KO mice, while increased spine density maintains hyperconnectivity and circuit hyperexcitability (Huber et al., 2002). Additionally, regulation of excitatory synapse strength and number was shown to be cell autonomous, regulated by FMRP in the postsynaptic pyramidal neuron (Pfeiffer and Huber, 2007). Elegant paired electrophysiological recordings went on to show that excitatory inputs onto fast-spiking inhibitory interneurons were weaker in *Fmr1* KO leading to deficient recruitment of inhibition in the cortex (Gibson et al., 2008). Furthermore, defects in excitatory inputs were due to a cell-autonomous decrease in multivesicular release (Patel et al., 2013).

Defects in excitatory transmission likely lead to abnormally long periods of increased cortical network activity or “UP states” observed both in vitro and in vivo in the *Fmr1* KO (Goncalves et al., 2013; Hays et al., 2011). Moreover, in vivo, within an UP state the network was more synchronous in *Fmr1* KO mice indicating a developmental delay in cortical desynchronization, likely reflecting weak engagement of the inhibitory network (Goncalves et al., 2013; Paluszkiewicz et al., 2011). Therefore, through in vitro and in vivo electrophysiology there is strong evidence for E/I imbalance in cortical circuits in *Fmr1* KO mice. In support of an E/I imbalance favoring excitation, *Fmr1* KO mice exhibit robust seizure activity (Yan et al., 2004). Audiogenic seizures, a model of generalized seizure, are the most common method used to evoke seizures in this model

and audiogenic seizures are present on FVB, C57BL/6J, and hybrid backgrounds (Osterweil et al., 2013; Ross and Coleman, 2000; Yan et al., 2004). Together, accumulated evidence suggest FXS mouse models show a strong E/I imbalance in cortical circuits that likely contributes to defects in cortical processing, seizures, and cognitive dysfunction.

1.3 Rett Syndrome

Rett syndrome (RTT) is a postnatal neurodevelopmental disorder that affects predominately girls (Chahrour and Zoghbi, 2007). The causative gene, *MECP2*, is X-linked and results in mosaicism for the *MECP2* mutation in affected girls (Amir et al., 1999). *MECP2* codes for MeCP2 a transcription repressor that recognizes and binds methylated DNA (Lewis et al., 1992). Decreased levels of MeCP2 results in dysregulation of MeCP2 target genes and the onset of RTT symptoms at 6 to 18 months (Nomura, 2005). Prominent features of RTT include stereotypies, ataxia, seizures, autonomic dysfunction and intellectual disability. Several mouse models of RTT (*Mecp2* knockout mice) have been generated and recapitulate many of the behaviors seen in humans including hypoactivity, seizures, ataxia, early death and learning and memory impairments (Chahrour and Zoghbi, 2007). Most of the studies I will discuss here were performed on male *Mecp2* knockout mice (*Mecp2*$^{-/y}$) which lack *Mecp2* from all neurons (Chen et al., 2001).

Mecp2 knockout mice have been reported to have an E/I imbalance in cortical circuits in several studies (Chao et al., 2010; Dani et al., 2005; Durand et al., 2012). This imbalance strongly favors inhibition and is likely to contribute largely to cognitive and perceptual impairments in *Mecp2* knockout mice. Decreased excitatory and

increased inhibitory neurotransmission was first described in L5 pyramidal neurons of primary somatosensory cortex of *Mecp2* knockout mice. This was shown to lead to decreased spontaneous action potential firing in vitro and decreased connectivity of excitatory circuits (Dani et al., 2005; Dani and Nelson, 2009). In addition, it is likely that decreased excitation in cortex arises from reduced numbers of excitatory synapses as spine densities have been shown to be reduced in multiple brain regions in *Mecp2* knockout mice (Fukuda et al., 2005; Stuss et al., 2012).

Recent studies using laser scanning photostimulation in primary motor cortex have shown decreased excitatory connectivity may be due to loss of Mecp2 in the postsynaptic neurons alone. Mapping of excitatory inputs demonstrated that knocking down Mecp2 in a sparse population of L2/3 pyramidal neurons resulted in decreased ascending excitatory inputs from L3 and L5A onto knockdown neurons, but not neighboring controls (Wood et al., 2009).

The first in vivo evidence of E/I imbalance favoring inhibition came from studies of neuronal firing patterns in L2/3 of visual cortex (Durand et al., 2012). In vivo recordings from multiunit electrodes showed that both spontaneous and evoked spiking rates were reduced in *Mecp2* knockout mice leading to a change in signal-to-noise ratio. Interestingly, studies in the visual cortex indicate increased inhibition from parvalbumin (PV) containing inhibitory neurons is the primary contributor to E/I imbalance due to increased PV+ puncta in *Mecp2* knockout mice (Durand et al., 2012). Details concerning the underlying functional synaptic defect at inhibitory synapses in *Mecp2* knockout mice remain to be investigated.

Collectively, Mecp2 loss in all neurons results in an E/I imbalance that favors

inhibition and reduced cortical firing rates, however, depending on the cortical region (S1, M1, or V1) the underlying synaptic cause may differ. Therefore, it was particularly surprising when it was shown that deleting *Mecp2* in only GABAergic neurons using an *Mecp2* floxed allele was sufficient to produce all of the behavioral phenotypes observed in the *Mecp2* knockout mice (Chao et al., 2010). Additionally, mice where *Mecp2* was deleted from only GABAergic neurons showed decreased inhibition, but no change in excitation onto L2/3 pyramidal neurons in S1. These findings demonstrate that deleting *Mecp2* from inhibitory neurons alone results in completely different inhibitory synaptic phenotypes than deletion of *Mecp2* in all neurons. It also raises questions concerning how homeostatic/compensatory mechanisms may contribute to synaptic abnormalities seen in *Mecp2* knockout mice. These data suggest that defective cortical excitatory neurotransmission may not be a requirement for any of the RTT behavioral phenotypes to manifest. It will be of great interest to assay inhibitory and excitatory inputs onto GABAergic neurons in mice where *Mecp2* is deleted in only GABAergic neurons as it will give a clearer picture of E/I balance in the circuit/network. Clearly, the precise contribution of disrupted E/I balance to RTT behavioral phenotypes is complex and will require more subtle manipulation of *Mecp2* in both excitatory and inhibitory neurons to fully clarify the contribution of Mecp2 to excitatory and inhibitory synapse function.

1.4 Angelman Syndrome

Angelman syndrome (AS) is a severe neurodevelopmental disorder characterized by cognitive disability, seizures, absence of speech, and high comorbidity with autism (Williams et al., 2006). Maternal deletions of chromosome 15q11-q13 and mutations specific to *UBE3A*, which lies within that region, cause AS (Kishino et al.,

1997). *UBE3A* is imprinted and expressed exclusively from the maternally inherited chromosome in both humans and mice (Rougeulle et al., 1997). Interestingly, *Ube3a* seems to be exclusively imprinted in neurons where strong repression of the paternal allele occurs postmitotically (Judson et al., 2013). Glia and other tissues express *Ube3a* biallelically and the effect of maternal *Ube3a* deletion on these cells is unknown (Judson et al., 2013). However, it is important to note that mice that lack *Ube3a* from the paternal allele (*Ube3a*$^{m+/p-}$) and are therefore heterozygous for *Ube3a* in glia and other tissues but have normal levels of Ube3a in neurons present no observable behavioral phenotypes compared to controls, indicating that loss of Ube3a in neurons is required for AS phenotypes (Jiang et al., 1998; Miura et al., 2002). Ube3a has several known functions, one as an E3 ubiquitin ligase that targets substrate proteins and marks them for proteosomal degradation (Scheffner et al., 1993), and the other as a transcriptional co-activator functioning primarily in the nucleus (Kuhnle et al., 2013; Ramamoorthy and Nawaz, 2008). However, the extent to which Ube3a acts in either or both of these capacities in neurons is largely unknown (Mabb et al., 2011). A mouse model of AS was generated in 1998 harboring a *Ube3a* null allele on the maternally inherited chromosome (Jiang et al., 1998). It recapitulates the major phenotypes seen in AS including ataxia, motor dysfunction, seizures, and cognitive disabilities (Jiang et al., 1998).

Ube3a null mice were first recognized to have defects in excitatory neurotransmission in the cortex with the report of reductions in dendritic spine density in L2/3 and L5 pyramidal neurons (Sato and Stryker, 2010; Yashiro et al., 2009). Spontaneous excitatory neurotransmission was also found to be reduced in *Ube3a* null

mice indicating a functional loss of excitatory synapses in L2/3 pyramidal neurons of V1 (Yashiro et al., 2009). Additionally, it was found that the Activity-regulated cytoskeleton-associated protein (Arc), a protein involved in AMPA receptor internalization, was increased in *Ube3a* null mice, providing a possible molecular mechanism underlying reduced excitatory synapse number (Greer et al., 2010).

While multiple studies reported decreased excitatory connectivity, *Ube3a* null mice have seizures that have been detected with cortical EEG/ECoG recordings, suggesting that epileptic activity, at a minimum, spreads to the cortex (Jiang et al., 1998; Miura et al., 2002). Therefore, we began an investigation to determine if cortical inhibition was altered in *Ube3a* null mice (Wallace et al., 2012). We found that both spontaneous and evoked inhibitory neurotransmission was reduced onto L2/3 pyramidal neurons. Conversely, both excitation and inhibition onto PV+ inhibitory neurons was normal in *Ube3a* null mice compared to controls. Defects in inhibitory neurotransmission seemed to be due, at least in part, to defects in synaptic vesicle cycling. This was supported by anatomical methods showing increases in clathrin-coated vesicles specifically at inhibitory axon terminals in *Ube3a* null mice, compared to controls. Electrophysiological recordings then determined that synaptic recovery from high frequency stimulation did not return to control levels at inhibitory synapses in *Ube3a* null mice (Wallace et al., 2012). We concluded from these studies that there existed an E/I imbalance in the cortex favoring excitation that would permit seizure propagation and hyperexcitability.

Having identified a circuit with E/I imbalance we then sought to determine the neuron type specific requirements of Ube3a loss for these synaptic phenotypes. In

order to manipulate *Ube3a* in neuron class specific manner we generated a conditional *Ube3a* knockout mouse (*Ube3a*^{Flox}). We then crossed this mouse line with lines expressing Cre in either GABAergic neurons (*Gad2-Cre*) or pyramidal neurons (*NEX-Cre*). Surprisingly, we saw no synaptic defects when we deleted *Ube3a* in GABAergic neurons, and only detected defects in evoked inhibition when we deleted *Ube3a* from pyramidal neurons. We conclude that for many of the synaptic phenotypes observed in AS model mice, Ube3a loss is required both pre and postsynaptically to cause the synaptic defect and resulting E/I imbalance.

1.5 Common mechanisms of E/I imbalance in autism

In each of the mouse models reviewed above there exists an E/I imbalance in cortical circuits. In both Fragile X and Angelman syndrome mouse models this imbalance favors excitation, while in Rett syndrome mouse models the balance is tipped towards inhibition (Dani et al., 2005; Durand et al., 2012; Patel et al., 2013; Wallace et al., 2012). Therefore, while all mouse models exhibit E/I imbalance, the underlying synaptic mechanisms in each model differ significantly. It is important to note that all of the reports of E/I imbalance in these mouse models arise from assaying excitatory and inhibitory neurotransmission onto excitatory and inhibitory neurons. Changes in intrinsic excitability can also strongly alter E/I balance and have been reported in these mouse models, but have yet to be rigorously tested in multiple cell classes in cortex (Dani et al., 2005; Gibson et al., 2008; Routh et al., 2013; Wallace et al., 2012). Additionally, investigators have focused on different cortical layers and microcircuits in these different mouse models (L2/3 for AS, L4 for FXS, and L5 for RTT) further complicating direct comparisons.

However, similarities in the synaptic defects leading to E/I imbalance do exist. In all three mouse models significant defects in excitatory neurotransmission are present resulting in decreased excitatory-to-excitatory connectivity (Bureau et al., 2008; Dani et al., 2005; Yashiro et al., 2009). In *Mecp2* knockout mice decreased excitation is accompanied by an increase in inhibition resulting in a "silent" cortex (Dani et al., 2005; Durand et al., 2012). Conversely, excitatory-to-inhibitory connections in *Fmr1* knockout mice are decreased leading to a reduction in inhibitory activity and a hyperexcitable circuit exhibiting increased local network activity (Goncalves et al., 2013; Patel et al., 2013). Finally, in *Ube3a* maternal null mice inhibitory-to-excitatory connections are themselves impaired due to defective synaptic vesicle cycling (Wallace et al., 2012). The precise impact that the synaptic defects in the *Ube3a* maternal null mice have on local network excitability *in vivo* remain unknown. Together, it seems that inhibition, rather than excitation, determines whether the E/I ratio favors excitation (*Fmr1* KO and *Ube3a* KO) or inhibition (*Mecp2* KO). Obviously, the autism community would benefit greatly from comparative studies of the mouse models discussed here. For example, would local network activity (UP/DOWN states) correlate the direction of E/I imbalance in different mouse models? If so, one would expect network activity to be modulated in the same direction as FXS in AS, and in the opposite direction in RTT. Studies examining such processes in multiple mouse models may help draw more parallels between the effects of synaptic E/I imbalance on local network activity and eventually behavior.

While excitatory and inhibitory synaptic defects have been observed in these mouse models of neurodevelopmental disorders, major unanswered questions

regarding the relationship between inhibitory and excitatory synaptic defects are only now beginning to be addressed. Studies employing conditional knockout mouse lines are particularly useful in determining cell class-specific or cell-autonomous synaptic defects. Surprising results in both the Fragile X and Rett syndrome fields have already exposed the importance of conditional manipulations of the gene of interest (Chao et al., 2010; Patel et al., 2013). Conditional manipulations of gene expression are of particular importance in these mouse models as they may help circumvent the indirect effects seizure activity can have on synaptic transmission and homeostatic processes (Cossart et al., 2001; Kumar and Buckmaster, 2006; Sloviter, 1987). The development of conditional *Ube3a* mouse lines, as well as more selective and precise temporal and regional manipulations of *Fmr1* and *Mecp2,* is sure to elucidate the complex role for these genes in synaptic transmission, plasticity, and E/I balance.

1.6 Outcomes of E/I imbalance in cortical circuits

While it is clear that E/I imbalance exists in several mouse models of neurodevelopmental disorders, major questions remain concerning the actual impact E/I imbalance has on the autistic like behaviors. With the advent of optical and chemical genetic means of circuit activity manipulation these questions may finally be able to be addressed. For example, if a synaptic imbalance exists, such as in *Mecp2* knockout mice, where cortical circuits are hypoexcitable, and a cortical computation, such as orientation tuning in the visual cortex, is defective, does restoring optimal excitability in the circuit rescue defects in the cortical computation (Durand et al., 2012)? Optogenetics allow modulation of E/I balance in real-time, and when combined with

quantitative imaging and behavioral techniques, direct relationships between E/I balance and behavior can begin to be tested (Guo et al., 2014; Yizhar et al., 2011).

Seizures have one of the highest comorbidities with autism and are often described as extreme manifestations of E/I imbalance (Tuchman et al., 2010). Seizure activity is almost always recorded using scalp EEG, whose signal comes from upper cortical layers (Buzsaki et al., 2012). However, how cortical E/I balance affects seizure susceptibility has never been directly tested. Clearly, cortical circuit imbalance in autism is permissive to cortical seizure activity, but whether it is the source remains an open question. In order to understand seizure susceptibility in autism, the relevant circuits must be identified first, then more detailed analysis of those circuits will provide insights into the relationship between E/I balance autism and seizures. Finally, when the primary underlying circuit defect is well understood, and the impact of rescuing E/I imbalance is realized, more precise effective strategies for treatment of E/I imbalance in patients with neurodevelopmental disorders will result.

CHAPTER 2: MATERNAL LOSS OF *UBE3A* PRODUCES AN EXCITATORY/INHIBITORY IMBALANCE THROUGH NEURON TYPE-SPECIFIC SYNAPTIC DEFECTS[1]

2.1 Overview

Angelman syndrome (AS) is a neurodevelopmental disorder caused by loss of the maternally inherited allele of *UBE3A*. AS model mice, which carry a maternal *Ube3a* null mutation (*Ube3a*$^{m-/p+}$), recapitulate major features of AS in humans, including enhanced seizure susceptibility. Excitatory neurotransmission onto neocortical pyramidal neurons is diminished in *Ube3a*$^{m-/p+}$ mice, seemingly at odds with enhanced seizure susceptibility. We show here that inhibitory drive onto neocortical pyramidal neurons is more severely decreased in *Ube3a*$^{m-/p+}$ mice. This inhibitory deficit follows the loss of excitatory inputs and appears to arise from defective presynaptic vesicle cycling in multiple interneuron populations. In contrast, excitatory and inhibitory synaptic inputs onto inhibitory interneurons are largely normal. Our results indicate that there are neuron type-specific synaptic deficits in *Ube3a*$^{m-/p+}$ mice despite the presence of Ube3a in all neurons. These deficits result in

---

[1] This chapter was previously published with Alain C. Burette, Richard J. Weinberg, and Benjamin D. Philpot in *Neuron* (2012) June; 7;74(5):793-800.

excitatory/inhibitory imbalance at cellular and circuit levels and may contribute to seizure susceptibility in AS.

2.2 Introduction

Angelman syndrome (AS) is characterized by severe intellectual disabilities, EEG abnormalities, gait disturbances, disrupted sleep patterns, profound language impairment, and autism (Williams et al., 2006). Seizures are present in 90% of AS patients, significantly impacting their quality of life and that of their caregivers (Thibert et al., 2009). AS is caused by deletions or loss-of-function mutations in the maternally inherited allele of *UBE3A* (Rougeulle et al., 1997). *UBE3A* encodes an E3 ubiquitin ligase that, in the brain, is expressed primarily from the maternal allele as a result of neuron-specific imprinting (Albrecht et al., 1997). Similar to humans with AS, mice lacking maternal *Ube3a* (*Ube3a*$^{m-/p+}$) have abnormal EEG activity and are susceptible to cortical seizures, suggesting that loss of Ube3a might disrupt the excitatory/inhibitory balance in the neocortex (Jiang et al., 1998).

Loss of maternally inherited *Ube3a* results in decreased excitatory synaptic drive onto pyramidal neurons in layer 2/3 (L2/3) of neocortex, as evidenced by a loss of dendritic spines (Yashiro et al., 2009). Decreased Ube3a-mediated proteasomal degradation of Arc and Ephexin5 proteins may lead to excitatory synaptic defects (Greer et al., 2010; Margolis et al., 2010). These observations suggest a mechanism for how the loss of Ube3a may cause fewer and/or weaker excitatory synapses. While these deficits may be relevant to cognitive phenotypes in *Ube3a*$^{m-/p+}$ mice, they would not on their own predict hyperexcitability and increased seizure susceptibility. We

hypothesized that Ube3a loss results in more severe inhibitory deficits, with the net outcome favoring cortical hyperexcitability.

Here, we use the visual cortex as a model to study the role of Ube3a in the establishment and function of inhibitory circuits. We show that *Ube3a*$^{m-/p+}$ mice have an abnormal accumulation of clathrin-coated vesicles at inhibitory axon terminals, indicating a defect in vesicle cycling. Consistent with this observation, inhibitory synaptic transmission onto L2/3 pyramidal neurons recovers slower following vesicle depletion in *Ube3a*$^{m-/p+}$ mice, compared to wildtypes. Recovery following high-frequency stimulation of excitatory synapses onto L2/3 pyramidal neurons, however, is normal. This discrepancy among synapse types may further contribute to excitatory/inhibitory imbalance during high levels of activity. Finally, we show that synaptic inputs onto inhibitory neurons in *Ube3a*$^{m-/p+}$ mice are largely normal. We conclude that neuron type-specific synaptic deficits likely underlie neocortical excitatory/inhibitory imbalance in AS.

2.3 Results

2.3.1 Inhibitory Deficits in Mature Ube3a$^{m-/p+}$ Mice

An excitatory/inhibitory imbalance in AS could arise from reduced numbers of inhibitory interneurons, abnormal inhibitory connectivity, and/or decreased inhibitory neurotransmission. To test the first possibility, we performed immunohistochemistry for three markers – parvalbumin, calretinin, and somatostatin – which together label 96% of the total GABAergic interneurons in L2/3 of mouse primary visual cortex (V1) (Gonchar et al., 2007). We compared *Ube3a*$^{m-/p+}$ mice and their wildtype (WT) 129Sv/Ev strain

littermate controls at postnatal day 80 (P80), an age where AS model mice exhibit abnormal EEG patterns and are susceptible to seizures (Jiang et al., 1998). We found no differences in the density of inhibitory interneurons expressing these markers (**Fig. 2.1A-B**), implying that the relative number of inhibitory interneurons is normal in L2/3 of V1.

Next we investigated the strength and number of inhibitory synapses onto L2/3 pyramidal neurons. Using whole-cell voltage-clamp, we recorded miniature inhibitory postsynaptic currents (mIPSCs) in the presence of tetrodotoxin to gauge spontaneous inhibitory synaptic activity onto excitatory L2/3 pyramidal neurons. We recorded mIPSCs at two ages: P25, during the critical period for ocular dominance plasticity and when excitatory deficits have been observed previously, and P80, when the visual cortex is fully mature. We observed no difference in mIPSC amplitude between WT and *Ube3a*$^{m-/p+}$ mice at either P25 or P80, suggesting that the loss of Ube3a did not change the strength of inhibitory synapses (**Fig. 2.1D; Table 2.1**). While we saw no genotypic differences in mIPSC frequency at P25, L2/3 pyramidal neurons in *Ube3a*$^{m-/p+}$ mice had a reduction in mIPSC frequency by P80 (**Fig. 2.1E**). These observations indicate that the loss of Ube3a leads to fewer functional inhibitory synapses, or a reduction of their release probability onto L2/3 pyramidal neurons.

To further investigate the development of inhibitory inputs onto L2/3 pyramidal neurons, we recorded evoked inhibitory postsynaptic currents (eIPSCs) using L4 stimulation at different intensities in P25 and P80 *Ube3a*$^{m-/p+}$ and WT mice (**Fig. 2.1F**). This type of stimulation activates diverse inhibitory inputs and, with strong stimulation, can activate most of the inhibitory inputs onto L2/3 pyramidal neurons (Morales et al.,

2002). We saw no significant difference in eIPSC amplitude at P25 (**Fig. 2.1G**), but a large decrease in eIPSC amplitude at P80 in *Ube3a*$^{m-/p+}$ mice compared to WT (**Fig. 2.1H**). Together, these results confirm that there is a severe deficit in the amount of inhibition arriving onto L2/3 pyramidal cells in the mature visual cortex of *Ube3a*$^{m-/p+}$ mice.

In principle, a decrease in eIPSC amplitude could arise from reductions in the number of postsynaptic GABA receptors, a decrease in the release probability of inhibitory axon terminals, fewer functional inhibitory synapses, or a depolarized inhibitory interneuron action potential threshold. It is unlikely that the decrease in eIPSC amplitude at P80 is due to a decrease in the number of GABA receptors at active synapses, since the amplitude of mIPSCs was similar in *Ube3a*$^{m-/p+}$ and WT mice. To assess whether the decrease in eIPSC amplitude is due to the loss of functional synapses or to a decrease in release probability, we examined the paired-pulse ratio of inhibitory inputs. Specifically, we stimulated L4 at varying inter-pulse intervals to evoke IPSCs in L2/3 pyramidal cells, and compared the paired-pulse ratio in WT and *Ube3a*$^{m-/p+}$ mice. We observed no difference in the paired-pulse ratio between genotypes at either P25 or P80, implying that release at functional inhibitory inputs onto L2/3 pyramidal cells is normal in response to brief stimuli given at several interpulse intervals (**Fig. 2.1I**). Finally, we found no difference in the action potential threshold or intrinsic excitability of FS neurons (a major class of inhibitory interneurons) in *Ube3a*$^{m-/p+}$ mice compared to WT, indicating that reduced eIPSC amplitude is unlikely to be due to reductions in evoked action potentials in inhibitory interneurons (**Fig. 2.2A-B**). By exclusion, our data suggest a reduction in the total number of functional inhibitory

synapses.

2.3.2 Neuron type-specific Reduction in Functional Synapses in Ube3a$^{m-/p+}$ Mice

Our previous observations of reduced inhibition were made in *Ube3a*$^{m-/p+}$ mice on the 129Sv/Ev strain, which are susceptible to spontaneous seizures (Jiang et al., 1998), making it difficult to determine whether the synaptic abnormalities were a cause or result of seizures (Sloviter, 1987). To address this concern, we tested for possible synaptic deficits in *Ube3a*$^{m-/p+}$ mice maintained on the C57BL/6J strain, which have a low incidence of evoked seizures and no reported spontaneous seizures (Jiang et al., 1998). We performed mIPSC recordings at P80 in WT and *Ube3a*$^{m-/p+}$ C57BL/6J mice to test if synaptic defects arose in the absence of spontaneous seizures. As before, we observed no genotypic differences in the amplitude of mIPSCs, but a large decrease in mIPSC frequency in *Ube3a*$^{m-/p+}$ mice (**Fig. 2.3A**). We also performed mEPSC recordings in L2/3 pyramidal neurons in mice on the C57BL/6J strain to confirm previous results from the 129Sv/Ev strain (Yashiro et al., 2009). Consistent with previous results, there was a significant decrease in mEPSC frequency, but not amplitude, between *Ube3a*$^{m-/p+}$ and WT mice (**Fig. 2.3B**). These observations reveal that *Ube3a*$^{m-/p+}$ L2/3 pyramidal neurons have a 50% reduction in spontaneous inhibitory synaptic activity, but only a 28% decrease in excitatory synaptic activity. Additionally, intrinsic excitability of L2/3 pyramidal neurons was increased in *Ube3a*$^{m-/p+}$ mice compared to WT (**Fig. 2.2C**). Together these data suggest that a disproportionate loss of inhibition may lead to an excitatory/inhibitory imbalance in *Ube3a*$^{m-/p+}$ L2/3 pyramidal neurons.

Ube3a is expressed by both excitatory and inhibitory interneurons in the cerebral cortex (Sato and Stryker, 2010). Therefore, Ube3a loss might be expected to affect both neuron classes. To assess this possibility, we recorded spontaneous synaptic activity in fast-spiking (FS) inhibitory interneurons, which we identified by membrane properties, aspinous dendrites, and characteristic high firing rates (Okaty et al., 2009). FS inhibitory interneurons in L2/3 were targeted for whole-cell recording at P80, an age at which excitatory and inhibitory neurotransmission onto L2/3 pyramidal neurons is altered. In contrast to L2/3 pyramidal neurons, the loss of Ube3a did not affect either the amplitude or the frequency of mIPSCs onto FS inhibitory interneurons (**Fig. 2.3C**). Moreover, excitatory connections onto FS inhibitory interneurons appeared normal, as Ube3a loss did not alter mEPSC amplitude or frequency (**Fig. 2.3D**). Similar to L2/3, Ube3a loss did not change the frequency or amplitude of mIPSCs or mEPSCs onto L5/6 FS inhibitory interneurons (**Fig. 2.4A-B**). These results imply that Ube3a loss has neuron type-specific synaptic effects.

2.3.3 Ube3a Loss Results in Inhibitory Deficits from FS Interneurons

We examined the effects of Ube3a loss on FS inhibitory interneurons, which provide the majority of perisomatic inhibitory input to L2/3 pyramidal neurons (Jiang et al., 2010), impart feed-forward and feedback inhibition, and have been implicated in seizure susceptibility (Di Cristo et al., 2004). Despite the challenge of performing paired recordings in adult neocortical slices, we were able to investigate synaptic connectivity between 83 pairs of L2/3 FS inhibitory interneurons and L2/3 pyramidal neurons in WT and *Ube3a*$^{m-/p+}$ mice at P80 (**Table 2.3**).

We first analyzed synaptic connectivity from FS inhibitory interneurons to pyramidal neurons. Using current-clamp recordings, we evoked action potentials in FS interneurons with depolarizing current injections at 30 Hz, and simultaneously recorded the response in pyramidal neurons (**Fig. 2.5A**). To measure short-term plasticity we normalized the amplitude of the evoked IPSPs to the amplitude of the first IPSP in the train. We observed no change in the short-term plasticity between genotypes (**Fig. 2.5B**). However, the amplitude of the first IPSP between these pairs was significantly decreased in *Ube3a*$^{m-/p+}$ mice, indicating decreased connection strength from FS inhibitory interneurons to L2/3 pyramidal neurons (**Fig. 2.5C**). We also found a 31% decrease in connection probability in *Ube3a*$^{m-/p+}$ mice compared to WT mice (**Fig. 2.5D**), supporting the conclusion that the decreased IPSP amplitude is likely due to a reduction in the number of functional synapses made from FS interneurons to pyramidal neurons. Finally, we estimated the average inhibitory drive from FS inhibitory interneurons onto L2/3 pyramidal neurons, by calculating the product of connection strength and connection probability, finding that inhibitory drive was reduced by 71% in *Ube3a*$^{m-/p+}$ mice compared to WT mice (**Fig. 2.5E**).

To further investigate possible effects of Ube3a loss on synaptic connectivity, we examined the connections from L2/3 pyramidal neurons to FS inhibitory interneurons. We measured short-term plasticity and found that *Ube3a*$^{m-/p+}$ mice had increased facilitation at synapses from pyramidal neuron to FS interneurons (**Fig. 2.6B**). To assess connection strength in this pathway, we measured the amplitude of the first EPSP evoked in the postsynaptic FS interneuron, detecting no difference between

genotypes (**Fig. 2.6C**). Finally, we found no genotypic difference in the connection probability of L2/3 pyramidal to FS inhibitory interneuron pairs (**Fig. 2.6D**).

These data suggest that, while excitatory connection frequency and strength onto L2/3 FS interneurons are unchanged in *Ube3a*$^{m-/p+}$ mice, excitatory inputs onto FS inhibitory interneurons have altered short-term plasticity, potentially leading to defective engagement of FS inhibitory interneurons during trains of activity. The unchanged strength of the pyramidal to FS inhibitory interneuron connections in *Ube3a*$^{m-/p+}$ mice was unexpected, since short-term plasticity measurements indicated a change in release probability at this synapse. We conclude that other factors, such as differences in calcium buffering, coupling of calcium channels to release machinery, or vesicular trafficking, must underlie the observed changes (Atwood and Karunanithi, 2002). Together, these experiments identify a specific inhibitory interneuron subtype, FS inhibitory interneurons, that is at least partially responsible for the decrease in inhibition found in L2/3 pyramidal neurons in the AS model.

2.3.4 Ube3a Loss Results in Inhibitory Deficits from Non-FS Interneurons

L2/3 pyramidal neurons receive inhibition from a variety of inhibitory interneuron subtypes (Markram et al., 2004). To test whether inhibitory deficits in *Ube3a*$^{m-/p+}$ mice could also be ascribed to other types of interneurons, we used agatoxin, a potent irreversible antagonist of P/Q-type voltage-gated calcium channels (VGCCs), to block release of GABA selectively from FS inhibitory interneurons (Jiang et al., 2010). Agatoxin suppressed about 90% of the total eIPSCs in both WT and *Ube3a*$^{m-/p+}$ mice 20 minutes after perfusion of the toxin (**Fig. 2.5G**). The agatoxin-insensitive portion of the eIPSC had an increased latency from stimulation onset and an increased rise time,

suggesting that the agatoxin-insensitive inputs targeted the distal dendrites of L2/3 pyramidal neurons (**Fig. 2.6G-H**). Agatoxin-insensitive inputs also had decreased paired-pulse depression compared to the total eIPSC, a signature of non-FS inhibitory interneurons (**Fig. 2.6F**) (Gupta et al., 2000). After agatoxin perfusion, we recorded eIPSCs at different stimulation intensities and again found a decrease in the strength of inhibitory inputs in the *Ube3a*$^{m-/p+}$ mice, compared to WT, demonstrating that Ube3a loss also affects inputs from non-FS classes of inhibitory interneurons (**Fig. 2.5H**).

2.3.5 *Ube3a*$^{m-/p+}$ mice have Defects in Synaptic Vesicle Cycling

Our electrophysiological data suggest that inhibitory deficits in *Ube3a*$^{m-/p+}$ mice result from a loss of functional inhibitory synapses onto L2/3 pyramidal neurons. However, a reduction in functional synapses could arise anatomically from fewer synaptic contacts, postsynaptically by a loss of functional receptors, or presynaptically by a severe depletion of releasable synaptic vesicles rendering a subset of inhibitory axon terminals non-functional. To test for an anatomical correlate to our functional data, we used immunohistochemistry to stain WT and *Ube3a*$^{m-/p+}$ mice for the vesicular GABA transporter (VGAT), a marker for the axon terminals of inhibitory interneurons (Chaudhry et al., 1998). We were surprised to see similar densities of VGAT-positive puncta in WT and *Ube3a*$^{m-/p+}$ mice, suggesting no change in the number of inhibitory interneuron axon terminals (**Fig. 2.8A-C**). However, there remained the possibility that some of these axon terminals were nonfunctional. To explore this possibility, we used electron microscopy to examine synaptic structure in WT and *Ube3a*$^{m-/p+}$ mice. Post-embedding immunogold localization of GABA was used to identify inhibitory synapses onto somata in L2/3 of V1. The area of GABA-positive axon terminals and proportion of

mitochondria per terminal were not different between WT and *Ube3a*$^{m-/p+}$ mice (**Fig. 2.7A$_2$-A$_3$**). However, there was a decrease in the number of synaptic vesicles, and a large increase in the number of clathrin-coated vesicles (CCVs), in the *Ube3a*$^{m-/p+}$ mice compared to WT (**Fig. 2.7A$_4$-A$_5$, 2.8F-G**). We also tested whether the defects we observed in inhibitory synapses were generalized to excitatory synapses. Similar to inhibitory synapses, we observed a decrease in the number of synaptic vesicles, but no change in the area of excitatory axon terminals or the proportion of mitochondria per terminal (**Fig. 2.7B$_1$-B$_4$, 2.8D-E**). Finally, we saw little or no decrease in the number of CCVs at excitatory synapses between genotypes (**Fig. 2.7B$_5$, 2.8D-E**). These data suggest a defect in synaptic vesicle cycling in inhibitory synapses of *Ube3a*$^{m-/p+}$ mice.

2.3.6 Incomplete Recovery of IPSCs after High-Frequency Stimulation in *Ube3a*$^{m-/p+}$ mice

Previous studies examining synaptic vesicle cycling have identified genes whose mutation leads to increased numbers of CCVs in axon terminals (Slepnev and De Camilli, 2000). Many of these mutant synapses maintain the ability to release neurotransmitter and have normal short-term plasticity; however, during periods of high activity these synapses fail to adequately replenish their synaptic vesicle pool, resulting in a delayed recovery to baseline levels of transmitter release (Luthi et al., 2001). These studies led us to test if inhibitory synapses in the *Ube3a*$^{m-/p+}$ mice had functional deficits similar to other synaptic vesicle cycling mutants. We applied a train of 800 stimuli at 10 Hz while recording eIPSCs in L2/3 pyramidal neurons in WT and *Ube3a*$^{m-/p+}$ mice (**Fig. 2.7C**). We then decreased the stimulation frequency to 0.33 Hz and recorded the recovery phase of the eIPSC (**Fig. 2.7C$_1$**). Ube3a loss had no effect

on the depletion phase of the eIPSC (**Fig. 2.7C$_2$**) in agreement with our previous experiments examining short-term plasticity (**Fig. 2.1I and 2.5B**). However, we found a large decrease in the rate and level of recovery of the eIPSC in *Ube3a*$^{m-/p+}$ mice compared to WT (**Fig. 2.7C$_3$**). These data are consistent with defects in inhibitory synaptic vesicle cycling in *Ube3a*$^{m-/p+}$ mice. Specifically, the decrease in recovery of the eIPSC, combined with the increase in CCVs, suggests an inability of newly endocytosed CCVs to reenter and replenish the synaptic vesicle pool. These defects may render a subset of inhibitory synapses nonfunctional in *Ube3a*$^{m-/p+}$ mice.

Finally, we challenged excitatory synapses with the same high frequency stimulation protocol that we used to test inhibitory synapses (**Fig. 2.7D$_1$**). Unlike inhibitory synapses, Ube3a loss did not have an effect on the recovery of excitatory synapses from high-frequency stimulation (**Fig. 2.7D$_3$**). Thus, the pronounced accumulation of CCVs observed at inhibitory synapses correlates well with the selective deficits in the synaptic recovery from high-frequency stimulation. Moreover, these functional data demonstrate that following a high-frequency train of activity a period of heightened excitatory/inhibitory imbalance may occur in this circuit.

2.4 Discussion

This work represents the first demonstration that maternal loss of Ube3a, as seen in individuals with AS, leads to neuron type-specific synaptic deficits. Our findings suggest that loss of Ube3a can result in an excitatory/inhibitory imbalance in the neocortex.

Earlier studies showing decreased excitatory neurotransmission in *Ube3a*$^{m-/p+}$ mice were difficult to reconcile with reports of high seizure susceptibility (Jiang et al.,

1998; Yashiro et al., 2009). Our data provides clarification, showing that the loss of Ube3a causes a particularly severe decrease in inhibitory input to L2/3 pyramidal neurons. We also report that AS model mice have a synaptic vesicle cycling defect, which suggests a basis for this deficit. The vesicle cycling defects we observe are similar to those observed after deletion of the presynaptic proteins synaptojanin (Cremona et al., 1999) or endophilin (Milosevic et al., 2011), both which lead to increased CCVs at synaptic terminals, and decreased synaptic recovery from high levels of activity. Notably, inhibitory synapses may be particularly sensitive to disruptions in vesicular trafficking, due to their enhanced activity and smaller vesicle pools (Hayashi et al., 2008). These results, combined with our functional studies describing defective inhibitory synaptic transmission in *Ube3a*$^{m-/p+}$ mice, suggest a means by which a hyperexcitable cortical circuit could arise despite fewer excitatory synapses.

Ube3a is present in both excitatory and inhibitory interneurons in the brain (Sato and Stryker, 2010). Our results showing different synaptic defects onto excitatory and inhibitory neurons indicate Ube3a deficiency causes neuron type-specific deficits. Since, Ube3a targets its substrate proteins for proteasomal degradation, the consequences of Ube3a loss may depend on which substrate proteins are normally present in a cell. This hypothesis is supported by recent work showing that Arc, a protein expressed postsynaptically in excitatory but not inhibitory interneurons, is a Ube3a substrate (Greer et al., 2010; McCurry et al., 2010). Thus, the loss of Ube3a is expected to cause an inappropriate overexpression of Arc in excitatory neurons without affecting inhibitory interneurons. Given the ability of Arc to influence AMPA receptor

endocytosis (Chowdhury et al., 2006), the neuron type-specific expression of Arc could partly explain the excitatory synaptic defects observed onto L2/3 pyramidal neurons and the lack of effect in FS interneurons. Conversely, our findings suggest a novel synaptic defect in *Ube3a*$^{m-/p+}$ mice at inhibitory synapses, primarily affecting presynaptic function at inhibitory synapses and resulting in fewer functional synapses. Intriguingly, the observed excitatory and inhibitory defects both involve endocytic processes, albeit at different sides of the synaptic cleft, suggesting common processes may be involved.

Altered function of GABA receptors and/or inhibitory interneurons has been hypothesized to underlie many of the phenotypes seen in AS (Dan and Boyd, 2003). While attention has focused on how defects in GABAergic neurotransmission may relate to epileptic phenotypes in AS, abnormalities in inhibition can have wide-ranging consequences, including disrupting synaptic plasticity, cortical network oscillations, and cortical circuit architecture (Cardin et al., 2009; Hensch, 2005). For example, FS inhibitory interneurons have a critical role in ocular dominance plasticity (Hensch et al., 1998), which is severely reduced in *Ube3a*$^{m-/p+}$ mice (Sato and Stryker, 2010; Yashiro et al., 2009). Our finding that inhibitory interneuron to L2/3 pyramidal neuron connections are altered in *Ube3a*$^{m-/p+}$ mice may prove important for understanding the mechanisms underlying plasticity and learning defects in AS. Understanding the specific synaptic impairments caused by the global loss of Ube3a may provide insights into the intractable nature of seizures found in many individuals with AS.

Excitatory/inhibitory imbalance has been observed in several genetic disorders that meet diagnostic criteria for autism spectrum disorders, including neuroligin-3 mutation, Fragile X, and Rett syndrome (Dani et al., 2005; Gibson et al., 2008; Tabuchi

et al., 2007). Moreover, excitatory/inhibitory imbalance may be a general neurophysiological feature of autism spectrum disorders, contributing to inappropriate detection or integration of salient sensory information due to a decreased signal-to-noise ratio (Rubenstein and Merzenich, 2003). Our finding that an excitatory/inhibitory imbalance may develop in AS due to the loss of functional inhibitory synapses highlights the importance of identifying Ube3a substrates in inhibitory interneurons.

2.5 Materials and Methods

2.5.1 Animals

Ube3a-deficient mice on the 129Sv/Ev background were originally developed by Jiang and colleagues (Jiang et al., 1998) and obtained through the Jackson Laboratory (Bar Harbor, ME). *Ube3a*-deficient mice backcrossed onto the C57BL/6J background were obtained from Yong-hui Jiang (Duke University). Mice of both genders were used between P21-28 or P70-90. *Ube3a*-deficient mice and WT littermates were obtained by crossing a paternal-null heterozygous female (*Ube3a*$^{m+/p-}$ mice) with a WT male, resulting in either WT progeny or progeny with loss of *Ube3a* only on the maternally-inherited allele (*Ube3a*$^{m-/p+}$ mice). Mice on the 129Sv/Ev background were used for experiments in **Fig. 2.1**. For all other experiments, mice were obtained by crossing female *Ube3a*$^{m+/p-}$ mice on a C57BL/6J background with male mice expressing GFP in a subset of parvalbumin expressing fast-spiking inhibitory interneurons (Chattopadhyaya et al., 2004) (obtained from Jackson Laboratory). Mice were raised on a 12-h light/dark cycle. All studies were conducted with protocols approved by the University of North Carolina at Chapel Hill Animal Care and Use Committee.

2.5.2 Coronal Slice Preparation

Mice were anesthetized with pentobarbital (40 mg/kg) and decapitated after disappearance of corneal reflexes, in compliance with University of North Carolina guidelines. Brains were rapidly removed and immersed in ice-cold dissection buffer (in mM: 87 NaCl, 2.5 KCl, 1.25 NaH_2PO_4, 26 $NaHCO_3$, 75 sucrose, 10 dextrose, 1.3 ascorbic acid, 7 $MgCl_2$, and 0.5 $CaCl_2$) bubbled with 95% O_2-5% CO_2. Prior to brain removal, P70-P90 mice were first intracardially perfused with dissection buffer to better preserve neuronal health and visualization. The visual cortices were dissected and 350 µm coronal slices were prepared using a vibrating microtome (Leica VT1000S). Slices were allowed to recover for 20 min in a 35º C submersion chamber filled with oxygenated artificial cerebrospinal fluid (ACSF) (in mM; 124 NaCl, 3 KCl, 1.25 NaH_2PO_4, 26 $NaHCO_3$, 1 $MgCl_2$ 2 $CaCl_2$ and 20 glucose) and then kept at room temperature for >40 min until use (Philpot et al., 2003).

2.5.3 Voltage-clamp Recordings

To isolate miniature inhibitory postsynaptic currents (mIPSCs), slices were placed in a submersion chamber, maintained at 30º C and perfused at 2 ml/min with oxygenated ACSF (as described above) containing (in µM): 20 6,7-dinitroquinoxaline-2,3-dione (DNQX), 100 D,L-2-amino-5-phosphonopentanoic acid (APV), and 0.2 tetrodotoxin (TTX). Cells were visualized using a Ziess Axioskop microscope equipped with infrared differential interference contrast (IR-DIC) optics. FS inhibitory interneurons were identified by GFP fluorescence in L5/6 or by firing rates (measured before TTX application), aspinous dendrites, and membrane properties in L2/3. Patch pipettes were

pulled from thick-walled borosilicate glass (P2000, Sutter Instruments Novato, CA). Open tip resistances were between 2.5-5 MΩ when pipettes were filled with the internal solution containing (in mM): 2 NaCl, 141 KCl, 1 $CaCl_2$, 10 EGTA, 2 Mg-ATP, 0.3 Na-GTP, 10 HEPES, 10 Na-phosphocreatine, and 0.025 Alexa-488 or 568 with pH adjusted to 7.25 with 1M KOH and osmolarity adjusted to ~295 mOsm by addition of sucrose. Voltage-clamp recordings were performed in the whole-cell configuration using patch-clamp amplifier (Multiclamp 700A, Molecular Devices), and data were acquired and analyzed using pClamp 9.2 or 10.2 software (Molecular Devices). The high internal chloride concentration increased the chloride driving force and allowed mIPSCs to be more easily resolved at -80 mV. Pipette seal resistances were **>** 1 GΩ, and pipette capacitive transients were minimized prior to breakthrough. Changes in series and input resistance were monitored throughout the experiment by giving test pulse every 30 s and measuring the amplitude of the capacitive current. Cells were discarded if series resistance rose above 30 MΩ or series resistance or input resistance changed by >25%.

For evoked IPSCs, a different internal solution was used to minimize the firing of action potentials in the postsynaptic cell when measuring the evoked response. This internal solution contained (in mM): 107 CsOH, 107 D-gluconate, 5 TEA-Cl, 2.7 NaCl, 20 HEPES, 4 Mg-ATP, 0.3 Na-GTP, 0.2 EGTA, 10 BAPTA, 5 QX-314-Cl and 0.025 Alexa-488 with pH adjusted to 7.2 with 1M CsOH and osmolarity adjusted to ~300 mOsm by addition of sucrose. The ASCF was identical to solution described above, but tetrodotoxin was not added. To increase the driving force for chloride with this internal solution, voltage-clamp recordings were performed at 0 mV. IPSCs were evoked from a

stimulating electrode (concentric bipolar; 200 µM tip separation) placed in 150 µm ventral of the recorded neuron, and stimulation was delivered for 200 µs. For agatoxin experiments ω-Agatoxin-IVa (Ascent Scientific) was perfused at a concentration of 500 nM in 0.01% BSA for 10 minutes. eIPSC latency was calculated as the time from the stimulus artifact to the initiation of the IPSC, and the rise time was calculated as the time elapsed during the rising phase of the IPSC.

mEPSCs were recorded at -70 mV in ACSF containing (in µM) 0.2 TTX, 100 APV, and 50 picrotoxin. The internal solution contained (in mM): 100 K-Gluconate, 20 KCl, 0.2 EGTA, 4 Mg-ATP, 0.3 Na-GTP, 10 HEPES, 10 Na-phosphocreatine and 0.025 Alexa-488 or 568 with pH adjusted to 7.25 with 1M KOH and osmolarity adjusted to ~295 mOsm by addition of sucrose.

For evoked EPSCs the same internal solution was used as for evoked IPSCs, however the cells were held at the reversal potential for chloride (-35 mV). As an additional control 20 µM DNQX was washed on after the depletion and recovery phases of the experiment to test for contamination of the EPSC with an IPSC. If the EPSC did not decrease by more than 80% the experiment was not included for analysis.

2.5.4 Current-clamp Recordings

Intrinsic excitability experiments were performed at -70 mV in ACSF with the same internal solution used for mEPSC experiments. Voltage threshold for AP generation was determined by measuring when dV_m/dt reached 10 V/s. For frequency-current curves, current was injected at 40 pA steps and average AP frequency was calculated to the same current injection. Slope was determined at the linear portion of the frequency-current curve for each experiment. The spike adaptation ratio was

calculated by dividing the average of the last two inter-event intervals by the first inter-event interval in the spike train. Spike trains from 10-20 Hz or 20-100 Hz were averaged to calculate the spike adaptation for pyramidal and FS inhibitory neurons respectively. Resting membrane potential (V_m) is given without adjustment for junction potential.

Paired recordings were performed with the pyramidal neuron maintained at -80 mV and the inhibitory interneuron maintained at -65 mV for the duration of the experiment in ACSF. Identification of pyramidal and inhibitory neuron cell types was determined using morphological and spiking characteristics. A pair was considered connected if the average (>12 trials) peak amplitude of a postsynaptic potential (PSP) was >0.3 mV and followed the presynaptic AP by 1-3 ms. Average PSP amplitudes were measured with respect to baseline immediately preceding PSP onset and were averages of at least 12 trials. The internal solution used for paired recordings contained (in mM) 134 KCl, 2 NaCl, 10 HEPES, 0.2 EGTA, 10 sucrose, 4 Mg-ATP, 0.3 Na-GTP, 14 Na-phosphocreatine and 0.025 Alexa-488 with pH adjusted to 7.2 with KOH and osmolarity adjusted to ~300 mOsm by addition of sucrose. A subset of unidirectional pyramidal to FS interneuron paired recordings with 4 presynaptic action potentials at 30 Hz were not included in the short-term plasticity data but were included in the analysis of pyramidal-FS connection frequency and strength.

2.5.5 Immunohistochemistry

Light Microscopy

Histology was performed on visual cortices of ~P80 mice that were intracardially perfused with 80 mL of 4% paraformaldehyde (PB, 0.1 M, pH 6.8) and sliced coronally

at 40-60 μm on a freezing sliding microtome (Ziess HM430) for Fig. 2.1, or a Vibratome for Fig. 2.8. Slices were then washed in 0.1 M PBS and incubated in 0.1 M tris-glycine for 30 min, permeabilized in 0.3% Triton-X and blocked in 10% normal donkey serum (Eagleson et al., 2005). Primary antibodies were incubated overnight at room temp at the following concentrations: mouse anti-VGAT 1:1000 (Synaptic Systems), rabbit anti-parvalbumin 1:250 (Swant), rabbit anti-calretinin 1:200 (Swant), rabbit anti-somatostatin 1:1000 (Peninsula, Cat# T-4103). Donkey anti-rabbit secondary antibodies were incubated for 1 hr at room temp and mounted on slides. Primary visual cortex was imaged with a 20x objective on a Ziess Axioskop. For images of Alexa dye-filled cells, slices were drop fixed in 4% paraformaldehyde for 1 hr after the termination of a recording. Slices were then mounted on slides and imaged with an Olympus FV1000 confocal microscope. Z-stacks were compiled and maximum intensity projections of image series were used in figures.

For VGAT staining, antigenic sites were visualized with donkey IgG conjugated to DyLight 488 (1:200, Jackson ImmunoResearch; West Grove, PA). Sections were then counterstained with Hoechst 33342 (Invitrogen) to visualize all cell nuclei and/or with NeuroTrace 640/660 (Invitrogen) to selectively visualize neuronal somata. Sections were examined with an Olympus FV1000 laser scanning confocal microscope. Z-axis image stacks were acquired (z-step size 0.6 μm) as 1,024 × 1.024 pixel images, with a planapo ×60 objective (numerical aperture 1.42) and pinhole 1.0 Airy unit. To improve signal/noise ratio, 16 frames of each image were averaged. To obtain a better signal-to-noise ratio image stacks were processed using the AMIRA deconvolution algorithm.

Quantitative analysis was performed on randomly-selected 51 μm X 51 μm fields from layer II/III of primary visual cortex (20 fields per mice, three wild-type and three mutant mice) using ImageJ (http://rsb.info.nih.gov/ij/, Rasband, 1997-2011). Optimal visualization of punctate staining (good separation between contiguous puncta, along with clear contours for each immunopositive punctum) was achieved by setting the threshold to the median pixel value over the field under study.

Electron Microscopy

Mice were intracardially perfused with 0.9% saline solution for 1 min, followed by a mixture of depolymerized 2% paraformaldehyde and 2% glutaraldehyde (Electron Microscopy Science) in 0.1 M phosphate buffer, pH 6.8. Brains were removed and postfixed overnight in the same fixative. 50 μm-thick sections were cut on a Vibratome, incubated 1 hr in 1% osmium tetroxide in 0.1 M phosphate buffer (pH 6.8), rinsed in 0.1 M maleate buffer (pH 6.0), and incubated in 1% uranyl acetate in maleate. Sections were dehydrated in ethanol, infiltrated with Spurr resin, and flat-embedded between sheets of ACLAR plastic. Chips of tissue were cut from heat-polymerized wafers and glued to plastic blocks; thin (~70 nm) sections were collected on copper mesh grids and poststained with uranyl acetate and Sato's lead.

Postembedding immunocytochemistry was performed as previously described (Phend et al., 1992). Nickel grids were pre-treated using 0.01M citrate buffer (pH 6, at 60°C for 15 mins) and blocked in 1% bovine serum albumin in Tris-buffered saline with 0.005% Tergitol NP-10 (TBSN, pH 7.6), then incubated overnight at 21–24 °C with the rabbit anti-GABA antibody (Sigma, A2052, 1:100,000). Grids were rinsed, blocked in 1% normal goat serum in TBSN (pH 8.2), and incubated in goat anti-rabbit conjugated to 20

nm gold particles (BBI, EM.GAR20) for 2 h, rinsed, then counterstained with 1% uranyl acetate followed by Sato's lead. Electron micrographs were collected with a Philips Tecnai microscope at 80 KV.

Analysis

Inhibitory and excitatory presynaptic terminals from three wild-type and four mutant mice were analyzed (at least 20 terminals per animal for each classes). Inhibitory terminals were identified by GABA staining; attention was restricted to axosomatic contacts. Excitatory synapses terminating onto dendritic spines were identified by their prominent postsynaptic density.

Parameters measured included cross-sectional area of the presynaptic terminal and mitochondria within, number of synaptic vesicles, and number of clathrin-coated vesicles. All morphometric analyses were performed by an anatomist blinded with respect to genotype.

2.5.6 Statistics

Most experiments and analyses were performed blind to genotype. Unpaired students t-tests were used on all data except input-output, frequency-current, short-term plasticity, and connection probability. For input-output, frequency-current, and short-term plasticity analyses we employed a 2-way ANOVA to assess significance. For connection probability, we used a chi-squared test and a Fisher's exact test for significance. For depletion and recovery experiments we used a monophasic non-linear regression analysis to assess significance. The function was as follows:

$$Y=(Y_0 - \text{Plateau})^{-K*X} + \text{Plateau}$$

Where Y_0 is the Y value when time (X) is zero, Plateau is Y at infinite times, and K is the rate constant. Graphs represent the mean and error bars represent the SEM. For all figures p-values are as follows *p<0.05, **p<0.01, ***p<0.001. All statistics were performed in Graphpad Prism.

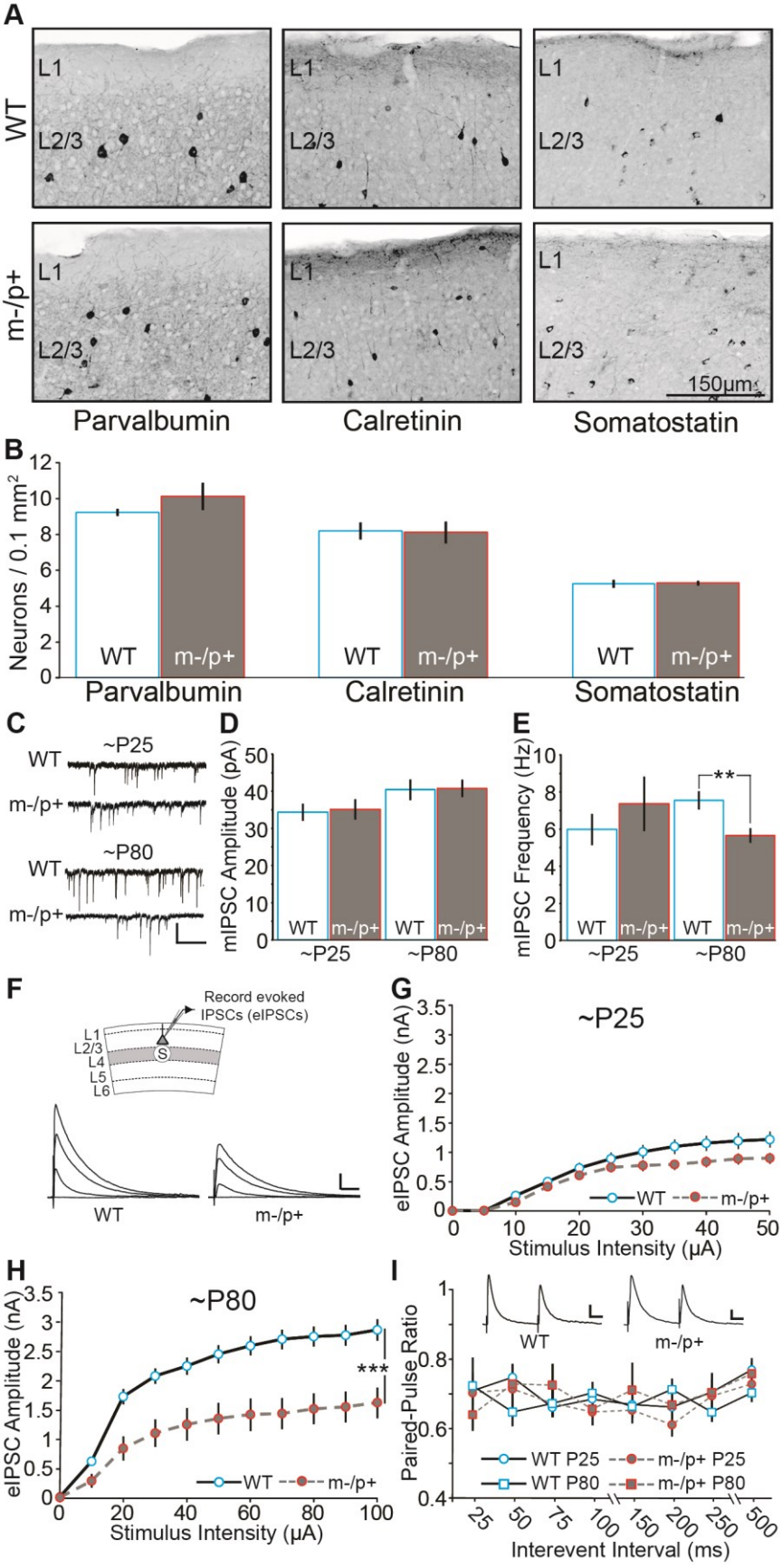
A
WT
m-/p+
L1
L2/3
150μm
Parvalbumin
Calretinin
Somatostatin
B
Neurons / 0.1 mm²
WT
m-/p+
Parvalbumin
Calretinin
Somatostatin
C
~P25
~P80
WT
m-/p+
D
mIPSC Amplitude (pA)
~P25
~P80
E
mIPSC Frequency (Hz)
**
F
Record evoked IPSCs (eIPSCs)
L1
L2/3
L4
L5
L6
S
G
~P25
eIPSC Amplitude (nA)
Stimulus Intensity (μA)
H
~P80
***
I
Paired-Pulse Ratio
WT P25
m-/p+ P25
WT P80
m-/p+ P80
Interevent Interval (ms)

Figure 2.1 Inhibitory synaptic deficits arising through development in Ube3a$^{m-/p+}$ mice are not due to decreased density of inhibitory interneurons.

(A) Photomicrographs of immunocytochemical markers for inhibitory interneurons in visual cortex of wildtype (WT) and *Ube3a*-deficient (m-/p+) mice. (B) Quantification of parvalbumin, calretinin, and somatostatin positive neurons in L2/3 of mouse primary visual cortex at ~P80 (n=4 mice/genotype). (C) Sample mIPSC recordings from ~P25 (P21-P28) and ~P80 (P70-P90) WT and *Ube3a*$^{m-/p+}$ mice (scale bar = 30 pA, 400 ms). (D) Average mIPSC amplitude was similar between WT and *Ube3a*$^{m-/p+}$ mice at ~P25 (WT n=10 cells; m-/p+ n=8 cells) and ~P80 (n=13 cells/genotype) in L2/3 pyramidal cells. (E) Average mIPSC frequency for ~P25 (WT n=10 cells; m-/p+ n=8 cells) and ~P80 (n=13 cells/genotype) (see also Table 2.1). (F) Illustration of stimulation (L4) and recording (L2/3 pyramidal neuron) configuration in primary visual cortex, and sample recordings of evoked IPSCs at stimulation intensities of 0, 10, 30, and 100 μA (scale bar = 500 pA, 30 ms). (G) Evoked IPSCs at ~P25 (WT n=26 cells; m-/p+ n=29 cells) and (H) ~P80 (WT n=20 cells; m-/p+ n=14 cells). (I) Sample recordings of evoked IPSCs in paired-pulse experiments (scale bar = 100pA, 20 ms) and quantification of paired-pulse ratio in mice aged ~P25 (WT n=12 cells; m-/p+ n=11 cells) and ~P80 (WT n=13 cells; m-/p+ n=8 cells.) (see also Fig. 2.2). All data are represented as the mean ± SEM; **p<0.01, ***p<0.001.

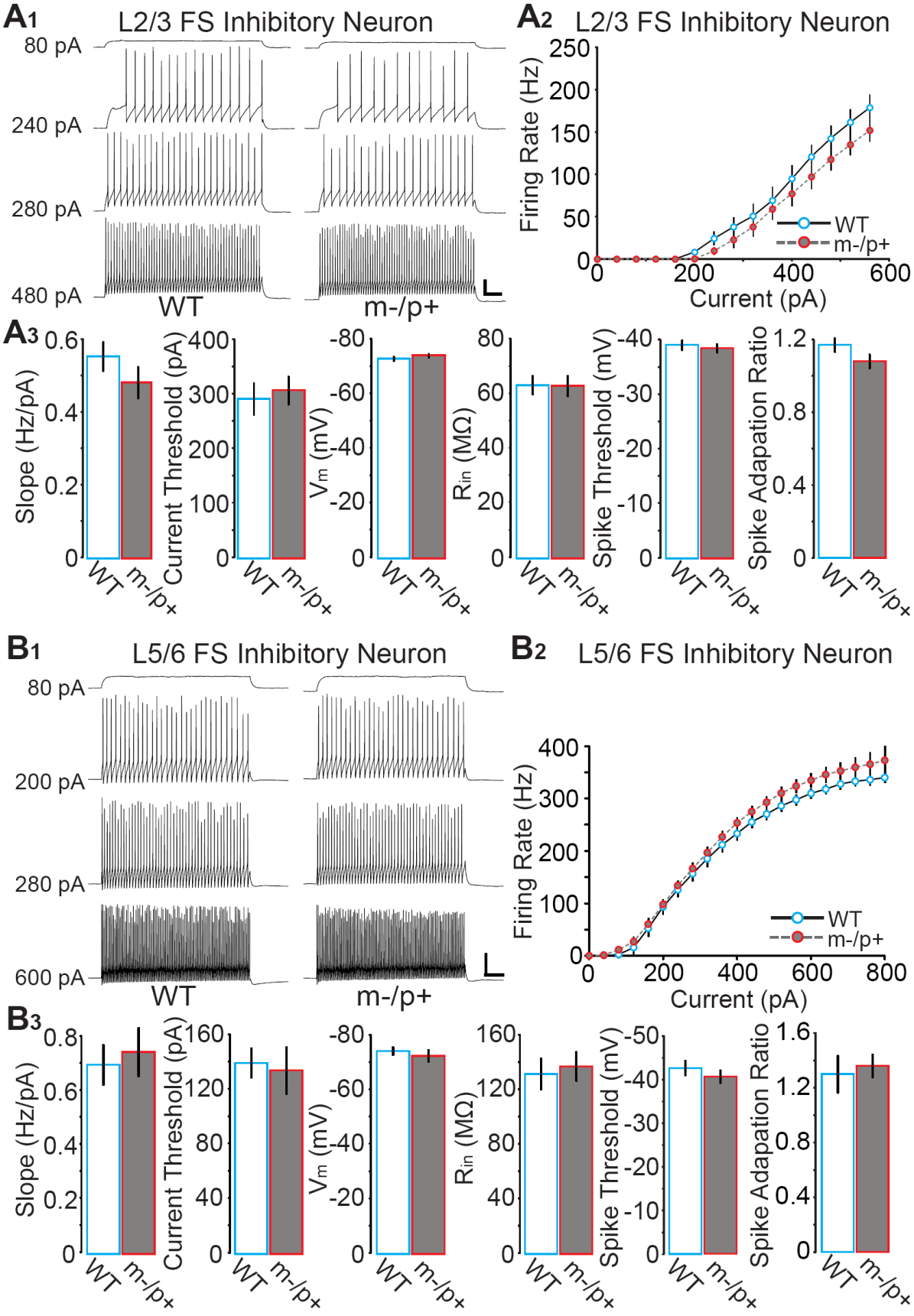
A1
L2/3 FS Inhibitory Neuron
80 pA
240 pA
280 pA
480 pA
WT
m-/p+
A2
L2/3 FS Inhibitory Neuron
Firing Rate (Hz)
Current (pA)
WT
m-/p+
A3
Slope (Hz/pA)
Current Threshold (pA)
Vm (mV)
Rin (MΩ)
Spike Threshold (mV)
Spike Adapation Ratio
B1
L5/6 FS Inhibitory Neuron
80 pA
200 pA
280 pA
600 pA
WT
m-/p+
B2
L5/6 FS Inhibitory Neuron
Firing Rate (Hz)
Current (pA)
WT
m-/p+
B3
Slope (Hz/pA)
Current Threshold (pA)
Vm (mV)
Rin (MΩ)
Spike Threshold (mV)
Spike Adapation Ratio

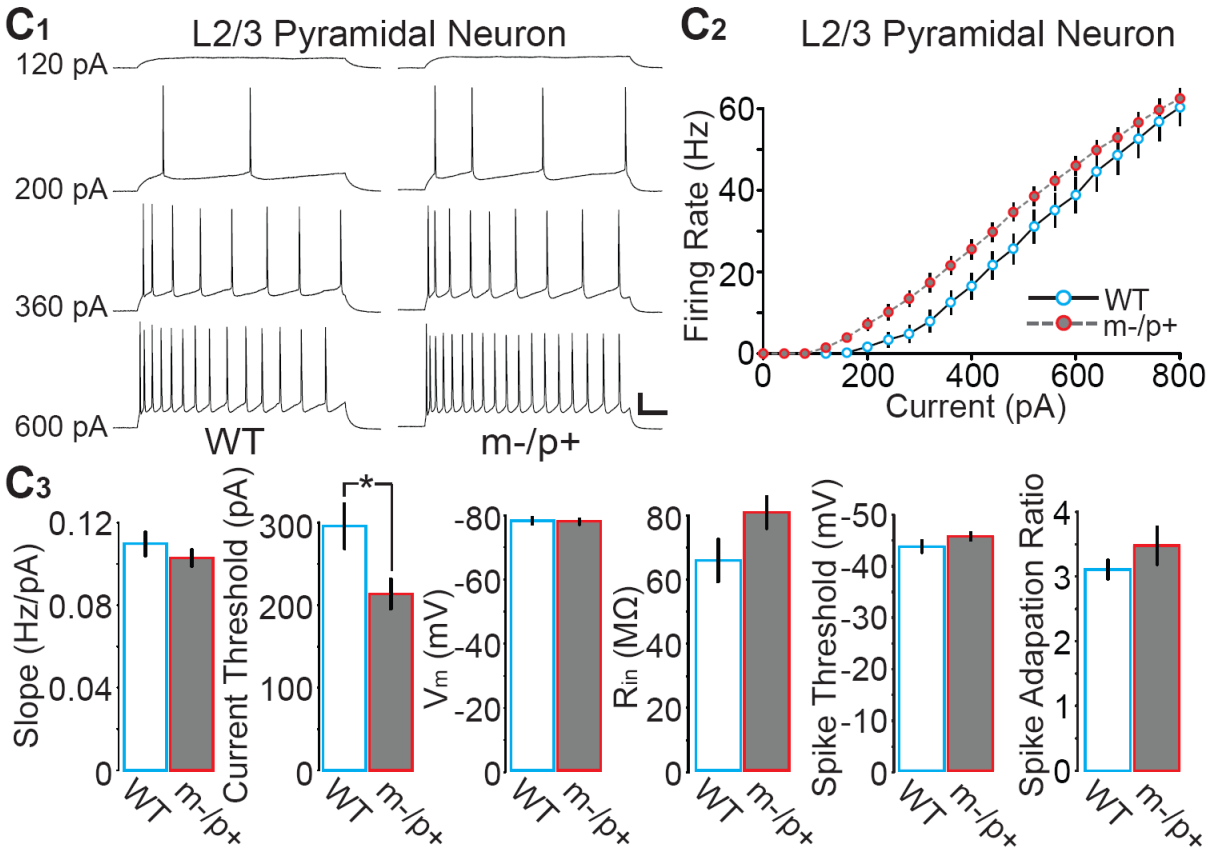

Figure 2.2 L2/3 pyramidal neurons, but not FS inhibitory interneurons, have increased intrinsic excitability in *Ube3a*$^{m-/p+}$ mice at P80.

(A_1) Sample responses of a L2/3 FS inhibitory interneuron to current injections and (A_2) average frequency-current curves from WT and *Ube3a*$^{m-/p+}$ mice (cell was held at -70 mV) (WT n=13 cells; m-/p+ n=10 cells; scale bar 20 mV, 40 ms). (A_3) Average values (left to right) of frequency-current curve slope (p=0.24), current threshold (p=0.69), resting membrane potential (V_m; p=0.28), input resistance (R_{in}; p=0.95), voltage threshold for spiking (p=0.63) and spike adaptation ratio (p=0.11). (B_1) Sample responses of a L5/6 GFP+ FS inhibitory interneuron to current injections and (B_2) average frequency-current curves from WT and *Ube3a*$^{m-/p+}$ mice (cell was held at -65 mV) (WT n=8 cells; m-/p+ n=11 cells; scale bar 20 mV, 40 ms). (B_3) Average values

(left to right) of frequency-current curve slope (p=0.70), current threshold (p=0.81), resting membrane potential (V_m; p=0.54), input resistance (R_{in}; p=0.72), voltage threshold for spiking (p=0.38), and spike adaptation ratio (p=0.86). (C_1) Sample responses of a L2/3 pyramidal neuron to current injections and (C_2) average frequency-current curves from WT and *Ube3a*$^{m-/p+}$ mice (cell was held at -70 mV) (WT n=10 cells; m-/p+ n=23 cells; p=0.09; scale bar 20 mV, 40 ms). (C_3) Average values (left to right) of frequency-current curve slope (p=0.35), current threshold (p=0.02), resting membrane potential ($V_{m;}$; p=0.85), input resistance (R_{in}; p=0.08), and voltage threshold for spiking (p=0.19). All bars represent the mean ± SEM; *p<0.05.

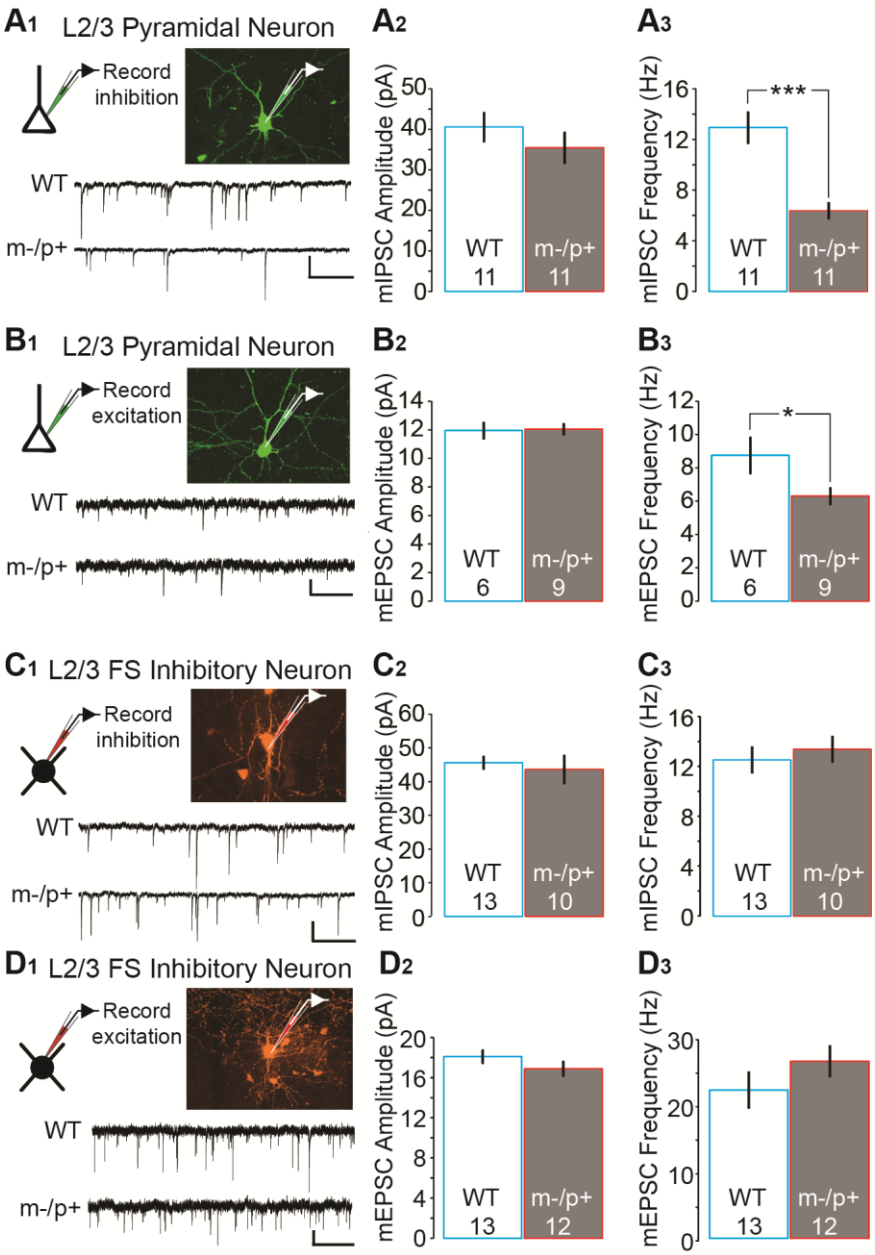

Figure 2.3 Ube3a loss leads to neuron type-specific defects in inhibitory neurotransmission.

(A_1) Illustration and photomicrograph of a filled L2/3 pyramidal neuron and sample recordings from ~P80 WT (upper) and *Ube3a*$^{m-/p+}$ (lower) mice (scale bar = 40 pA, 300 ms.) (A_2) Average mIPSC amplitude (n=11 cells/genotype, p=0.16) and (A_3)

frequency (n=11 cells/genotype) from L2/3 pyramidal neurons. (B_1) Illustration and fill of a L2/3 pyramidal neuron and sample recordings from ~P80 WT (upper) and *Ube3a*$^{m-/p+}$ (lower) mice (scale bar 15 pA, 300 ms). (B_2) Average mEPSC amplitude (WT n=6 cells; m-/p+ n=9 cells) and (B_3) frequency (WT n=6 cells; m-/p+ n=9 cells) from L2/3 pyramidal neurons. (C_1) Illustration and fill of a L2/3 FS inhibitory interneuron and sample recordings from ~P80 WT (upper) and *Ube3a*$^{m-/p+}$ (lower) mice (scale bar 40 pA, 300 ms). (C_2) Average mIPSC amplitude (WT n=13 cells; m-/p+ n=10 cells) and (C_3) frequency (WT n=13 cells; m-/p+ n=10 cells; p=0.57) from L2/3 FS inhibitory interneurons. (D_1) Illustration and fill of a L2/3 FS inhibitory interneuron and sample recordings from ~P80 WT (upper) and *Ube3a*$^{m-/p+}$ (lower) mice (scale bar 10 pA, 300 ms). (D_2) Average mEPSC amplitude (WT n=13 cells; m-/p+ n=12 cells) and (D_3) frequency (WT n=13 cells; m-/p+ n=12 cells) from L2/3 FS inhibitory interneurons (see also Fig. 2.4 and Table 2.2). Bar graphs represent the mean ± SEM; p*<0.05, p***<0.001.

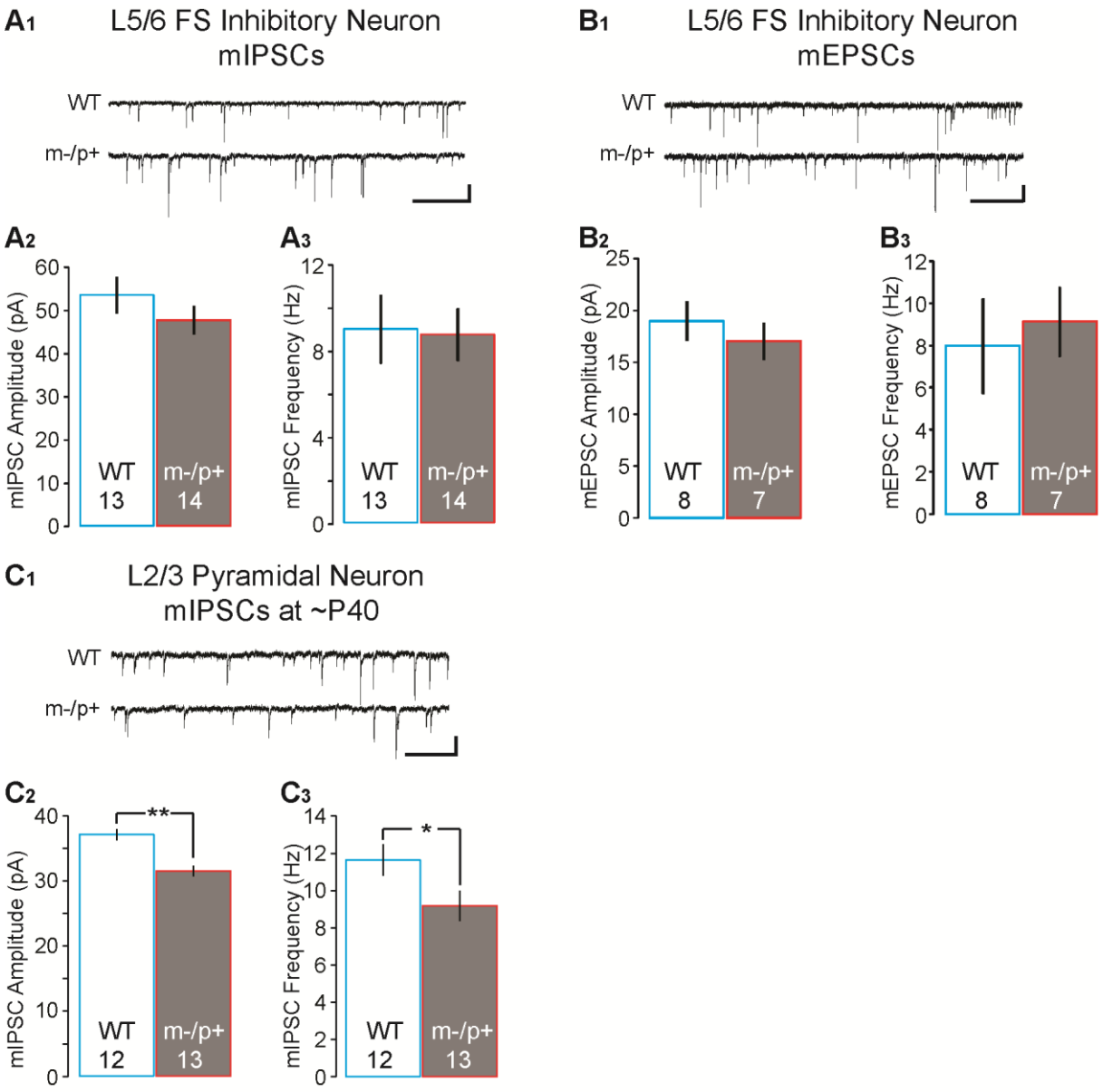

Figure 2.4 L5/6 FS inhibitory interneurons do not show changes in mEPSC or mIPSC amplitude or frequency at ~P80, L2/3 pyramidal neurons have decreased mIPSC amplitude and frequency at ~P40

(A_1) Sample recordings from ~P80 WT (upper) and *Ube3a*$^{m-/p+}$ (lower) mice (scale bar = 40 pA, 300 ms.) (A_2) Average mIPSC amplitude (WT n=13 cells; m-/p+ n=14 cells; p=0.30) and (A_3) frequency (WT n=13 cells; m-/p+ n=14 cells, p=0.78) from L5/6 GFP+ FS inhibitory interneurons. (B_1) Sample recordings from ~P80 WT (upper) and

Ube3a$^{m-/p+}$ (lower) mice (scale bar = 20 pA, 300 ms). (B_2) Average mEPSC amplitude (WT n=8 cells; m-/p+ n=7 cells, p=0.45) and (B_3) frequency (WT n=8 cells; m-/p+ n=7 cells; p=0.69) from L5/6 GFP+ FS inhibitory interneurons (see also Table 2.2). (C_1) Sample recordings from ~P40 WT (upper) and *Ube3a*$^{m-/p+}$ (lower) mice (scale bar = 40 pA, 300 ms.) (C_2) Average mIPSC amplitude (WT n=12 cells; m-/p+ n=13 cells; p=0.02) and (C_3) frequency (WT n=12 cells; m-/p+ n=13 cells, p=0.04) from L2/3 pyramidal neurons. Bar graphs represent the mean ± SEM.

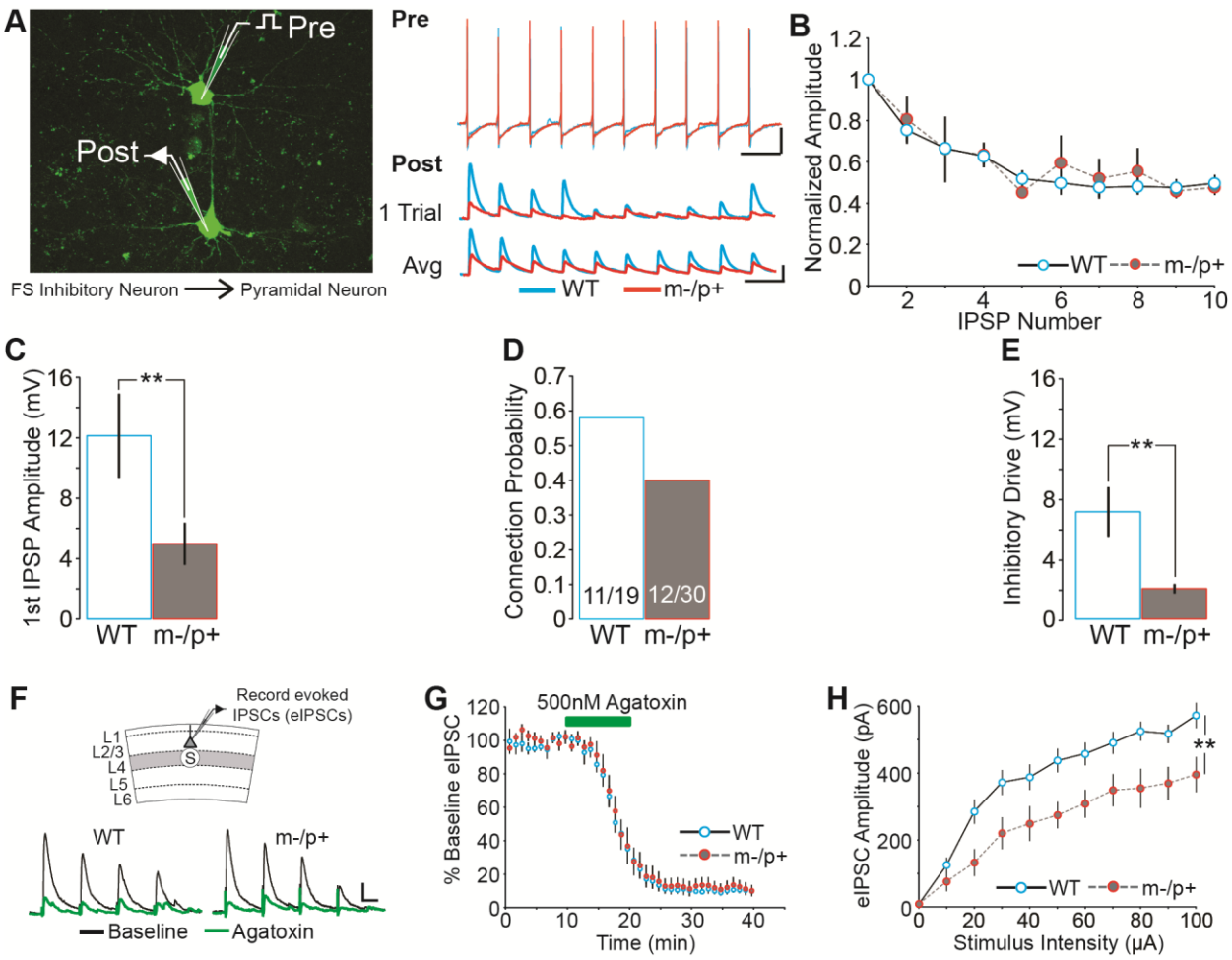

Figure 2.5 Synaptic deficits arise from both FS and non-FS inhibitory interneurons in *Ube3a*$^{m-/p+}$ mice.

(A) Recording configuration (left) and representative recordings of presynaptic action potentials evoked in a FS inhibitory interneuron (upper), and resulting unitary IPSPs in a L2/3 pyramidal neuron (lower) from WT (blue) and *Ube3a*$^{m-/p+}$ mice (red). Average is of 12 trials. Scale bar "Pre" 20 mV, 40 ms; "Post" 4 mV, 40 ms. (B) Average short-term plasticity of inhibitory to excitatory connections (WT n=8; m-/p+ n=12) (presynaptic spikes @ 30 Hz). (C) Average unitary IPSP amplitude of 1st IPSP of inhibitory to excitatory connections (WT n=8; m-/p+ n=12). (D) Connection probability of FS

inhibitory interneurons to L2/3 pyramidal neurons (numbers of connected/total pairs written in bars); (E) inhibitory drive of FS inhibitory interneurons to L2/3 pyramidal neurons (WT n=19 pairs; m-/p+ n=30 pairs). (F) Recording configuration (upper) and representative recordings (lower) of eIPSCs during baseline (black) and 20 minutes after 500 nM ω-agatoxin-IVa perfusion (green) (scale bar = 100 pA, 20 ms). (G) A 10 minute baseline was recorded before a 10 minute perfusion of agatoxin (green bar) (WT n=10; m-/p+ n=10). (H) Input-output relationship in the agatoxin-insensitive portion of total eIPSC performed 20 minutes after cessation of agatoxin perfusion (WT n=10; m-/p+ n=10). (see also Figure 2.6 and Table 2.3). Data are represented as the mean ± SEM; *p<0.05, **p<0.01, ***p<0.001.

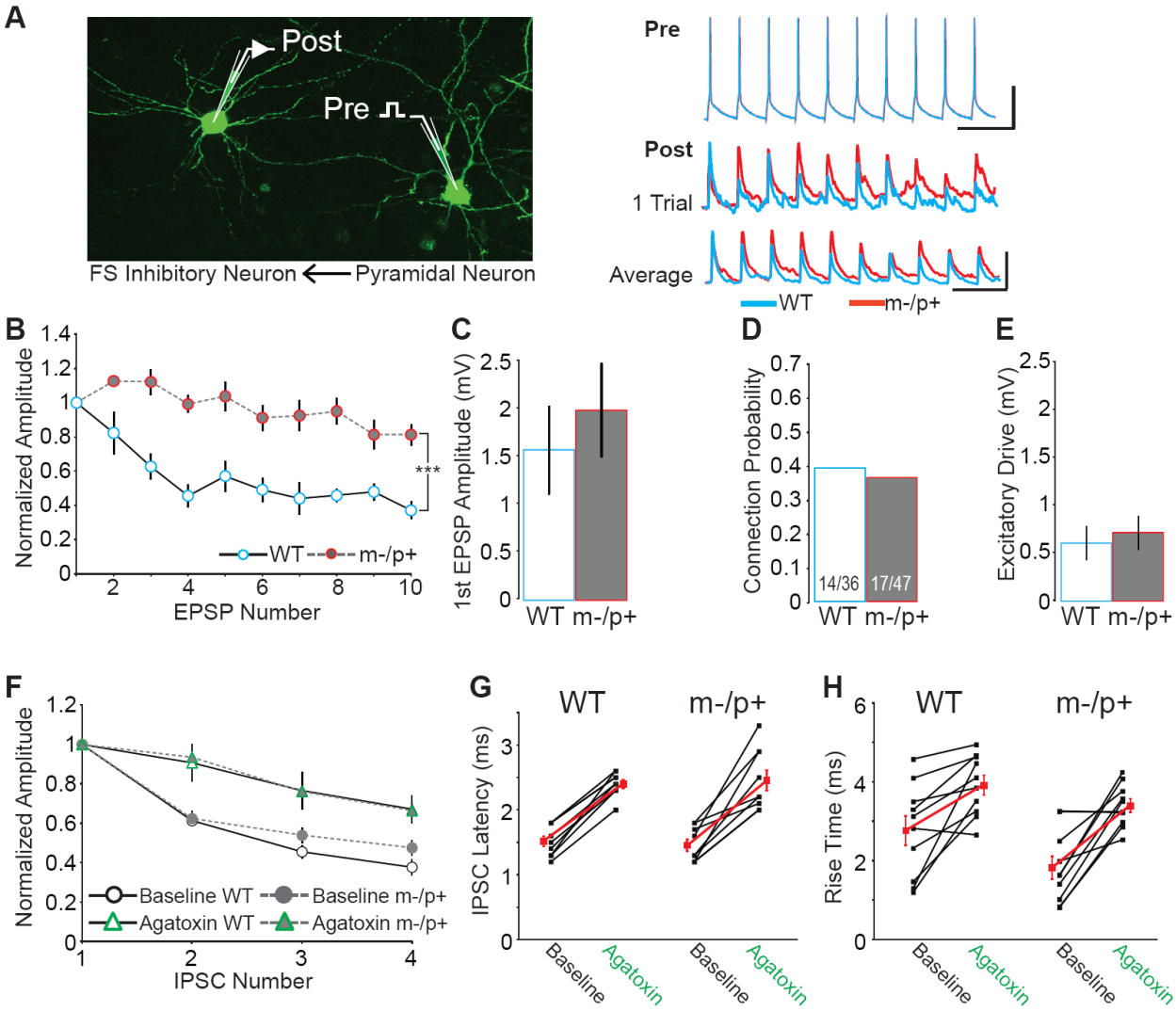

Figure 2.6 L2/3 pyramidal to L2/3 FS inhibitory interneuron paired recordings and effects of agatoxin on eIPSC short-term plasticity, latency, and rise time.

(A) Recording configuration (left) and representative recordings of presynaptic action potentials evoked in a L2/3 pyramidal neuron (upper), and resulting unitary EPSPs in a FS inhibitory interneuron (lower) from WT (blue) and *Ube3a*$^{m-/p+}$ mice (red). Average is of 12 trials. Scale bar "Pre" 40 mV, 60 ms; "Post" 4 mV, 60 ms. (B) Average short-term plasticity of excitatory to inhibitory connections (WT n=6; m-/p+ n=10; p=0.001) (presynaptic spikes @ 30 Hz). (C) Average unitary EPSP amplitude of 1st EPSP of

excitatory to inhibitory connections (WT n=14; m-/p+ n=16; p=0.54). (D) Connection probability of L2/3 pyramidal neurons to FS inhibitory interneurons (numbers of connected/total pairs written in bars) and (E) the average excitatory drive of connected and non-synaptically connected pairs (WT n=36 pairs; m-/p+ n=47 pairs). (F) eIPSCs normalized to the 1st IPSC in a 4 pulse stimulation train at 20 Hz during baseline period and 20 min after perfusion with 500 nM agatoxin (green) (WT n=10; m-/p+ n=10). (G) Increase in latency between stimulus artifact and eIPSC onset after perfusion of 500 nM agatoxin (red line shows mean ± SEM) (WT n=10; m-/p+ n=10). (H) Increase in rise time of eIPSC after perfusion of 500 nM agatoxin (red line shows mean ± SEM) (WT n=10; m-/p+ n=10).

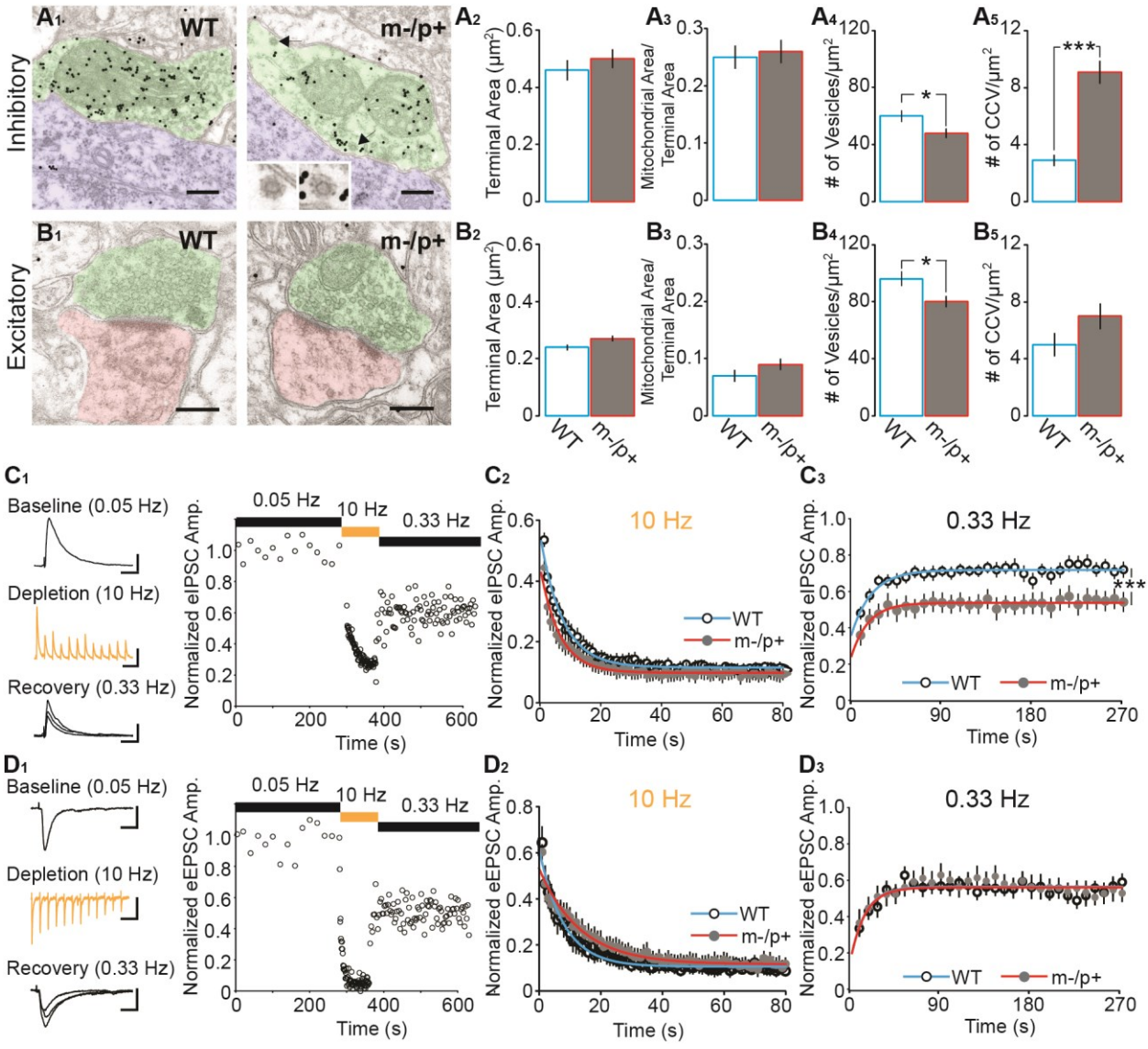

Figure 2.7 Inhibitory synapses of *Ube3a*$^{m-/p+}$ mice have presynaptic defects.

(A_1) Electron micrographs of inhibitory synapses stained for GABA in ~P80 WT and *Ube3a*$^{m-/p+}$ mice (green denotes axon terminal, blue denotes soma), insets highlight CCVs (scale bar = 250 nm). Average values of (left to right) (A_2) axon terminal area, (A_3) mitochondrial area divided by terminal area, (A_4) number of synaptic vesicles per square micron, and (A_5) number of CCVs per square micron (WT n = 3; m-/p+ n = 4). (B_1) Electron micrographs of excitatory synapses in WT and *Ube3a*$^{m-/p+}$ mice (green

denotes axon terminal, red denotes spine) (scale bar = 250 nm). Average values of (left to right) (B_2) axon terminal area, (B_3) mitochondrial area divided by terminal area, (B_4) number of synaptic vesicles per square micron, and (B_5) number of CCVs per square micron (WT n = 3; m-/p+ n = 4). (C_1) Sample recordings (left) and sample experiment (right) showing baseline (black), high frequency depletion (orange), and recovery (black) phases (scale bars; baseline = 200 pA, 20 ms; depletion = 200 pA, 200 ms; recovery = 200 pA, 20 ms). (C_2) Average depletion phase showing eIPSC amplitude normalized to baseline during 800 stimuli at 10 Hz. 10 responses are averaged for each point and a monophasic exponential was fit to the averaged responses for WT and *Ube3a*$^{m-/p+}$ mice (WT n=19; m-/p+ n=18). (C_3) Average recovery phase showing eIPSC amplitude normalized to baseline during 90 stimuli at 0.33 Hz. 3 responses are averaged for each point and a monophasic exponential was fit to the averaged responses for WT and *Ube3a*$^{m-/p+}$ mice (WT n=19; m-/p+ n=18). (D_1) Sample recordings (left) and sample experiment (right) showing baseline (black), high frequency depletion (orange), and recovery (black) phases (scale bars; baseline = 100 pA, 10 ms; depletion = 100 pA, 200 ms; recovery = 100 pA, 10 ms). (D_2) Average depletion phase showing eEPSC amplitude normalized to baseline during 800 stimuli at 10 Hz. 10 responses are averaged for each point and a monophasic exponential was fit to the averaged responses for WT and *Ube3a*$^{m-/p+}$ mice (WT n=10; m-/p+ n=11). (D_3) Average recovery phase showing eEPSC amplitude normalized to baseline during 90 stimuli at 0.33 Hz. 3 responses are averaged for each point and a monophasic exponential was fit to the averaged responses for WT and *Ube3a*$^{m-/p+}$ mice (WT n=10; m-/p+ n=11) (see also Figure 2.8). Data are represented as the mean ± SEM; *p<0.05, ***p<0.001.

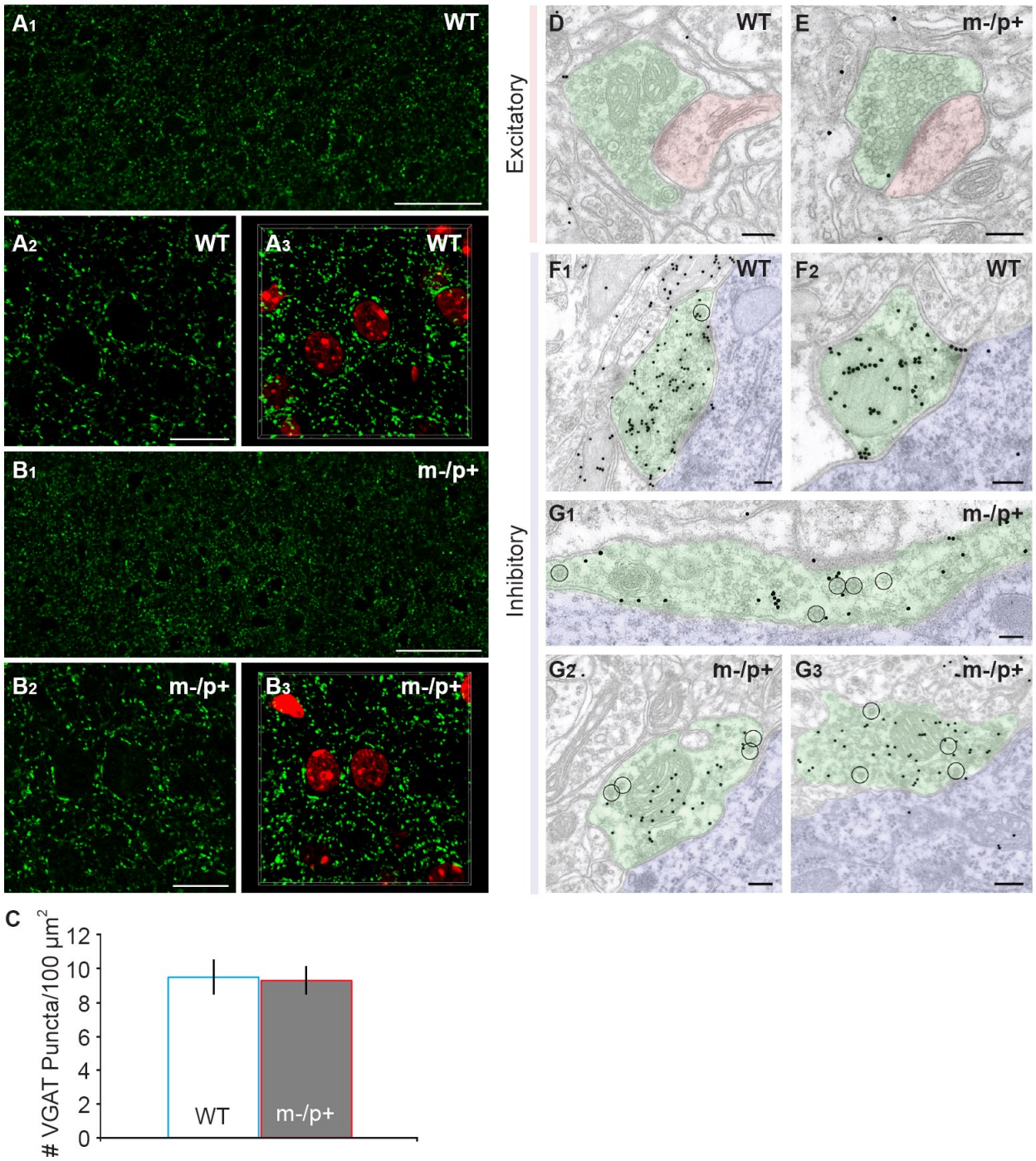

Figure 2.8 Quantification of VGAT puncta density and electronmicrographs from WT and *Ube3a*$^{m-/p+}$ mice.

(A and B) Photomicrographs of immunocytochemical markers of inhibitory interneuron terminals (VGAT) in L2/3 visual cortex of WT (A) and *Ube3a*$^{m-/p+}$ (B) mice, nuclei are

stained with Neurotrace (A_3 and B_3) (scale bar A_1 and B_1 = 50 μm; A_2 and B_2 = 15 μm). (C) Quantification of VGAT puncta per 100 square microns (n=3 animals/genotype). (D and E) Electron micrographs of excitatory synapses in WT and *Ube3a*$^{m-/p+}$ mice (green denotes axon terminal, red denotes spine) (scale bar = 200 nm). (F and G) Electron micrographs of immunogold staining of GABA used to identify inhibitory synapses onto soma (blue) in L2/3 of V1. CCVs are highlighted with circles (scale bar = 200 nm).

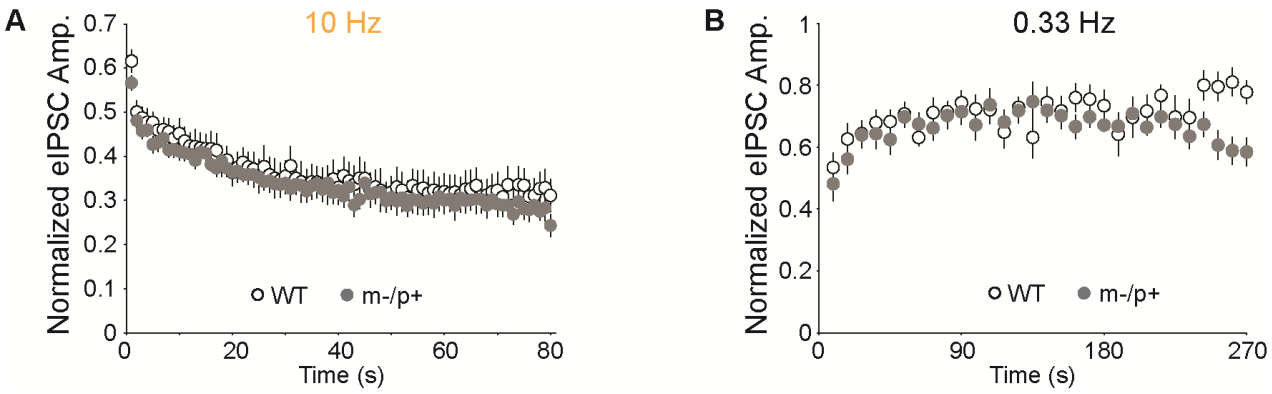

Figure 2.9 Inhibitory synaptic depletion and recovery at ~P25

(A) Average depletion phase showing eIPSC amplitude normalized to baseline during 800 stimuli at 10 Hz. 10 responses are averaged for each point for WT and *Ube3a*$^{m-/p+}$ mice (WT n=9; m-/p+ n=9). (B) Average recovery phase showing eIPSC amplitude normalized to baseline during 90 stimuli at 0.33 Hz. 3 responses are averaged for each point for WT and *Ube3a*$^{m-/p+}$ mice (WT n=9; m-/p+ n=9).

Table 2.1 Membrane properties from mIPSC experiments related to Figure 2.1

From Fig. 2.1C, D, E mIPSCs L2/3 Pyramidal Neurons 129Sv/Ev

	~P25			~P80		
	WT	m-/p+	p value	WT	m-/p+	p value
neuron number	10	8		13	12	
C_m (pF)	113±9.8	126±12.3	0.400	145±5.7	122±6.2	0.007
R_s (MΩ)	20±1.3	20±0.8	0.910	18±0.8	18±0.6	0.807
R_m (MΩ)	188±25.3	180±26.9	0.850	84±2.2	124±12.2	0.003
Tau (ms)	2.3±0.2	2.7±0.3	0.238	2.7±0.1	2.4±0.1	0.015

Table 2.2 Membrane properties from mEPSC and mIPSC experiments related to Figure 2.3 and 2.4

From Fig. 2.3A mIPSCs L2/3 Pyramidal Neurons C57BL/6J

	~P80		
	WT	m-/p+	p value
neuron number	11	11	
C_m (pF)	122±6.1	121±10.9	0.937
R_s (MΩ)	21±1.0	21±1.2	0.729
R_m (MΩ)	99±6.8	122±11.2	0.093
Tau (ms)	2.6±0.1	2.4±0.3	0.560

From Fig. 2.3B mEPSCs L2/3 Pyramidal Neurons C57BL/6J

	~P80		
	WT	m-/p+	p value
neuron number	6	9	
C_m (pF)	150±8.3	150±8.1	0.989
R_s (MΩ)	18±1.6	18±0.8	0.684
R_m (MΩ)	86±17.8	72±6.7	0.436
Tau (ms)	2.9±0.2	2.5±0.1	0.128

From Fig. 2.3C mIPSCs L2/3 FS Inhibitory Neurons C57BL/6J

	~P80		
	WT	m-/p+	p value
neuron number	13	10	
C_m (pF)	42±2.3	39±1.2	0.295
R_s (MΩ)	24±1.1	27±1.7	0.105
R_m (MΩ)	101±6.8	111±8.8	0.366
Tau (ms)	.418±0.04	.446±0.03	0.623

From Fig. 2.3D mEPSCs L2/3 FS Inhibitory Neurons C57BL/6J

	~P80		
	WT	m-/p+	p value
neuron number	13	12	
C_m (pF)	58±3.2	60±3.7	0.756
R_s (MΩ)	21±0.9	20±1.2	0.492
R_m (MΩ)	84±5.0	81±4.4	0.698
Tau (ms)	.865±0.05	.884±0.04	0.778

From Fig. 2.4A mIPSCs L5/6 FS Inhibitory Neurons C57BL/6J

	~P80		
	WT	m-/p+	p value
neuron number	13	14	
C_m (pF)	39±2.5	36±2.8	0.454
R_s (MΩ)	28±1.0	30±0.9	0.226
R_m (MΩ)	185±36.2	177±17.7	0.805
Tau (ms)	.702±0.07	.745±0.03	0.654

From Fig. 2.4B mEPSCs L5/6 FS inhibitory Neurons C57BL/6J

	~P80		
	WT	m-/p+	p value
neuron number	8	7	
C_m (pF)	42±4.3	34±2.4	0.136
R_s (MΩ)	26±2.5	27±1.8	0.599
R_m (MΩ)	153±18.3	187±20.4	0.235
Tau (ms)	.774±0.09	.577±0.11	0.201

Table 2.3 Membrane properties from Paired Recordings and Agatoxin experiments related to Figure 2.5 and 2.6

From Fig. 2.5A-F Intrinsic membrane properties from paired recordings

	~P80			
	WT		m-/p+	
	L2/3 Pyr.	L2/3 FS	L2/3 Pyr.	L2/3 FS
neuron number	36	36	47	47
V_m (mV)	-79±1.8	-72±0.9	-81±0.9	-72±0.9
R_m (MΩ)	105±10.9	110±11.1	107±6.9	120±8.1
Distance btwn soma(μm)	51±3.8		68±5.3	

From Fig. 2.5G-I Agatoxin eIPSC Recordings

	~P80		
	WT	m-/p+	p value
neuron number	10	10	
C_m (pF)	173±10.5	160±10.4	0.423
R_s (MΩ)	12±0.8	12±0.6	0.468
R_m (MΩ)	224±17.6	268±21.6	0.401
Tau (ms)	2.1±0.11	2.0±0.16	0.374

CHAPTER 3: CIRCUIT AND CELL-TYPE SPECIFIC REQUIREMENTS FOR *Ube3a* IN NEOCORTICAL EXCITATORY/INHIBITORY BALANCE

3.1 Overview

Balanced excitation and inhibition is critical for normal circuit function and disruptions in excitation/inhibition (E/I) balance have been shown to exist in many neurological disorders. Recently, we have shown that an Angelman syndrome mouse model (*Ube3a*$^{m-/p+}$) has an E/I imbalance in cortical circuits. Inhibitory deficits appeared to arise from defective presynaptic vesicle cycling resulting in decreased evoked and spontaneous neurotransmission. Defining the neuron class or classes required for the resulting imbalance is crucial to our understanding of neural circuit dysfunction in Angelman syndrome as well as elucidating the role of Ube3a in different neuronal subtypes. To permit detailed dissection of the role of Ube3a in specific neural circuits we generated a conditional *Ube3a* knockout mouse which allows neuron type-specific deletion of *Ube3a*. Surprisingly, when we deleted *Ube3a* in all GABAergic neurons we observed none of the synaptic phenotypes observed when *Ube3a* was deleted from all neurons. Conversely, when we deleted *Ube3a* from cortical pyramidal neurons we observed only defects in evoked inhibition. Together these findings suggest Ube3a loss is required both pre and postsynaptically for several synaptic phenotypes observed in AS model mice. These results were supported by data showing that re-expression of *Ube3a* in GABAergic neurons was sufficient to normalize defects in inhibitory synaptic

vesicle cycling but not evoked inhibition. Intriguingly, Ube3a may be required in only a subset of neurons to achieve normal circuit balance.

3.2 Introduction

Classical knockout mouse models of genes implicated in human disorders offer an excellent opportunity to study human health and disease in an experimentally tractable animal. One such human disorder is Angelman Syndrome (AS), a severe genetic neurodevelopmental disorder caused by deletion or mutation of maternally inherited *UBE3A* (Williams et al., 2006). AS model mice exhibit behavioral changes mirroring the hallmarks of the human syndrome including abnormal EEG patterns, elevated seizure susceptibility, and difficulty with movement and balance (Jiang et al., 1998). This mouse model has allowed insight into the synaptic defects that occur when Ube3a is lost in all neurons. Previous studies have shown that Ube3a is present both pre and postsynaptically in excitatory and inhibitory neurons and deletion of *Ube3a* results in defects at excitatory and inhibitory synapses (Dindot et al., 2008; Wallace et al., 2012; Yashiro et al., 2009). These defects have been hypothesized to underlie defective circuit function and behavioral abnormalities seen in AS model mice. However, difficulties remain in the interpretation of these results as neural circuits and synapses exist under strong homeostatic control; therefore, it is often difficult to determine the synaptic defects that result directly from loss of a gene and which, if any, are induced secondarily as a consequence of altered circuit function (Marder and Goaillard, 2006; Turrigiano and Nelson, 2004). It is of great importance to understand the most direct consequences of gene loss as those may be most beneficial targets for therapeutic intervention.

Here we use electrophysiological, anatomical, and molecular genetic techniques to dissect the role of Ube3a loss in specific neuronal classes to synaptic pathophysiology. Using several newly developed conditional *Ube3a* mouse lines we manipulate *Ube3a* expression in inhibitory and excitatory neurons in the cortex and observe differential effects on synaptic transmission. We observe that deletion of *Ube3a* in all cortical inhibitory neurons is insufficient to produce synaptic defects seen when Ube3a is lost in all neurons. Conversely, deletion of *Ube3a* in all cortical excitatory neurons results in a decrease in evoked inhibition, but not in defects in spontaneous excitatory or inhibitory neurotransmission or synaptic recovery from high frequency stimulation. Finally, we show that restoring *Ube3a* function in only inhibitory neurons early in development prevents deficits in recovery from high frequency stimulation at inhibitory synapses and normalizes defects in synaptic vesicle cycling. Our findings suggest that specific synaptic phenotypes are due to loss of Ube3a from specific classes of neurons and that several defects in AS mice may require loss of Ube3a both pre and postsynaptically to become manifest.

3.3 Results

3.3.1 Generation and validation of Ube3a conditional knockout mouse

To explore the physiological and anatomical consequences of Ube3a loss in specific neuron classes in the brain we developed a conditional *Ube3a* knockout mouse. Using homologous recombination, a targeting vector containing loxP sites flanking exon 5 of *Ube3a* replaced the endogenous *Ube3a* gene creating a *Ube3a* conditional knockout allele (**Fig. 3.1A**). Mice carrying the conditional *Ube3a* allele on the maternally inherited chromosome ($Ube3a^{Flox/p+}$) were alive and fertile and displayed no

obvious behavioral abnormalities. Cortical lysates showed that Ube3a protein isolated from *Ube3a*$^{Flox/p+}$ mice ran at the same molecular weight as endogenous Ube3a indicating that knock-in of the *Ube3a* conditional allele did not affect Ube3a protein weight (**Fig. 3.1B**). We then crossed *Ube3a*$^{Flox/p+}$ mice to *Nestin-Cre* mice which express Cre in the entire central nervous system from early embryonic development (Graus-Porta et al., 2001; Tronche et al., 1999). We hypothesized that *Ube3a*$^{Flox/p+}$::*Nestin-Cre* mice would recapitulate phenotypes observed in *Ube3a* null mice (*Ube3a*$^{m-/p+}$) and that *Ube3a*$^{Flox/p+}$ mice would be identical to controls (wild-type +/- *Nestin-Cre*). Ube3a protein levels in neocortex of *Ube3a*$^{Flox/p+}$ were not different than control mice and *Ube3a*$^{Flox/p+}$::*Nestin-Cre* mice expressed similar levels of Ube3a as *Ube3a*$^{m-/p+}$ mice (**Fig 3.1C**). To assess synaptic phenotypes in control, *Ube3a*$^{Flox/p+}$, and *Ube3a*$^{Flox/p+}$::*Nestin-Cre* we performed whole-cell patch clamp electrophysiology on acute slices of L2/3 primary visual cortex. We recorded miniature inhibitory (mIPSCs) in L2/3 pyramidal neurons at adult ages (P70-P90) where synaptic phenotypes have been shown to exist in *Ube3a* maternal null mice (*Ube3a*$^{m-/p+}$) (Wallace et al., 2012). *Ube3a*$^{Flox/p+}$::*Nestin-Cre* mice had a significant decrease in mIPSC frequency compared to control and *Ube3a*$^{Flox/p+}$ mice (**Fig. 3.1G**) suggesting defects in synaptic transmission similar to those observed in *Ube3a*$^{m-/p+}$ mice. *Ube3a*$^{Flox/p+}$ mice did not show any change in mIPSC frequency compared to control mice indicating that *Ube3a*$^{Flox/p+}$ mice were similar to wild-type mice (**Fig. 3.1G**). Interestingly, *Ube3a*$^{Flox/p+}$::*Nestin-Cre* mice had a significant decrease in mIPSC amplitude compared to control mice and a strong trend for decreased amplitude compared to *Ube3a*$^{Flox/p+}$ mice (**Fig. 3.1F**). This effect

was not observed in *Ube3a*$^{m-/p+}$ mice (**Fig. 2.1**) and may indicate a change in GABA receptor number, occupancy, or subunit composition.

As *Ube3a*$^{m-/p+}$ mice have also been reported to have defects in evoked inhibitory neurotransmission, we recorded evoked IPSCs (eIPSCs) (**Fig. 3.1H**). *Ube3a*$^{Flox/p+}$::*Nestin-Cre* mice showed a significant decrease in eIPSC amplitude compared to control mice and a strong trend for reduced amplitude compared to *Ube3a*$^{Flox/p+}$ mice, suggesting *Ube3a*$^{Flox/p+}$::*Nestin-Cre* mice had decreased inhibitory synaptic strength (**Fig. 3.1J**). In summary, *Ube3a*$^{Flox/p+}$::*Nestin-Cre* mice harboring a new conditional *Ube3a* allele recapitulate the defects in cortical synaptic transmission seen in the AS mouse model (*Ube3a*$^{m-/p+}$). Furthermore, *Ube3a*$^{Flox/p+}$ mice are similar to control wild-type mice and serve as an excellent model to dissect cell class specific contributions of Ube3a loss to the aforementioned synaptic phenotypes.

3.3.2 Conditional deletion of *Ube3a* from all GABAergic inhibitory interneurons

Having validated the conditional *Ube3a* knockout mouse, we investigated the effects of Ube3a loss in specific neuron classes to synaptic phenotypes. We hypothesized that Ube3a loss in GABAergic neurons would have effects on inhibitory synaptic phenotypes, and Ube3a loss in excitatory pyramidal neurons would have effects on excitatory synaptic phenotypes. We crossed the *Ube3a*^{Flox} line to a line which expresses Cre in almost all GABAergic neurons in the cortex (*Gad2-Cre*) to investigate the effects of Ube3a loss in only GABAergic neurons (Taniguchi et al., 2011). This breeding scheme produced WT (+/- *Gad2-Cre*), *Ube3a*$^{Flox/p+}$, and *Ube3a*$^{Flox/p+}$::*Gad2-Cre* mice. Because we saw no differences between the WT (+/- Cre) and *Ube3a*$^{Flox/p+}$

mice in the cross with *Nestin-Cre* (**Fig. 3.1**), we combined the WT (+/- *Gad2-Cre*) and *Ube3a*$^{Flox/p+}$ groups into a single "control" group for remaining experiments. To compare the effects of Ube3a loss in GABAergic neurons we again performed whole cell patch clamp recordings in L2/3 pyramidal neurons (**Fig. 3.2**). Surprisingly, unlike *Ube3a*$^{Flox/p+}$::*Nestin-cre*, *Ube3a*$^{Flox/p+}$::*Gad2-Cre* mice did not show changes in mIPSC or mEPSC frequency or amplitude compared to controls (**Fig. 3.2A-H**). Defects in evoked inhibitory neurotransmission observed in *Ube3a*$^{Flox/p+}$::*Nestin-Cre* mice were also absent in *Ube3a*$^{Flox/p+}$::*Gad2-Cre* mice when compared against controls (**Fig. 3.2K**). Finally, deleting *Ube3a* in GABAergic neurons was insufficient to produce defects in synaptic recovery from high frequency stimuli seen in *Ube3a*$^{m-/p+}$ mice (**Fig. 2.7**), as *Ube3a*$^{Flox/p+}$::*Gad2-Cre* mice recovered to similar levels as controls following high frequency stimulation (**Fig. 3.2N**). These results suggest deletion of *Ube3a* in GABAergic neurons alone is not sufficient to produce any of the synaptic phenotypes seen when Ube3a is absent from all neurons.

3.3.3 Conditional deletion of *Ube3a* from all excitatory pyramidal neurons

As deletion of *Ube3a* from GABAergic neurons was insufficient to produce defects in synaptic transmission seen with global Ube3a loss we next sought to delete *Ube3a* from the other major class of neurons in the cortex, pyramidal neurons. To investigate the effects of Ube3a loss in pyramidal neurons, we crossed the *Ube3a*^{Flox} line to the *NEX-Cre* line which expresses Cre in all cortical pyramidal neurons (Goebbels et al., 2006). Again, we combined WT (+/- *NEX-Cre*) and *Ube3a*$^{Flox/p+}$ into one group labeled "control". We observed no change in mIPSC or mEPSC frequency or amplitude in *Ube3a*$^{Flox/p+}$::*NEX-Cre* mice compared to controls (**Fig. 3.3A-H**). However,

deleting *Ube3a* from all excitatory pyramidal neurons was sufficient to produce defects in evoked inhibitory neurotransmission as *Ube3a*$^{Flox/p+}$::*NEX-Cre* mice had decreased eIPSC amplitude compared to controls (**Fig. 3.3K**). Finally, as seen in *Ube3a*$^{Flox/p+}$::*Gad2-Cre* mice, *Ube3a*$^{Flox/p+}$::*NEX-Cre* mice recovered from high frequency stimuli to similar levels as controls (**Fig. 3.3N**). Taken together, data from *Ube3a*$^{Flox/p+}$::*Gad2-Cre* and *Ube3a*$^{Flox/p+}$::*NEX-Cre* suggest reductions in mIPSCs and mEPSCs may require loss of Ube3a from both GABAergic and pyramidal neurons. Also, loss of Ube3a in pyramidal neurons is sufficient to cause decreased eIPSC amplitude and loss of Ube3a in GABAergic neurons is not required for this phenotype (**Fig. 3.2K and 3.3K**). Finally, phenotypes relating to defects in recovery from high frequency stimuli likely require Ube3a loss in both presynaptic GABAergic neurons and postsynaptic pyramidal neurons. Therefore, depending on the synaptic phenotype, Ube3a loss in pyramidal neurons is either completely sufficient or completely insufficient at producing the particular synaptic defect.

3.3.4 Conditional reinstatement of *Ube3a* in all GABAergic inhibitory interneurons

One interpretation of the negative results presented from the *Ube3a*$^{Flox/p+}$::*Gad2-Cre* (**Fig. 3.2**) mouse is that Ube3a loss is required in additional cell types to produce the synaptic defects observed when Ube3a is lost globally. A second interpretation is that the *Gad2-Cre* line did not delete *Ube3a* early enough in development (E12-E15), and therefore missed the key time point to produce phenotypes seen in *Ube3a*$^{Flox/p+}$::*Nestin-Cre* mouse line (**Fig. 3.1**) where Cre is expressed by E11(Graus-Porta et al., 2001; Taniguchi et al., 2011). If the second interpretation were correct, then we reasoned we would also be unable to recover synaptic phenotypes in a *Ube3a*

null animal by re-expressing Ube3a with the *Gad2-Cre* line. To test this we took advantage of an additional conditional *Ube3a* mouse line which contains a STOP cassette flanked by loxP sites between exons 3 and 4 of *Ube3a* (*Ube3a*$^{STOP/p+}$) (**Fig. 3.4-3.7**). *Ube3a*$^{STOP/p+}$ mice do not express *Ube3a* in the absence of Cre, but when Cre is present the STOP cassette is excised and Ube3a is expressed at normal levels. This line was crossed with the *Gad2-Cre* line to create three genotypic groups, control (WT +/- *Gad2-Cre*), *Ube3a*$^{STOP/p+}$ and *Ube3a*$^{STOP/p+}$::*Gad2-Cre*. Histological analysis revealed that Cre mediated recombination efficiency was near 100% as almost all cortical GABAergic neurons (marked by parvalbumin, calretinin, and somatostatin) expressed Ube3a in the *Ube3a*$^{STOP/p+}$::*Gad2-Cre* mouse, but not in the *Ube3a*$^{STOP/p+}$ mice (**Fig. 3.4**) (Gonchar et al., 2007). We performed electrophysiological recordings and electron microscopy on these groups at adult ages (P70-P90). We first recorded mIPSCs and mEPSCs in L2/3 pyramidal neurons (**Fig. 3.5A-H**). Unfortunately, we did not observe mPSC defects in *Ube3a*$^{STOP/p+}$ mice (mice that should be similar to *Ube3a*$^{m-/p+}$ and *Ube3a*$^{Flox/p+}$::*Nestin-Cre* mice). Therefore we could not assess the impact of re-expressing *Ube3a* in inhibitory neurons on these phenotypes. We presume that the mPSC phenotypes were not present due to a small amount of transcriptional leak observed the in *Ube3a*$^{STOP/p+}$ mice (personal communication with Ype Elgersma). However, we did observe a significant decrease in eIPSC amplitude in the *Ube3a*$^{STOP/p+}$ mice compared to controls (**Fig. 3.5K**). *Ube3a*$^{STOP/p+}$::*Gad2-Cre* mice showed an eIPSC amplitude that was intermediate and not significantly different from either the control or *Ube3a*$^{STOP/p+}$ mice (**Fig. 3.5K**). We then examined synaptic recovery of the eIPSC following high frequency stimuli. *Ube3a*$^{STOP/p+}$ mice showed defects in recovery from

high frequency stimuli that was significantly decreased when compared to both control and *Ube3a*$^{STOP/p+}$::*Gad2-Cre* (**Fig. 3.5N**). Therefore, re-expression of Ube3a in GABAergic neurons was sufficient to normalize defects in recovery from synaptic depletion in the *Ube3a*$^{STOP/p+}$ mice. Our data from the *Ube3a*$^{STOP/p+}$::*Gad2-Cre* is consistent with our results in the *Ube3a*$^{Flox/p+}$::*NEX-Cre* which similarly have Ube3a expressed only GABAergic neurons in the cortex and do not show defects in recovery from high frequency stimulation. These data also suggest that the *Gad2-Cre* line expresses Cre early enough in development to ameliorate some GABAergic synaptic phenotypes and is unlikely to be the reason synaptic phenotypes are not present in the *Ube3a*$^{Flox/p+}$::*Gad2-Cre* line.

3.3.5 Synaptic vesicle cycling phenotypes following conditional reinstatement of *Ube3a* in all GABAergic inhibitory interneurons

In *Ube3a*$^{m-/p+}$ mice we observed a large increase in clathrin-coated vesicles (CCVs) in GABAergic axon terminals (**Fig. 2.7**) (Wallace et al., 2012). We posited that this was indicative of defective synaptic vesicle recycling and lead to the defects in synaptic recovery from high frequency depletion. Therefore, we hypothesized that changes in CCVs would mirror the changes in recovery from high frequency depletion we observed in the *Ube3a*$^{STOP/p+}$ mice. We performed immunogold electron microscopy and analyzed GABAergic axon terminals onto soma and dendrites in control, *Ube3a*$^{STOP/p+}$, and *Ube3a*$^{STOP/p+}$::*Gad2-Cre* mice (**Fig. 3.6 and 3.7**). Similar to *Ube3a*$^{m-/p+}$ mice we saw a significant increase in CCVs in the *Ube3a*$^{STOP/p+}$ mice compared to controls at GABAergic axon terminals onto soma and dendrites, but observed no change in terminal area, mitochondrial area, or synaptic vesicle density

(**Fig. 3.6B-D and 3.7B-D**). Consistent with our electrophysiological findings, we observed a normalization of CCV density at GABAergic axon terminals onto both soma and dendrites in the *Ube3a*$^{STOP/p+}$::*Gad2-Cre* mice compared to controls (**Fig. 3.6E and 3.7E**). Therefore, re-expression of *Ube3a* in GABAergic neurons is sufficient to normalize increases in CCVs observed in mice which lack Ube3a from all neurons. Increased density of CCVs also tracks well with electrophysiological phenotypes (ie recovery from high frequency stimuli). Paradoxically, it is likely that there is no increase in CCV density in *Ube3a*$^{Flox/p+}$::*Gad2-Cre* mice, even though Ube3a is not present in GABAergic neurons, because these mice do not show decreased recovery from high frequency stimulation. Rather, it is probable that Ube3a loss is required both pre and postsynaptically for the expression of this phenotype.

3.4 Discussion

This work introduces several new conditional *Ube3a* mouse lines that allow detailed dissection of the role of Ube3a in specific neural circuits. In this study we chose to investigate excitatory and inhibitory circuits in the visual cortex and found differential effects of conditional *Ube3a* deletion and reinstatement on excitatory and inhibitory synapses.

We hypothesized that Ube3a loss in GABAergic neurons would have effects on one set of synaptic phenotypes, and Ube3a loss in excitatory pyramidal neurons would have effects on others. Our findings suggest that for several synaptic phenotypes (mIPSCs and recovery from synaptic depletion) loss of Ube3a both pre and postsynaptically is required for the defect to manifest. Conversely, Ube3a loss in

excitatory neurons alone is sufficient for defects in evoked inhibitory neurotransmission. Consequently, for the synaptic phenotypes investigated, Ube3a loss in excitatory neurons is either completely sufficient for the synaptic phenotype or completely insufficient (**Fig. 3.3 and 3.5**). Furthermore, Ube3a loss in inhibitory neurons is insufficient to produce any of the synaptic phenotypes assayed (**Fig. 3.2**).

Previous observations of synaptic phenotypes at GABAergic synapses in *Ube3a*$^{m-/p+}$ mice lead us to conclude that there existed defects in synaptic vesicle cycling (Wallace et al., 2012). Many of the known molecular mechanisms regulating vesicle cycling are in the axon terminal (Slepnev and De Camilli, 2000). As such, we expected that Ube3a loss in the GABAergic neurons alone would be sufficient to cause synaptic vesicle cycling defects in GABAergic neurons. Our results indicate that this is unlikely to be the case as Ube3a loss in GABAergic neurons in the *Ube3a*$^{Flox/p+}$::*Gad2-Cre* mice does not result in electrophysiological phenotypes that indicate defects in vesicle cycling (**Fig 3.2N**). Paradoxically, expressing Ube3a in GABAergic neurons alone in the *Ube3a*$^{STOP/p+}$::*Gad2-Cre* mice prevents defects in synaptic vesicle cycling at GABAergic axon terminals (**Fig 3.5N**). Together these findings suggest that Ube3a loss is required in both the presynaptic GABAergic neuron and the postsynaptic pyramidal neuron in order to result in synaptic vesicle cycling defects. It is also possible, while more complex, that Ube3a deficient GABAergic neurons are primed for defects in vesicle cycling but dysfunction does not arise until Ube3a loss occurs in pyramidal neurons triggering the observed vesicle cycling defect. More subtle manipulations of cell type and number will be required to definitely determine the link between Ube3a loss and synaptic vesicle cycling defects.

While loss of Ube3a in GABAergic neurons did not result in any synaptic phenotype, loss of Ube3a in pyramidal neurons resulted in decreased evoked IPSC amplitude (**Fig. 3.3K**). Interestingly, decreased eIPSC amplitude occurred in the absence of defects in mIPSCs and synaptic vesicle cycling and is most likely due to decreased GABA receptors on the postsynaptic pyramidal neuron. However, because mIPSC amplitude is unchanged it is likely that the decrease in GABA receptors occurs extrasynaptically and is only evident when GABA is released in large quantities during strong stimulation (Ye et al., 2013). A decrease in extrasynaptic GABA receptor function has already been reported in AS model mice in cerebellar granule neurons (Egawa et al., 2012). Also, similar to cerebellar granule neurons L2/3 pyramidal neurons express high levels of extrasynaptic GABA receptors (Jang et al., 2013). Intriguingly, L2/3 pyramidal neurons have an increased membrane resistance in *Ube3a*$^{m-/p+}$ mice only when GABA receptors are unblocked (**Table. 2.1 and 2.2**) suggesting a decrease in tonically active extrasynaptic GABA receptors. Electrophysiology experiments examining extrasynaptic GABA receptor mediated currents will be critical to resolve this issue. It is also of interest to determine if eIPSC amplitude defects are cell-autonomous. This could be addressed by sparsely deleting *Ube3a* from pyramidal neurons and examining eIPSC amplitude in control and Ube3a deficient neurons.

The work presented here provides a general framework for further investigations into the synaptic phenotypes resulting from Ube3a loss. A crucial future experiment will be to test for inhibitory synaptic recovery from depletion when Ube3a is lost both pre and postsynaptically. This can be achieved by sparsely deleting *Ube3a* in pyramidal

neurons in the *Ube3a*$^{Flox/p+}$::*Gad2-Cre* mice and then recording from neighboring pyramidal neurons that either express or lack Ube3a while Ube3a is absent from all GABAergic neurons. Sparse expression of Cre in pyramidal neurons can be achieved by a perinatal intracerebroventricular injection of AAV-Cre virus or with tamoxifen inducible Cre lines that allow sparse activation of Cre (Agarwal et al., 2012; Chakrabarty et al., 2013; Madisen et al., 2010). In these experiments the vast majority of the pyramidal neurons will contain Ube3a and we will be able to either rule in or out the possibility that GABAergic neurons are primed for, but not expressing, vesicle cycling defects.

In conclusion, our hypothesis that Ube3a loss in inhibitory neurons governed inhibitory synaptic phenotypes, and Ube3a loss in excitatory neurons governed excitatory synaptic phenotypes, requires modification. Our data suggest that Ube3a loss in multiple cell types (both GABAergic and pyramidal) is required to produce several synaptic phenotypes and that deletion of *Ube3a* in a single neuronal type is insufficient for all phenotypes but one. Finally, we show reinstating Ube3a in a small population of neurons (~20% of cortical neurons are GABAergic) was sufficient to normalize defects in synaptic vesicle cycling. Thus, it is tantalizing to speculate that it may be sufficient to reinstate Ube3a in only a small population of neurons in order to achieve significant behavioral improvement.

3.5 Materials and Methods

3.5.1 Animals

Ube3a-deficient (*Ube3a*$^{m-/p+}$) mice backcrossed onto the C57BL/6J background were obtained from Yong-hui Jiang (Duke University). *Gad2*-Cre (JAX# 010802) and *Nestin-Cre* (JAX# 003771) mice were on the C57BL/6J background and were obtained from The Jackson Laboratory (www.jax.org). *NEX-Cre* mice were on the C57BL/6J background and originally described by (Goebbels et al., 2006). *Ube3a*^{Floxed} mice were generated at the UNC Animal Models Core on a C57BL/6J background (see below for details). *Ube3a*^{Stop} mice were generously provided by Ype Elgersma on the 129Sv/Pas background and were crossed to *Gad2-Cre* mice to create F2 or F4 hybrid (C57BL/6J / 129SvPas) mice that were used for Figures 3.4-3.7. Mice of both genders were used at postnatal day (P) 70-90. Experimental groups were obtained by crossing a paternal-Flox (or paternal-STOP) heterozygous female (*Ube3a*$^{m+/Flox(or\ STOP)}$ mice) with a male heterozygous for *Cre*. Mice were raised on a 12-h light/dark cycle and fed *ad libitum*. All studies were conducted with protocols approved by the University of North Carolina at Chapel Hill Animal Care and Use Committee.

Mouse Transgenics

The gene targeting construct used for to create the *Ube3a*^{Flox} allele was generated by the trans-NIH Knock-Out Mouse Project (KOMP) and obtained from the KOMP Repository (www.komp.org). Using knockout first technology (Skarnes et al., 2011) we validated the construct prior to embryonic stem cell culture and gene targeting. Gene targeting, identification of correctly targeted clones, Southern blotting,

ES cell blastocyst injections and transfer to pseudopregnant females were performed by the UNC Animal Models Core using standard methods (www.med.unc.edu/amc). Chimeric pups were identified by coat color and crossed to a mouse line containing Flpe recombinase (JAX# 009086) on a C57BL/6J background to remove the gene trap and create *Ube3a*^{Flox} founder mice.

3.5.2 Coronal Slice Preparation

Mice (P70-P90) were anesthetized with pentobarbital (40 mg/kg) and, after disappearance of corneal reflexes, intracardially perfused with dissection buffer (in mM: 87 NaCl, 2.5 KCl, 1.25 NaH_2PO_4, 26 $NaHCO_3$, 75 sucrose, 10 dextrose, 1.3 ascorbic acid, 7 $MgCl_2$, and 0.5 $CaCl_2$ bubbled with 95% O_2-5% CO_2). Brains were then rapidly removed and immersed in ice-cold dissection buffer. The visual cortices were dissected and 350 μm coronal slices were prepared using a vibrating microtome (Leica VT1200s). Slices were allowed to recover for 20 min in a 35º C submersion chamber filled with oxygenated artificial cerebrospinal fluid (ACSF) (in mM; 124 NaCl, 3 KCl, 1.25 NaH_2PO_4, 26 $NaHCO_3$, 1 $MgCl_2$ 2 $CaCl_2$ and 20 glucose) and then kept at room temperature for >40 min until use (Philpot et al., 2003).

3.5.3 Voltage-clamp Recordings

To isolate miniature inhibitory postsynaptic currents (mIPSCs), slices were placed in a submersion chamber, maintained at 30º C and perfused at 2 ml/min with oxygenated ACSF (as described above) containing (in μM): 20 6,7-dinitroquinoxaline-2,3-dione (DNQX), 100 D,L-2-amino-5-phosphonopentanoic acid (APV), and 1.0

tetrodotoxin (TTX). L2/3 pyramidal neurons between 20-150 μm ventral from the L1-2 boundary were targeted for recording. Cells were visualized using a Ziess Axioskop microscope equipped with infrared differential interference contrast (IR-DIC) optics. Patch pipettes were pulled from thick-walled borosilicate glass (P2000, Sutter Instruments Novato, CA). Open tip resistances were between 2-5 MΩ when pipettes were filled with the internal solution containing (in mM): 100 $CsCH_3SO_3$, 15 CsCl, 2.5 $MgCl_2$, 5 Cs-Bapta, 4 Mg-ATP, 0.3 Na-GTP, 10 HEPES, 5 QX-314-Cl, and 0.025 Alexa-568 with pH adjusted to 7.25 with 1M CsOH and osmolarity adjusted to ~295 mOsm by addition of sucrose. Voltage-clamp recordings were performed at 0 mV in the whole-cell configuration using patch-clamp amplifier (Multiclamp 700A, Molecular Devices), and data were acquired at 10 kHz filtered at 2 kHz and analyzed using pClamp 10.2 (Molecular Devices) and MATLAB (Mathworks) software. Pipette seal resistances were **>** 1 GΩ, and pipette capacitive transients were minimized prior to breakthrough. Changes in series and input resistance were monitored throughout the experiment by giving test pulse every 30 s and measuring the amplitude of the capacitive current. Cells were discarded if series resistance or input resistance changed by >25%.

For evoked IPSCs, the internal solution was identical to the solution used for mIPSCs. The ASCF was identical to solution described above, but tetrodotoxin was not added. IPSCs were evoked from a stimulating electrode (concentric bipolar; 200 μM tip separation) placed in 150 μm ventral of the recorded neuron, and stimulation was delivered for 200 μs.

mEPSCs were recorded at -70 mV in ACSF containing (in μM) 1.0 TTX, 100 APV, and 50 picrotoxin. The internal solution was identical to the solution used for mIPSCs.

3.5.4 Western Blotting.

Mice were deeply anesthetized with sodium pentobarbital (60 mg/kg i.p.) prior to decapitation and brain removal. The neocortical hemispheres from each harvested brain were rapidly dissected in ice-cold PBS and then immediately snap-frozen with liquid nitrogen and stored at -80°C. Frozen tissue samples were homogenized in a glass tissue homogenizer (Wheaton, Millville, NJ, USA) with ice-cold RIPA buffer (50 mM Tris pH 8.0, 150 mM NaCl, 1% triton x-100, 0.1% SDS, 0.5% Na Deoxycholate) supplemented with 2 mM EDTA and a protease inhibitor cocktail (Sigma, Saint Louis, MO, USA). Tissue homogenates were cleared by 16,000 x g centrifugation for 20 minutes at 4°C and protein concentrations of the supernatants were determined using the BCA assay (Thermo Scientific). Protein samples (30 μg per lane) were resolved by SDS-PAGE and transferred to nitrocellulose membranes. Membranes were blocked for 1 hour at room temperature in Odyssey blocking buffer (Li-COR, Lincoln, NE, USA) prior to incubation overnight at 4°C with primary antibodies diluted in a 1:1 solution of blocking buffer and Tris-buffered saline containing 0.1% Tween-20 (TBS-Tween). The following primary antibodies were used mouse anti-Ube3a 1:1000 (Sigma) and mouse anti-Gapdh (Millipore). Membranes were subsequently washed repeatedly with TBS-Tween prior to incubation for 1 hour at room temperature with secondary antibodies prepared in the same diluent as the primary antibodies. The following secondary

antibodies were used: 1:10,000 donkey anti-mouse 800CW (LICOR, 926-32212). Finally, blots were washed repeatedly in TBS-Tween followed by TBS alone prior to imaging with the Odyssey imaging system (LI-COR).

3.5.5 Immunohistochemistry

Light Microscopy

Histology was performed on visual cortices of ~P80 mice that were intracardially perfused with ~80 mL of 4% paraformaldehyde (PB, 0.1 M, pH 6.8) and sliced sagitally at 40-60 µm on a freezing sliding microtome (Ziess HM430). Slices were then washed in 0.1 M PBS, permeabilized in 0.2% Triton-X and blocked in 5% normal goat serum. Primary antibodies were incubated 48hrs at 4ºC at the following concentrations: mouse anti-Ube3a 1:750 (Sigma), rabbit anti-parvalbumin 1:500 (Swant), rabbit anti-calretinin 1:1000 (Swant), rabbit anti-somatostatin 1:1000 (Peninsula, Cat# T-4103). Secondary antibodies were incubated at 1:500 for 1 hr at room temp and tissue was mounted on slides. Primary visual cortex (layers 1-6) was imaged on a Zeiss LSM 710 Confocal Microscope using 20×/0.8 NA objective.

Electron Microscopy

Mice were intracardially perfused with 0.9% saline solution for 1 min, followed by a mixture of depolymerized 2% paraformaldehyde and 2% glutaraldehyde (Electron Microscopy Science) in 0.1 M phosphate buffer, pH 6.8. Brains were removed and postfixed overnight in the same fixative. 50 µm-thick sections were cut on a Vibratome, incubated 1 hr in 1% osmium tetroxide in 0.1 M phosphate buffer (pH 6.8), rinsed in 0.1

M maleate buffer (pH 6.0), and incubated in 1% uranyl acetate in maleate. Sections were dehydrated in ethanol, infiltrated with Spurr resin, and flat-embedded between sheets of ACLAR plastic. Chips of tissue were cut from heat-polymerized wafers and glued to plastic blocks; thin (~70 nm) sections were collected on copper mesh grids and poststained with uranyl acetate and Sato's lead.

Postembedding immunocytochemistry was performed as previously described (Phend et al., 1992). Nickel grids were pre-treated using 0.01M citrate buffer (pH 6, at 60°C for 15 mins) and blocked in 1% bovine serum albumin in Tris-buffered saline with 0.005% Tergitol NP-10 (TBSN, pH 7.6), then incubated overnight at 21–24 °C with the rabbit anti-GABA antibody (Sigma, A2052, 1:100,000). Grids were rinsed, blocked in 1% normal goat serum in TBSN (pH 8.2), and incubated in goat anti-rabbit conjugated to 20 nm gold particles (BBI, EM.GAR20) for 2 h, rinsed, then counterstained with 1% uranyl acetate followed by Sato's lead. Electron micrographs were collected with a Philips Tecnai microscope at 80 KV.

Analysis

Inhibitory presynaptic terminals from three mice per genotype were analyzed (at least 20 terminals per animal for each class). Inhibitory terminals were identified by GABA staining.

Parameters measured included cross-sectional area of the presynaptic terminal and mitochondria within, number of synaptic vesicles, and number of clathrin-coated vesicles. All morphometric analyses were performed by an anatomist blinded with respect to genotype.

3.5.6 Statistics

All experiments and analyses were performed blind to genotype. One way ANOVA was used to test for significance for mIPSCs, mEPSCs, and changes in CCV density in Fig. 3.1, 3.5, 3.6, and 3.7. Unpaired t-tests were used in for mIPSCs and mEPSCs in Fig 3.2 and 3.3. For eIPSC, depletion, and recovery analyses we employed a 2-way ANOVA to assess significance. Graphs represent the mean and error bars represent the SEM. For all figures p-values are as follows *$p<0.05$, **$p<0.01$, ***$p<0.001$. All statistics were performed in Graphpad Prism 6.

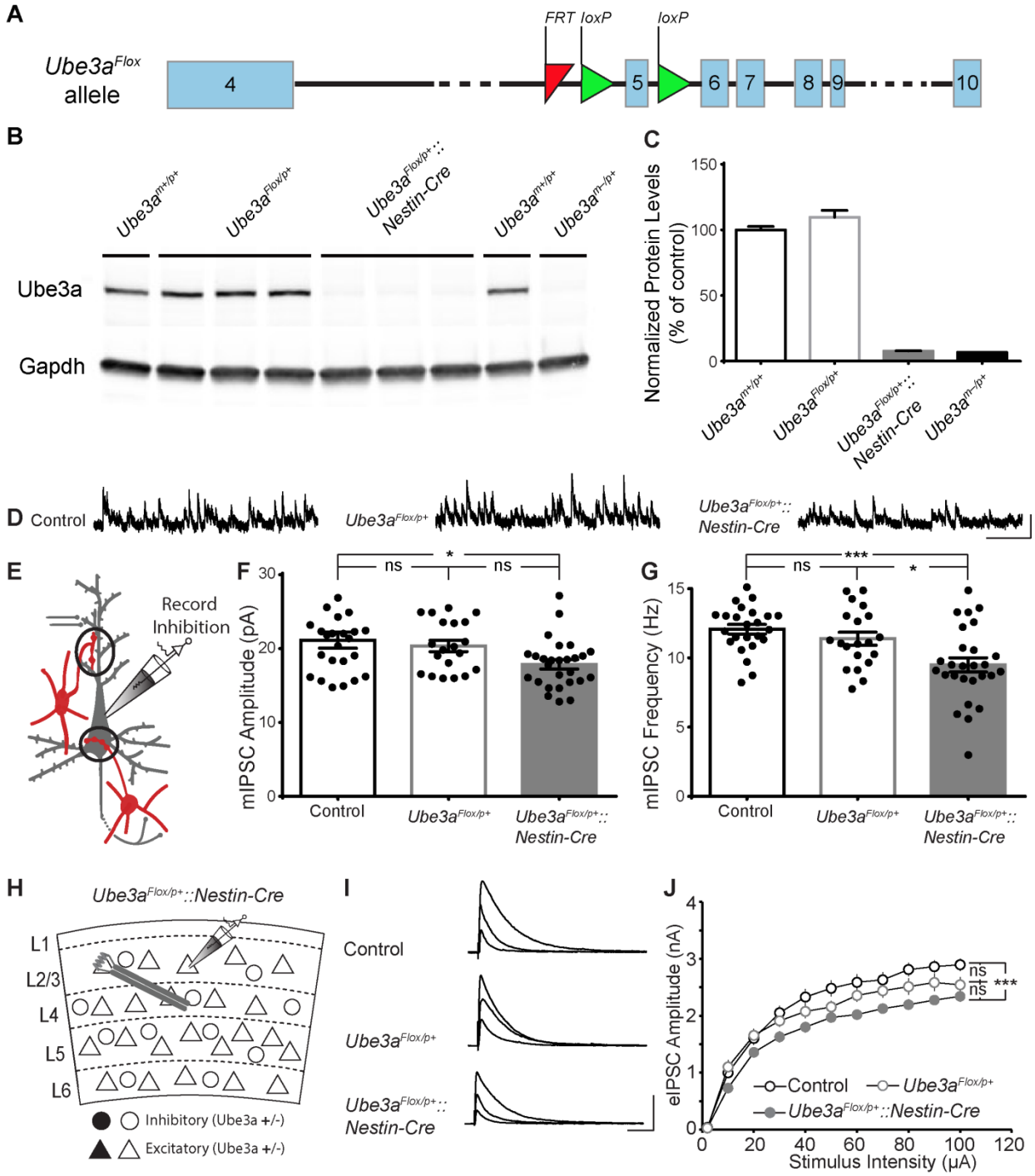

Figure 3.1 Generation and validation of conditional *Ube3a* knockout mice.

(**A**) Schematic (not to scale) depicting the *Ube3a*^{Flox} knock-in allele, which can be conditionally deleted via Cre/loxP recombination of exon 5. (**B**) Western blot of

neocortical lysates prepared from control (*Ube3a*$^{m+/p+}$), maternal floxed mice (*Ube3a*$^{Flox/p+}$), maternal floxed mice crossed to *Nestin-Cre* (*Ube3a*$^{Flox/p+}$::*Nestin-Cre*), and maternal null mice (*Ube3a*$^{m-/p+}$). Gapdh serves as a control for equal protein loading. (**C**) Quantified protein levels for different mouse lines shown in (**B**), (*Ube3a*$^{m+/p+}$ n=3, *Ube3a*$^{Flox/p+}$ n=5, *Ube3a*$^{Flox/p+}$::*Nestin-Cre* n=6, and *Ube3a*$^{m-/p+}$ n=2 animals). (**D**) Sample recordings and (**E**) recording configuration for mIPSCs from control, *Ube3a*$^{Flox/p+}$ and *Ube3a*$^{Flox/p+}$::*Nestin-Cre* mice (scale bar = 20 pA, 200 ms). Average mIPSC (**F**) amplitude and (**G**) frequency from control, *Ube3a*$^{Flox/p+}$ and *Ube3a*$^{Flox/p+}$::*Nestin-Cre* mice (control n=24 cells; *Ube3a*$^{Flox/p+}$ n=20 cells; *Ube3a*$^{Flox/p+}$::*Nestin-Cre* n=27 cells) in L2/3 pyramidal cells. (**H**) Illustration of stimulation and recording (L2/3 pyramidal neuron) configuration in primary visual cortex, and sample recordings (**I**) of evoked IPSCs at stimulation intensities of 10, 20, and 100 μA (scale bar = 1000 pA, 60 ms). (**J**) Evoked IPSCs are decreased in *Ube3a*$^{Flox/p+}$ *:: Nestin-Cre* mice compared to controls, but *Ube3a*$^{Flox/p}$ mice are not different from controls or *Ube3a*$^{STOP/p+}$ *::Nestin-Cre* mice (control n=22 cells; *Ube3a*$^{Flox/p+}$ n=16 cells; *Ube3a*$^{Flox/p+}$::*Nestin-Cre* n=33 cells). All data are represented as the mean ± SEM (*p<0.05, ***p<.001).

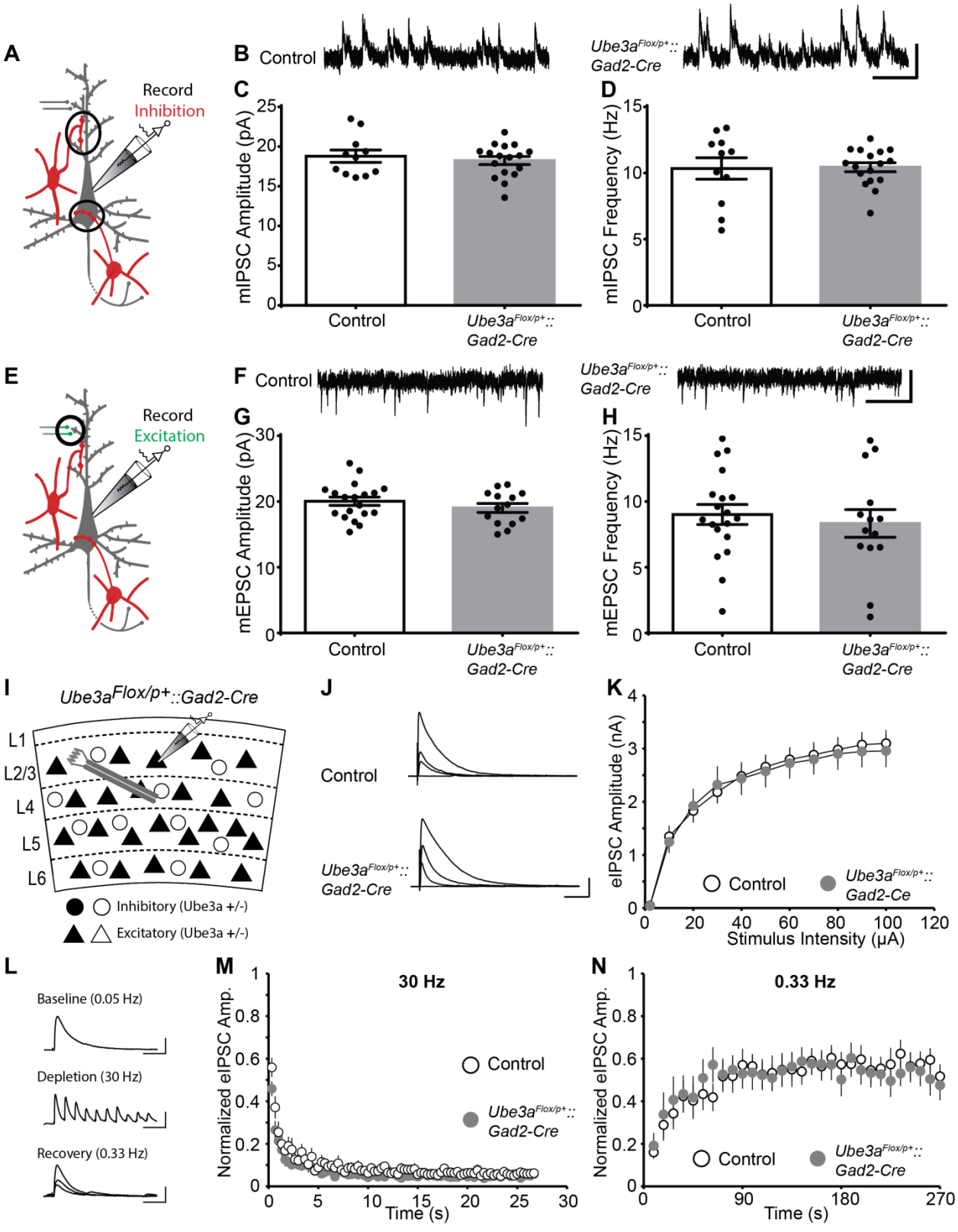

Figure 3.2 Lack of synaptic phenotypes in *Ube3a*$^{Flox/p+}$::*Gad2-Cre* mice

(**A**) Recording configuration for mIPSCs, and (**B**) sample recordings from control and *Ube3a*$^{Flox/p+}$::*Gad2-Cre* mice (scale bar = 20 pA, 200 ms). Average mIPSC (**C**) amplitude and (**D**) frequency was similar between control and *Ube3a*$^{Flox/p+}$::*Gad2-Cre* mice (control n=11 cells; *Ube3a*$^{Flox/p+}$::*Gad2-Cre* n=17) in L2/3 pyramidal cells. (**E**) Recording configuration for mEPSCs, and (**F**) sample recordings from control and *Ube3a*$^{Flox/p+}$::*Gad2-Cre* mice (scale bar = 20 pA, 200 ms). Average mEPSC (**G**) amplitude and (**H**) frequency was similar between control and *Ube3a*$^{Flox/p+}$::*Gad2-Cre* mice (control n=19 cells; *Ube3a*$^{Flox/p+}$::*Gad2-Cre* n=14) in L2/3 pyramidal cells. (**I**) Illustration of stimulation and recording (L2/3 pyramidal neuron) configuration in primary visual cortex, and sample recordings (**J**) of evoked IPSCs at stimulation intensities of 0, 10, 20, and 100 μA (scale bar = 1000 pA, 60 ms). (**K**) Evoked IPSCs are similar between control and *Ube3a*$^{Flox/p+}$::*Gad2-Cre* mice (control n=12 cells; *Ube3a*$^{Flox/p+}$::*Gad2-Cre* n=11). (**L**) Sample recordings showing baseline (top), high frequency depletion (middle), and recovery (bottom) phases (scale bars; baseline = 200 pA, 20 ms; depletion = 200 pA, 70 ms; recovery = 200 pA, 20 ms). (**M**) Average depletion phase showing eIPSC amplitude normalized to baseline during 800 stimuli at 30 Hz. 10 responses are averaged for each point (control n=11; *Ube3a*$^{Flox/p+}$::*Gad2-Cre* n=9). (**N**) Average recovery phase showing eIPSC amplitude normalized to baseline during 90 stimuli at 0.33 Hz. 3 responses are averaged for each point (control n=11; *Ube3a*$^{Flox/p+}$::*Gad2-Cre* n=9). All data are represented as the mean ± SEM.

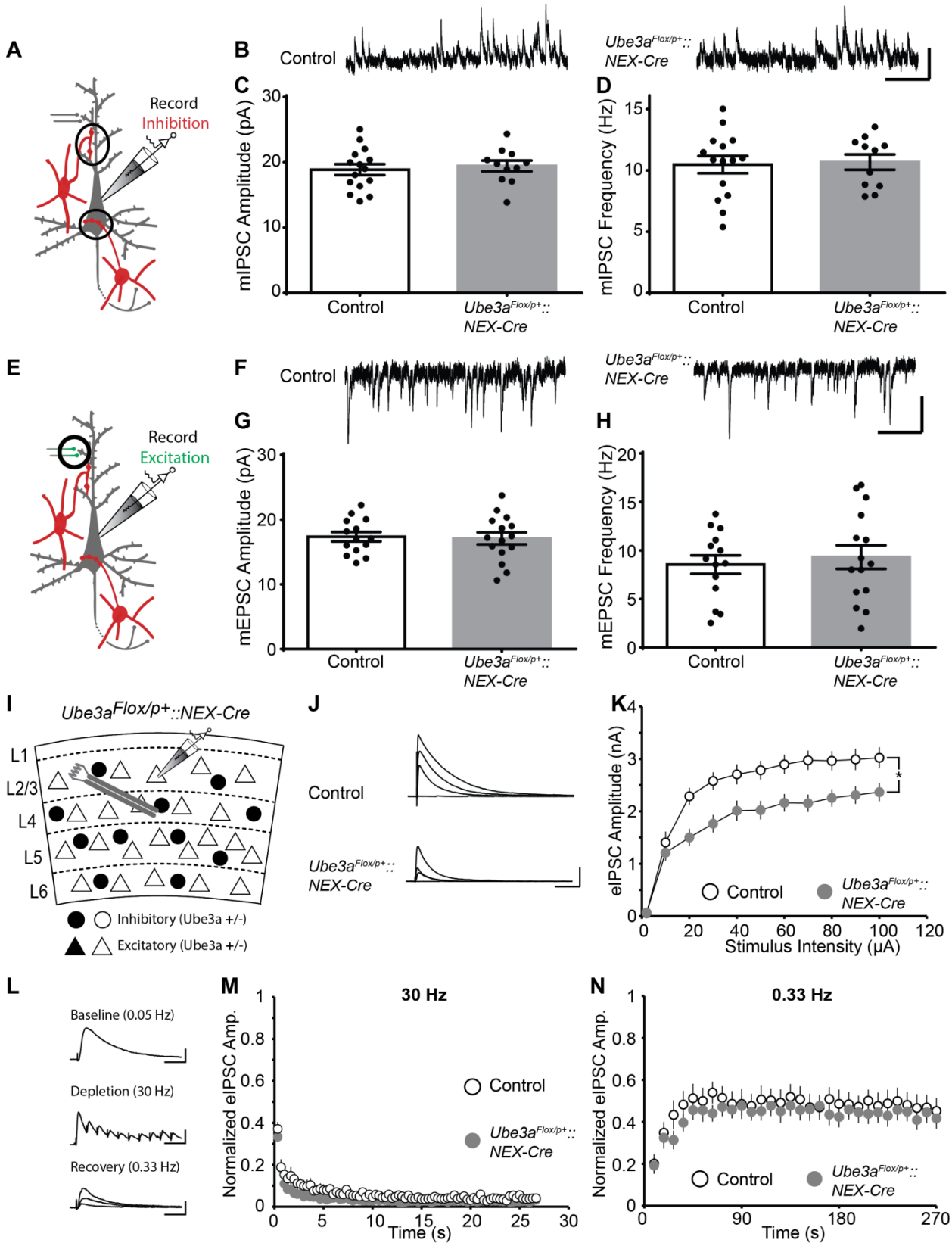
A
Record
Inhibition
B
Control
Ube3a Flox/p+:: NEX-Cre
C
mIPSC Amplitude (pA)
Control
Ube3a Flox/p+:: NEX-Cre
D
mIPSC Frequency (Hz)
Control
Ube3a Flox/p+:: NEX-Cre
E
Record
Excitation
F
Control
Ube3a Flox/p+:: NEX-Cre
G
mEPSC Amplitude (pA)
Control
Ube3a Flox/p+:: NEX-Cre
H
mEPSC Frequency (Hz)
Control
Ube3a Flox/p+:: NEX-Cre
I
Ube3a Flox/p+::NEX-Cre
L1
L2/3
L4
L5
L6
Inhibitory (Ube3a +/-)
Excitatory (Ube3a +/-)
J
Control
Ube3a Flox/p+:: NEX-Cre
K
eIPSC Amplitude (nA)
Control
Ube3a Flox/p+:: NEX-Cre
Stimulus Intensity (μA)
L
Baseline (0.05 Hz)
Depletion (30 Hz)
Recovery (0.33 Hz)
M
30 Hz
Normalized eIPSC Amp.
Control
Ube3a Flox/p+:: NEX-Cre
Time (s)
N
0.33 Hz
Normalized eIPSC Amp.
Control
Ube3a Flox/p+:: NEX-Cre
Time (s)

Figure 3.3 Loss of Ube3a in cortical pyramidal neurons in *Ube3a$^{Flox/p+}$*::*NEX-Cre* mice is sufficient for some, but not all synaptic phenotypes.

(**A**) Recording configuration for mIPSCs, and (**B**) sample recordings from control and *Ube3a$^{Flox/p+}$*::*NEX-Cre* mice (scale bar = 20 pA, 200 ms). Average mIPSC (**C**) amplitude and (**D**) frequency was similar between control and *Ube3a$^{Flox/p+}$*::*NEX-Cre* mice (control n=15 cells; *Ube3a$^{Flox/p+}$*::*NEX-Cre* n=11) in L2/3 pyramidal cells. (**E**) Recording configuration for mEPSCs, and (**F**) sample recordings from control and *Ube3a$^{Flox/p+}$*::*NEX-Cre* mice (scale bar = 20 pA, 200 ms). Average mEPSC (**G**) amplitude and (**H**) frequency was similar between control and *Ube3a$^{Flox/p+}$*::*NEX-Cre* mice (control n=14 cells; *Ube3a$^{Flox/p+}$*::*NEX-Cre* n=15) in L2/3 pyramidal cells. (**I**) Illustration of stimulation and recording (L2/3 pyramidal neuron) configuration in primary visual cortex, and sample recordings (**J**) of evoked IPSCs at stimulation intensities of 0, 10, 20, and 100 μA (scale bar = 1000 pA, 60 ms). (**K**) Evoked IPSC amplitude is decreased in *Ube3a$^{Flox/p+}$*::*NEX-Cre* mice compared to controls (control n=14 cells; *Ube3a$^{Flox/p+}$*::*NEX-Cre* n=22). (**L**) Sample recordings showing baseline (top), high frequency depletion (middle), and recovery (bottom) phases (scale bars; baseline = 200 pA, 20 ms; depletion = 200 pA, 70 ms; recovery = 200 pA, 20 ms). (**M**) Average depletion phase showing eIPSC amplitude normalized to baseline during 800 stimuli at 30 Hz. 10 responses are averaged for each point (control n=11; *Ube3a$^{Flox/p+}$*::*NEX-Cre* n=16). (**N**) Average recovery phase showing eIPSC amplitude normalized to baseline during 90 stimuli at 0.33 Hz. 3 responses are averaged for each point (control n=11; *Ube3a$^{Flox/p+}$*::*NEX-Cre* n=16). All data are represented as the mean ± SEM (*p<0.05).

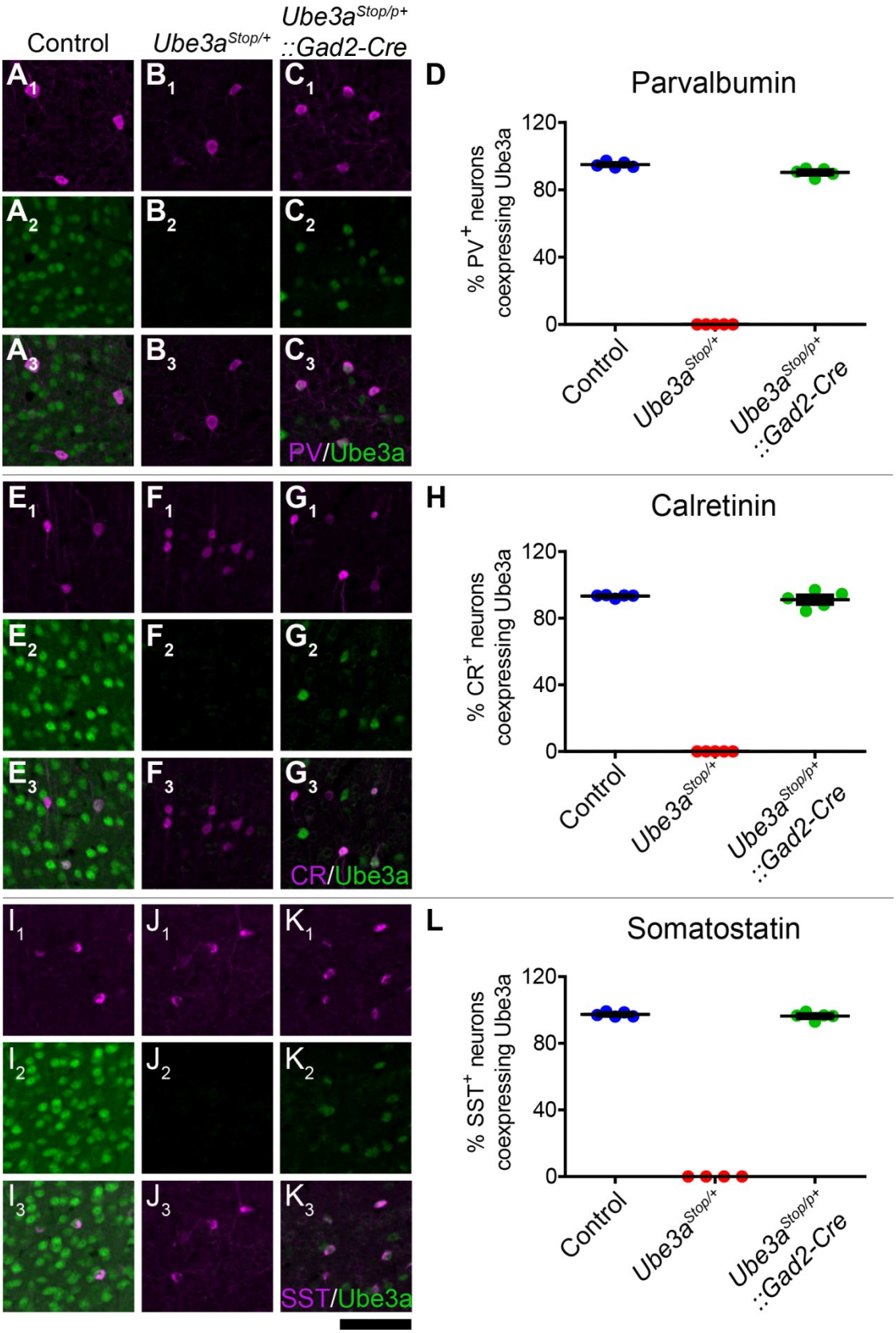
Control
Ube3a Stop/+
Ube3a Stop/p+ ::Gad2-Cre
A1
B1
C1
A2
B2
C2
A3
B3
C3
PV/Ube3a
D
Parvalbumin
% PV+ neurons coexpressing Ube3a
120
80
40
0
Control
Ube3a Stop/+
Ube3a Stop/p+ ::Gad2-Cre
E1
F1
G1
E2
F2
G2
E3
F3
G3
CR/Ube3a
H
Calretinin
% CR+ neurons coexpressing Ube3a
I1
J1
K1
I2
J2
K2
I3
J3
K3
SST/Ube3a
L
Somatostatin
% SST+ neurons coexpressing Ube3a

Figure 3.4 Highly efficient Cre mediated maternal Ube3a reinstatement across interneuron subclasses in *Ube3*$^{Stop/p+}$*::Gad2-Cre* mice.

(**A-C**) Co-immunohistochemical staining for parvalbumin (PV) and Ube3a in layer 2/3 visual cortex of control (**A$_{1-3}$**), *Ube3a*$^{Stop/p+}$ (**B$_{1-3}$**), and *Ube3a*$^{Stop/p+}$::*Gad2-Cre* (**C$_{1-3}$**). (**D**) Quantification of Ube3a coexpression in PV^{+} interneurons across all cortical layers. Values represent the mean percentage of coexpression for individual animals (n=5 animals per genotype). (**E-G**) Co-immunohistochemical staining for calretinin (CR) and Ube3a in layer 2/3 visual cortex of control (**E$_{1-3}$**), *Ube3a*$^{Stop/p+}$ (**F$_{1-3}$**), and *Ube3a*$^{Stop/p+}$::*Gad2-Cre* (**G$_{1-3}$**). (**H**) Quantification of Ube3a coexpression in CR^{+} interneurons across all cortical layers (n=5 animals per genotype). (**I-K**) Co-immunohistochemical staining for somatostatin (SST) and Ube3a in layer 2/3 visual cortex of control (**I$_{1-3}$**), *Ube3a*$^{Stop/p+}$ (**J$_{1-3}$**), and *Ube3a*$^{Stop/p+}$*::Gad2-Cre* (**K$_{1-3}$**). (**L**) Quantification of Ube3a coexpression in SST^{+} interneurons across all cortical layers (n=5 animals for control and *Ube3a*$^{Stop/p+}$*::Gad2-Cre* and 4 animals for *Ube3a*$^{Stop/p+}$). Animal averages ± SEM are indicated. Scale bar = 75 μm.

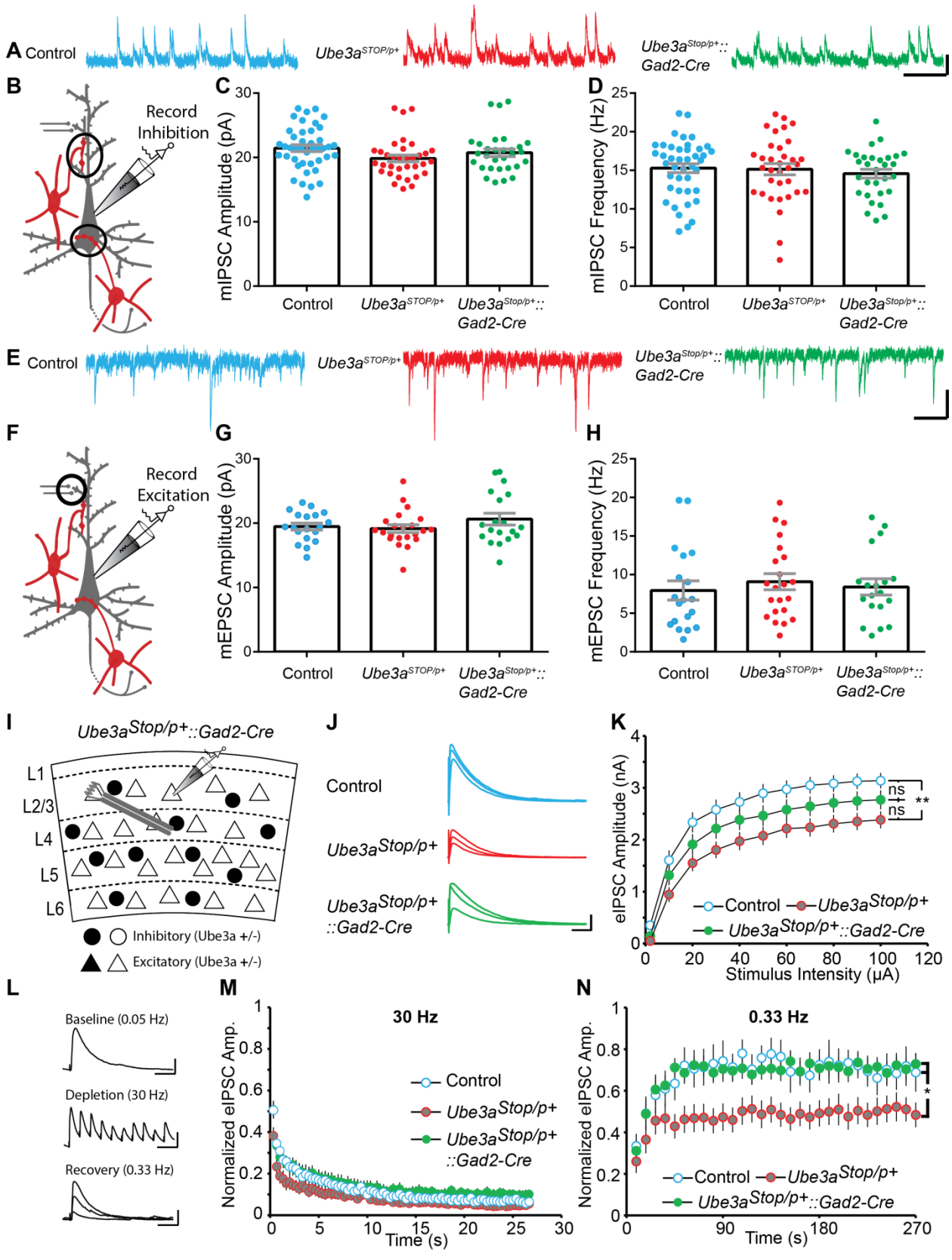
A Control
Ube3a STOP/p+
Ube3a Stop/p+::Gad2-Cre
B
Record Inhibition
C
mIPSC Amplitude (pA)
Control
Ube3a STOP/p+
Ube3a Stop/p+::Gad2-Cre
D
mIPSC Frequency (Hz)
E Control
F
Record Excitation
G
mEPSC Amplitude (pA)
H
mEPSC Frequency (Hz)
I
Ube3a Stop/p+::Gad2-Cre
L1
L2/3
L4
L5
L6
Inhibitory (Ube3a +/-)
Excitatory (Ube3a +/-)
J
Control
Ube3a Stop/p+
Ube3a Stop/p+ ::Gad2-Cre
K
eIPSC Amplitude (nA)
ns
ns
**
Control
Ube3a Stop/p+
Ube3a Stop/p+::Gad2-Cre
Stimulus Intensity (μA)
L
Baseline (0.05 Hz)
Depletion (30 Hz)
Recovery (0.33 Hz)
M
30 Hz
Normalized eIPSC Amp.
Control
Ube3a Stop/p+
Ube3a Stop/p+ ::Gad2-Cre
Time (s)
N
0.33 Hz
Normalized eIPSC Amp.
*
Control
Ube3a Stop/p+
Ube3a Stop/p+::Gad2-Cre
Time (s)

Figure 3.5 Reinstatement of Ube3a in GABAergic neurons in *Ube3a*$^{STOP/p+}$::*Gad2-Cre* mice restores defects synaptic recovery.

(**A**) Sample recordings and (**B**) recording configuration for mIPSCs from control, *Ube3a*$^{STOP/p+}$ and *Ube3a*$^{STOP/p+}$::*Gad2-Cre* mice (scale bar = 20 pA, 200 ms). Average mIPSC (**C**) amplitude and (**D**) frequency was similar between control, *Ube3a*$^{STOP/p+}$ and *Ube3a*$^{STOP/p+}$::*Gad2-Cre* mice (control n=43 cells; *Ube3a*$^{STOP/p+}$ n=34 cells; *Ube3a*$^{STOP/p+}$::*Gad2-Cre* n=30 cells) in L2/3 pyramidal cells. (**E**) Sample recordings and (**F**) recording configuration for mEPSCs from control, *Ube3a*$^{STOP/p+}$ and *Ube3a*$^{STOP/p+}$::*Gad2-Cre* mice (scale bar = 20 pA, 200 ms). Average mEPSC (**G**) amplitude and (**H**) frequency was similar between control, *Ube3a*$^{STOP/p+}$ and *Ube3a*$^{STOP/p+}$::*Gad2-Cre* mice (control n=19 cells; *Ube3a*$^{STOP/p+}$ n=22 cells; *Ube3a*$^{STOP/p+}$::*Gad2-Cre* n=19 cells) in L2/3 pyramidal cells. (**I**) Illustration of stimulation and recording (L2/3 pyramidal neuron) configuration in primary visual cortex, and sample recordings (**J**) of evoked IPSCs at stimulation intensities of 0, 10, 20, and 100 μA (scale bar = 1000 pA, 60 ms). (**K**) Evoked IPSCs are decreased in *Ube3a*$^{STOP/p+}$ mice compared to controls, but *Ube3a*$^{STOP/p+}$::*Gad2-Cre* mice are not different from controls or *Ube3a*$^{STOP/p+}$ mice (control n=21 cells; *Ube3a*$^{STOP/p+}$ n=24 cells; *Ube3a*$^{STOP/p+}$::*Gad2-Cre* n=29 cells). (**L**) Sample recordings showing baseline (top), high frequency depletion (middle), and recovery (bottom) phases (scale bars; baseline = 200 pA, 20 ms; depletion = 200 pA, 70 ms; recovery = 200 pA, 20 ms). (**M**) Average depletion phase showing eIPSC amplitude normalized to baseline during 800 stimuli at 30 Hz. 10 responses are averaged for each point (control n=9 cells; *Ube3a*$^{STOP/p+}$ n=13 cells; *Ube3a*$^{STOP/p+}$::*Gad2-Cre* n=11 cells). (**N**) Average recovery phase showing eIPSC

amplitude normalized to baseline during 90 stimuli at 0.33 Hz. 3 responses are averaged for each point (control n=9 cells; *Ube3a*$^{STOP/p+}$ n=13 cells; *Ube3a*$^{STOP/p+}$::*Gad2-Cre* n=11 cells). All data are represented as the mean ± SEM (*p<0.05; **p<.01).

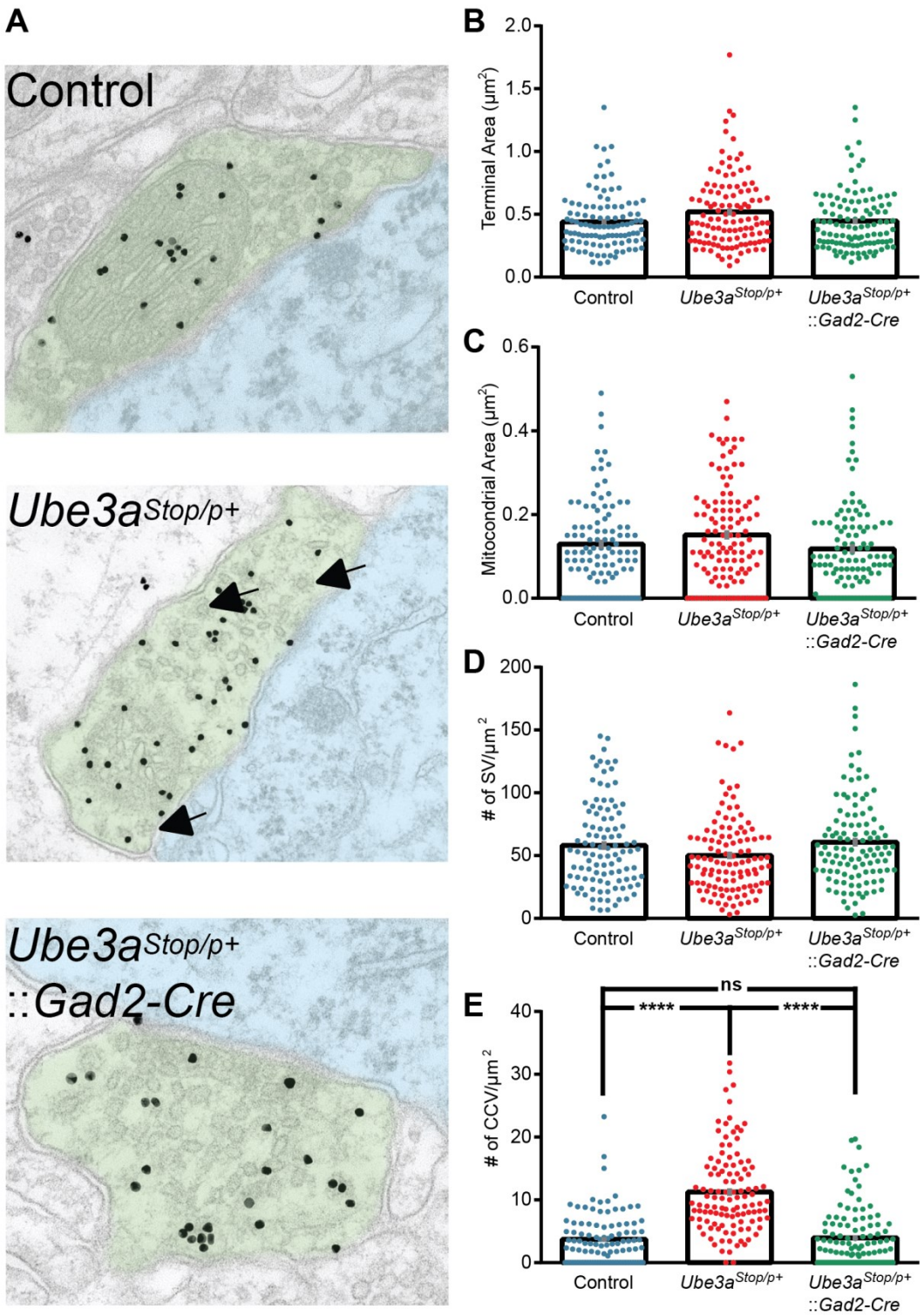

Figure 3.6 Accumulation of CCVs in *Ube3a*$^{STOP/p+}$ mice at inhibitory synapses onto somata are eliminated by reinstatement of Ube3a in inhibitory interneurons.

(**A**) Electron micrographs of inhibitory synapses stained for GABA in control, *Ube3a*$^{STOP/p+}$, and *Ube3a*$^{STOP/p+}$::*GAD2-Cre* mice (green denotes axon terminal, blue denotes soma, arrows indicate CCVs). Average values of (top to bottom) (**B**) axon terminal area, (**C**) mitochondrial area, (**D**) number of synaptic vesicles (SV) per square micron, and (**E**) number of CCVs per square micron (****p<0.0001, n = 3 animals per genotype).

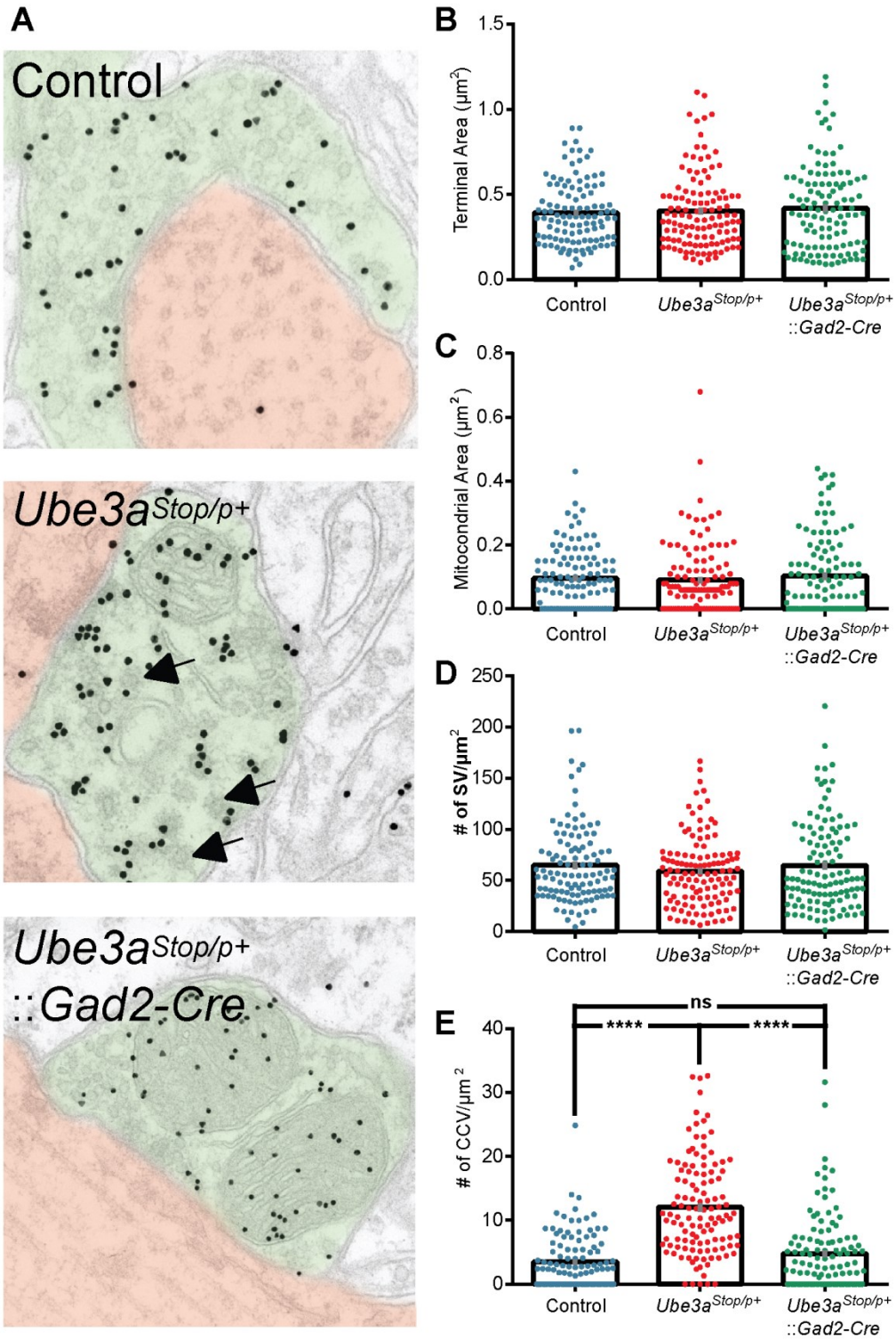

Figure 3.7 Accumulation of CCVs in *Ube3a*$^{STOP/p+}$ mice at inhibitory synapses onto dendrites are eliminated by reinstatement of *Ube3a* in inhibitory interneurons.

(**A**) Electron micrographs of inhibitory synapses stained for GABA in control, *Ube3a*$^{STOP/p+}$, and *Ube3a*$^{STOP/p+}$::*GAD2-Cre* mice (green denotes axon terminal, red denotes dendrite, arrows indicate CCVs). Average values of (top to bottom) (**B**) axon terminal area, (**C**) mitochondrial area, (**D**) number of synaptic vesicles (SV) per square micron, and (**E**) number of CCVs per square micron (****p<0.0001, n = 3 animals per genotype).

CHAPTER 4: DISCUSSION

4.1 Molecular mechanisms underlying synaptic defects in AS model mice

Ube3a is an E3 ubiquitin ligase and its primary function is to transfer polyubiquitin chains to substrate proteins targeting them for proteasomal degradation. Therefore, it has been hypothesized that AS results from the accumulation of Ube3a substrate proteins which in turn cause cellular/circuit dysfunction and behavioral abnormalities. However, identifying molecular targets for Ube3a in neurons has been one of the greatest challenges to AS research. Only recently have targets for Ube3a been identified that have a direct link to synaptic transmission. Notably, Arc and Ephexin5, which possibly contribute to defects in excitatory neurotransmission and plasticity, were recently identified as Ube3a substrates (Greer et al., 2010; Margolis et al., 2010).

Activity-regulated cytoskeleton-associated protein (Arc) is involved in regulation of excitatory synaptic strength through its actions during activity regulated AMPA receptor endocytosis (Chowdhury et al., 2006). In *Ube3a*$^{m-/p+}$ mice, Arc protein levels are increased and it has been shown that Ube3a interacts with a fragment of the Arc C-terminus in vitro. Therefore, it has been hypothesized that Arc is a substrate that Ube3a targets for degradation and accumulates in the absence of Ube3a resulting in excessive AMPA receptor endocytosis and excitatory synapse loss ((Greer et al., 2010), but also see (Kuhnle et al., 2013)). However, Arc is also strongly regulated by neuronal activity levels and could be expressed at increased levels in the seizure prone *Ube3a*$^{m-/p+}$ mice

(Lyford et al., 1995). Furthermore, Arc levels have been shown to be increased in other mouse models of autism spectrum disorders as a byproduct of increased neuronal activity levels rather than a direct consequence of gene loss (Bateup et al., 2013). If Arc is in fact a true substrate of Ube3a than mosaic deletion of *Ube3a* may result in cell autonomous loss of excitatory synapses, a hypothesis that will be tested in the future. Despite the advances made in understanding the molecular underpinnings of excitatory synaptic defects in *Ube3a*$^{m-/p+}$ mice, no study has uncovered any potential Ube3a substrates involved in inhibitory synaptic function.

The molecular architecture involved in synaptic vesicle recycling has been studied extensively and has revealed a detailed interplay between large numbers of presynaptic proteins (Slepnev and De Camilli, 2000; Sudhof, 2004). Therefore, when we observed an increase in CCVs in the presynaptic terminals of inhibitory synapses in *Ube3a*$^{m-/p+}$ mice we were able to quickly identify key molecules known to be involved in clathrin-coated vesicle formation and uncoating. Synaptojanin 1 was identified as a molecule necessary for the uncoating of CCVs. Its phosphoinositide phosphatase activity initiates disassembly of the clathrin coat, and it has also been shown to be involved in the early stages of CCV endocytosis (Cremona et al., 1999; Mani et al., 2007). Interestingly, inhibitory axon terminals seem to be particularly sensitive to insults to synaptic vesicle cycling machinery perhaps due to their high probability of release, low synaptic vesicle number, and/or high activity rates (Hayashi et al., 2008; Luthi et al., 2001). Neurons and mice lacking synaptojanin 1 accumulate large numbers of CCVs, especially at inhibitory synapses, and have defects in recovery of neurotransmission following high frequency stimulation (Cremona et al., 1999; Hayashi et al., 2008).

Similar to synaptojanin 1 KOs, *Ube3a*$^{m-/p+}$ mice have no detectable defects in baseline synaptic release probability; however, following periods of high activity GABA release is reduced (**Fig. 2.7C$_3$**). Reduced GABA release following high levels of activity is likely due to defective replenishment of release competent synaptic vesicles subsequent to deficient synaptic vesicle recycling (Kim et al., 2002).

Other proteins involved in synaptic vesicle cycling have been shown to directly associate with synaptojanin 1, these include endophillin, Eps15, syndapin and amphiphysin (Di Paolo et al., 2002; Koh et al., 2007; Milosevic et al., 2011; Qualmann et al., 1999). Of this group, endophillin was recently shown to be required for uncoating of CCVs, and endophillin KO neurons have a similar electrophysiological signature as both synaptojanin 1 KOs and *Ube3a*$^{m-/p+}$ mice (Milosevic et al., 2011). While these mice show similar phenotypes to *Ube3a*$^{m-/p+}$ mice, it is unlikely that Ube3a directly targets any of these proteins for degradation because deletion, not overexpression, of these molecules leads to phenotypes similar to *Ube3a*$^{m-/p+}$ mice. It is more likely that Ube3a targets a negative regulator of a protein required for CCV uncoating or alternatively activates a protein required for CCV uncoating, resulting in CCV accumulation in the absence of Ube3a.

Monoubiquitination is also performed by E3 ubiquitin ligases such as Ube3a and is a reversible non-proteolytic modification and that controls protein function (Haglund and Dikic, 2005). Interestingly, monoubiquitination of endocytic proteins Eps15 and Epsin is important for their functional roles and interactions with other endocytic/CCV associated proteins (Chen et al., 1998; Koh et al., 2007; Polo et al., 2002). In fact, a small 40 aa protein domain is required for their monoubiquitination and is present on

several other proteins involved in membrane trafficking at the axon terminal (Polo et al., 2002). Therefore, proteins involved in synaptic vesicle cycling/membrane trafficking may be particularly vulnerable to defects in monoubiquitination resulting from Ube3a loss. Additionally, there has recently been evidence that Ube3a has a role in the golgi apparatus and membrane trafficking further implicating vesicle and membrane trafficking in AS pathology (Condon et al., 2013).

Collectively, there is strong evidence that inhibitory synapses in *Ube3a*$^{m-/p+}$ mice have vesicle cycling and/or CCV uncoating defects. Furthermore, several proteins involved in clathrin-coated vesicle endocytosis and uncoating are targets for ubiquitination and, when deleted, lead to synaptic phenotypes similar to those observed in *Ube3a*$^{m-/p+}$ mice. Future biochemical and proteomic studies examining levels of CCV associated proteins, and their ubiquitination status, at inhibitory axon terminals in *Ube3a*$^{m-/p+}$ mice will yield important insights into new substrates for Ube3a.

4.2 $GABA_A$ receptor contributions to inhibitory defects in AS model mice

$GABA_A$ receptors (GABARs) have long been hypothesized to be involved in AS pathogenesis due to the proximity of *UBE3A* to a cluster of GABAR subunit genes (β3, α5, and γ3) on chromosome 15 (Dan and Boyd, 2003). Therefore it was predicted that haploinsufficency of a GABARs in large deletion patients may contribute to certain AS symptoms. This hypothesis has received less attention in studies on the AS mouse model as the targeted mutation is in the *Ube3a* gene alone and does not disrupt genes coding for GABAR subunits. However, there are reports of reduced GABAR subunit α5 mRNA levels in the cerebellum of *Ube3a*$^{m-/p+}$ mice indicating reduced Ube3a levels may

affect select GABAR subunits (Low and Chen, 2010). Nevertheless, to date, no study has revealed decreased GABA receptor protein levels in AS model mice.

Our studies performed in the *Ube3a*$^{m-/p+}$ mice led us to believe that defects in GABAergic neurotransmission were primarily presynaptic, arising from defects in synaptic vesicle cycling. Furthermore we observed no change in mIPSC amplitude indicating that activation of synaptic GABARs was unchanged in *Ube3a*$^{m-/p+}$ mice (**Fig. 2.1**). Therefore, we were surprised to see decreased evoked IPSC amplitude in the *Ube3a*$^{Flox/p+}$::*NEX*-Cre mice where *Ube3a* was deleted in the postsynaptic pyramidal neuron but not the presynaptic GABAergic neurons (**Fig. 3.3K**). This finding made us reconsider the possibility that there were both pre and postsynaptic contributions to GABAergic neurotransmission defects in *Ube3a*$^{m-/p+}$ mice.

mIPSC amplitude remains unchanged in *Ube3a*$^{Flox/p+}$::*NEX*-Cre mice, therefore it is likely that a reduction in extrasynaptic GABARs are contributing to decreased evoked IPSC amplitude which are activated during high stimulation intensities (Brickley and Mody, 2012). Extrasynaptic, primarily δ-subunit containing, GABARs have a high affinity for GABA and are tonically activated by the low concentrations of ambient GABA present in the extracellular space (Farrant and Nusser, 2005). Recent studies examining cerebellar granule neurons observed decreased tonic GABA current in *Ube3a*$^{m-/p+}$ mice due to decreased extracellular GABA concentrations. GABA concentrations were decreased due to increased expression of the GABA transporter GAT1 in *Ube3a*$^{m-/p+}$ mice (Egawa et al., 2012). It is likely that alterations in extrasynaptic GABARs also occur in L2/3 pyramidal neurons of *Ube3a*$^{m-/p+}$ mice; however, it is unlikely that changes in tonic GABA current would be due to changes in

GAT1 expression in the *Ube3a*$^{Flox/p+}$::*NEX*-Cre mice as Ube3a levels are normal in GABAergic neurons and astrocytes that predominantly express GAT1 (Melone et al., 2013; Minelli et al., 1995). Furthermore, changes in extrasynaptic GABARs may have different effects in L2/3 pyramidal neurons than in cerebellar granule neurons as they can be partially activated by synaptic GABA release (Ye et al., 2013). Studies examining extrasynaptic GABARs including investigation of the tonic GABAR current will help to determine the precise contribution of extrasynaptic GABARs to defects in inhibitory neurotransmission in *Ube3a*$^{m-/p+}$ mice. Finally, it will also be important to determine if loss of Ube3a in the postsynaptic pyramidal neuron alone is sufficient to cell-autonomously decrease evoked IPSC amplitude in L2/3 pyramidal neurons. This can be achieved with mosaic expression of Cre in the *Ube3a*$^{Flox/p+}$ mouse line (Agarwal et al., 2012; Chakrabarty et al., 2013). Once cell autonomous phenotypes are identified, understanding the molecular and biochemical means by which they result from Ube3a loss will allow a more complete picture of Ube3a function in specific neuron types and circuits.

4.3 E/I imbalance and seizure susceptibility in AS

Individuals with Angelman syndrome have increased seizure susceptibility and often develop epilepsy (Thibert et al., 2009). Epilepsy in AS patients is notoriously difficult to control with treatments often differing largely from patient to patient, and even changing drastically within a patient over time (Thibert et al., 2013). AS patients also present with a characteristic electroencephalogram (EEG) signature consisting of notched delta (1-3.5 Hz) and rhythmic theta (4-7.5 Hz) activity interspersed with epileptiform discharges (Thibert et al., 2009). Therefore, while seizure genesis may not

lie within cortical circuits, they clearly participate and permit seizure activity and abnormal cortical oscillations in AS individuals.

A major impetus for initiating our studies on E/I balance in *Ube3a*$^{m-/p+}$ mice were reports regarding their high susceptibility to seizures (Jiang et al., 1998). Seizures in *Ube3a*$^{m-/p+}$ mice are triggered by strong auditory stimuli such as vigorous key grating on a metal cage top, or loud (120 dB) personal alarm systems (Jiang et al., 1998; Osterweil et al., 2013). These audiogenic seizures are dependent on mouse strain and are present on the 129Sv/Ev or 129Sv/Pas strain, but not the C57BL/6J strain ((Jiang et al., 1998), unpublished observations). Audiogenic seizures are a model of generalized seizure that involves predominantly midbrain auditory circuits such as the inferior colliculus and reticular formation, but also recruit cortical and limbic circuits following kindling (Ross and Coleman, 2000; Simler et al., 1994). It is difficult to speculate on how cortical E/I imbalance may relate or contribute to audiogenic seizure susceptibility in *Ube3a*$^{m-/p+}$ mice; however, clearly hyperexcitable circuits do exist in *Ube3a*$^{m-/p+}$ mice and cortical circuits are positioned to propagate epileptic activity throughout the brain.

In support of cortical participation in epileptic activity, AS model mice exhibit abnormal cortical EEG/ECoG patterns on both 129 and C57 mouse strains (Jiang et al., 1998; Miura et al., 2002). Furthermore, detailed power spectral analysis of cortical network activity using local field potential (LFP) recordings made from primary visual cortex of *Ube3a*$^{m-/p+}$ mice revealed increased power in the delta and theta frequency bands compared to controls (Riday, 2013). This suggests that aberrant LFP activity in *Ube3a*$^{m-/p+}$ mice may mirror altered EEG activity occurring the same frequency bands in AS individuals. Recent optogenetic studies examining cellular determinants of cortical

oscillations have demonstrated that increased power in the low frequency delta and theta bands likely arises from increased synchrony of cortical pyramidal neurons (Cardin et al., 2009; Vierling-Claassen et al., 2010). These observations suggest that increased pyramidal neuron activity may underlie increased delta and theta power in cortical networks of *Ube3a*$^{m-/p+}$ mice. It will be interesting to examine cortical oscillations in conditional *Ube3a* animals to test for neuron type-specific contributions to abnormal cortical rhythms.

While generalized tonic-clonic seizures are the most dangerous type of epileptic activity to occur in AS individuals, absence or drop seizures are just as common (Thibert et al., 2009). Absence seizures may arise from disruptions in the thalamocortical circuit and are detected with EEG as sudden generalized synchronous spike-wave discharges of 2-4 Hz (Genton et al., 2008; Huguenard and McCormick, 2007). Absence seizures behaviorally manifest as a loss of cognitive abilities and behavioral arrest (Browne et al., 1974).

Ube3a$^{m-/p+}$ mice also exhibit spontaneous spike wave discharges that occur with behavioral immobility and abnormal posturing (Colas et al., 2005). It is likely that the increased delta and theta power observed in the visual cortex LFP results, at least in part, from these spike-wave discharges which may indicate occurrence of absence seizures in the AS model mouse. Spike-wave discharges arise following bursting activity of thalamocortical relay neurons which synapse onto layer 4 excitatory neurons resulting in high frequency synchronous activity in cortical layers 4 and 2/3 (McCormick and Contreras, 2001). This activity is detected by the EEG electrodes as a large spike that repeatedly occurs at 2-4 Hz during an absence seizure (Genton et al., 2008).

The presence of abnormal slow-wave sleep in AS model mice also points towards defective thalamocortical circuitry (Colas et al., 2005). "Sleep spindles" or rhythmic thalamocortical bursting events during slow-wave (non-REM) sleep, require thalamocortical and GABAergic thalamic reticular circuitry and may underlie abnormal sleep in AS mice (Bruni et al., 2004; Colas et al., 2005; Halassa et al., 2011). Together, physiological and behavioral measures in AS model mice present a convincing case for the occurrence of absence, thalamocortically derived, seizure activity. It is possible that this activity may arise from defective thalamic, cortical, or thalamocortical circuits. E/I imbalance in cortical circuits could certainly magnify and propagate seizure activity initiated in the thalamus, and it is likely that all three circuits have some role in seizure activity. Obviously, experiments directed at monitoring thalamocortical networks and behavioral state simultaneously are needed before one can make strong conclusions concerning absence seizures, and their underlying circuits, in AS mice.

4.4 Rescue/prevention of AS phenotypes via expression of *Ube3a* in GABAergic neurons

A provocative finding arising for our studies examining *Ube3a*$^{STOP/p+}$ mice were that reinstating *Ube3a* expression in GABAergic neurons in early development prevented defects in synaptic vesicle cycling at inhibitory synapses (**Fig 3.5-7**). These data suggest that reinstating Ube3a in a small subpopulation of neurons may be sufficient for significant recovery of circuit function in AS model mice. Of course, the *GAD2-Cre* line expresses Cre in GABAergic neurons throughout the brain, including cortex, striatum, thalamic reticular nucleus, hippocampus, etc., all which may contribute to the prevention of synaptic vesicle cycling defects in the cortex of *Ube3a*$^{STOP/p+}$

::GAD2-Cre mice (Taniguchi et al., 2011). Important future experiments will investigate recovery of behavioral defects including seizure susceptibility and motor performance following reinstatement of *Ube3a* in GABAergic neurons. These experiments will also help define behaviors that may be relevant to the anatomical and electrophysiological defects we observed in the visual cortex. Also, crossing the *Ube3a*$^{STOP/p+}$ line to Cre lines targeting subsets of GABAergic neurons in specific brain areas (ie cortical, thalamic, etc.) will allow further identification of the particular GABAergic circuits that are required for rescue of synaptic defects and associated behaviors.

Recent studies have shown that the small molecule inhibitors of topoisomerase are capable of unsilencing paternal *Ube3a* in AS mice (Huang et al., 2012). A remaining challenge is to determine the therapeutic window for treatments based on reinstating *Ube3a* expression. A major advantage of the *Ube3a*$^{STOP/p+}$ line is that *Ube3a* expression of *Ube3a* can be controlled in a temporally precise and dose dependent manner when combined with tamoxifen inducible Cre lines (Hayashi and McMahon, 2002). Therefore, to define the most efficacious window(s) for therapeutic intervention, one could employ a GABAergic neuron specific inducible Cre line and inject tamoxifen at specific points in development, then electrophysiologically and behaviorally assay for recovery of AS phenotypes.

Identifying optimal windows for therapeutic intervention as well as the neuron type or types most likely to yield significant behavioral improvement are crucial future studies that will be of large interest in the AS field. Importantly, many of those future experiments rely and build on the work presented here.

4.5 Effects of E/I imbalance on cortical computation

Synaptic deficits observed in *Ube3a*$^{m-/p+}$ mice result in cortical E/I imbalance; however, it remains unclear how E/I imbalance would affect neuronal computations performed in cortex. Several studies have recently examined the effects of modulating inhibition on information transfer within the cortical neural network (Sohal et al., 2009; Yizhar et al., 2011). These studies and others suggest that timing and synchronization within and between neural networks is controlled by inhibition and is crucial for efficient information processing and transfer (Buzsaki and Watson, 2012). E/I imbalance in *Ube3a*$^{m-/p+}$ mice likely interferes with optimal information processing in cortical networks as evidenced by altered cortical synchrony and cognitive defects (Huang et al., 2013; Riday, 2013).

A cortical region that allows direct testing for defects in cortical computations is the visual cortex, which traditionally has been a focus of many computational neuroscientists studying vision and provides a rich literature describing various circuit computations (Marr, 1980; Priebe and Ferster, 2012). Recently, optogenetic modulation of inhibition in visual cortex has shown that cortical computations underlying orientation tuning and contrast sensitivity can be modified by increasing or decreasing activity of entire subpopulations of inhibitory neurons (Atallah et al., 2012; Cottam et al., 2013; Lee et al., 2012; Wilson et al., 2012). By extension, E/I imbalance may be expected to affect orientation tuning and contrast sensitivity in visual cortex *Ube3a*$^{m-/p+}$ mice. Alternatively, defects in inhibition in *Ube3a*$^{m-/p+}$ mice are quite distinct from optogenetic modulation of inhibitory neuron subpopulations and may be expected to have different effects. For example, due to synaptic vesicle cycling defects, deficits in inhibition may be particularly

severe in *Ube3a*$^{m-/p+}$ mice following high levels of inhibitory neuron activity, but very mild during quiescent states. Therefore, cortical computations may only be measurably altered in *Ube3a*$^{m-/p+}$ mice following some sort of priming paradigm that would deplete GABAergic transmission or a behavioral state or task that heavily activates inhibitory neurons. Increased cortical activity states are observed during periods of heightened awareness or attention and therefore may be preferentially affected in *Ube3a*$^{m-/p+}$ mice (Pinto et al., 2013). Furthermore, particular inputs into cortex activate specific types of inhibitory neurons and computations performed by these networks may be particularly impaired in AS mice (Lee et al., 2013; Pi et al., 2013). Experiments addressing cortical computations in the visual cortex *in vivo* in awake animals would be the best way to test for defects in information processing in cortical circuits in *Ube3a*$^{m-/p+}$ mice as well as other mouse models of neurodevelopmental disorders. With the advent of advanced imaging and optogenetics combined with mouse models with conditional control of gene expression, new insights into neurological disorders and their underlying defects in neural information processing will emerge.

REFERENCES

Agarwal, A., Dibaj, P., Kassmann, C.M., Goebbels, S., Nave, K.A., and Schwab, M.H. (2012). In vivo imaging and noninvasive ablation of pyramidal neurons in adult NEX-CreERT2 mice. Cereb Cortex *22*, 1473-1486.

Albrecht, U., Sutcliffe, J.S., Cattanach, B.M., Beechey, C.V., Armstrong, D., Eichele, G., and Beaudet, A.L. (1997). Imprinted expression of the murine Angelman syndrome gene, Ube3a, in hippocampal and Purkinje neurons. Nat Genet *17*, 75-78.

American Psychiatric Association, A. (2013). Diagnostic and statistical manual of mental disorders 5th edn (Arlington, VA: American Psychiatric Publishing.).

Amir, R.E., Van den Veyver, I.B., Wan, M., Tran, C.Q., Francke, U., and Zoghbi, H.Y. (1999). Rett syndrome is caused by mutations in X-linked MECP2, encoding methyl-CpG-binding protein 2. Nat Genet *23*, 185-188.

Atallah, B.V., Bruns, W., Carandini, M., and Scanziani, M. (2012). Parvalbumin-expressing interneurons linearly transform cortical responses to visual stimuli. Neuron *73*, 159-170.

Atwood, H.L., and Karunanithi, S. (2002). Diversification of synaptic strength: presynaptic elements. Nat Rev Neurosci *3*, 497-516.

Bakker, C.E., Verheij, C., Willemsen, R., van der Helm, R., Oerlemans, F., Vermey, M., Bygrave, A., Bygrave, A., Hoogeveen, A.T., and Oostra, B.A. (1994). Fmr1 knockout mice: a model to study fragile X mental retardation. The Dutch-Belgian Fragile X Consortium. Cell *78*, 23-33.

Bassell, G.J., and Warren, S.T. (2008). Fragile X syndrome: loss of local mRNA regulation alters synaptic development and function. Neuron *60*, 201-214.

Bateup, H.S., Johnson, C.A., Denefrio, C.L., Saulnier, J.L., Kornacker, K., and Sabatini, B.L. (2013). Excitatory/inhibitory synaptic imbalance leads to hippocampal hyperexcitability in mouse models of tuberous sclerosis. Neuron *78*, 510-522.

Brickley, S.G., and Mody, I. (2012). Extrasynaptic GABA(A) receptors: their function in the CNS and implications for disease. Neuron *73*, 23-34.

Browne, T.R., Penry, J.K., Proter, R.J., and Dreifuss, F.E. (1974). Responsiveness before, during, and after spike-wave paroxysms. Neurology *24*, 659-665.

Bruni, O., Ferri, R., D'Agostino, G., Miano, S., Roccella, M., and Elia, M. (2004). Sleep disturbances in Angelman syndrome: a questionnaire study. Brain & development *26*, 233-240.

Bureau, I., Shepherd, G.M., and Svoboda, K. (2008). Circuit and plasticity defects in the developing somatosensory cortex of FMR1 knock-out mice. J Neurosci *28*, 5178-5188.

Buzsaki, G., Anastassiou, C.A., and Koch, C. (2012). The origin of extracellular fields and currents--EEG, ECoG, LFP and spikes. Nat Rev Neurosci *13*, 407-420.

Buzsaki, G., and Watson, B.O. (2012). Brain rhythms and neural syntax: implications for efficient coding of cognitive content and neuropsychiatric disease. Dialogues in clinical neuroscience *14*, 345-367.

Cardin, J.A., Carlen, M., Meletis, K., Knoblich, U., Zhang, F., Deisseroth, K., Tsai, L.H., and Moore, C.I. (2009). Driving fast-spiking cells induces gamma rhythm and controls sensory responses. Nature *459*, 663-667.

Chahrour, M., and Zoghbi, H.Y. (2007). The story of Rett syndrome: from clinic to neurobiology. Neuron *56*, 422-437.

Chakrabarty, P., Rosario, A., Cruz, P., Siemienski, Z., Ceballos-Diaz, C., Crosby, K., Jansen, K., Borchelt, D.R., Kim, J.Y., Jankowsky, J.L.*, et al.* (2013). Capsid serotype and timing of injection determines AAV transduction in the neonatal mice brain. PLoS One *8*, e67680.

Chao, H.T., Chen, H., Samaco, R.C., Xue, M., Chahrour, M., Yoo, J., Neul, J.L., Gong, S., Lu, H.C., Heintz, N.*, et al.* (2010). Dysfunction in GABA signalling mediates autism-like stereotypies and Rett syndrome phenotypes. Nature *468*, 263-269.

Chattopadhyaya, B., Di Cristo, G., Higashiyama, H., Knott, G.W., Kuhlman, S.J., Welker, E., and Huang, Z.J. (2004). Experience and activity-dependent maturation of perisomatic GABAergic innervation in primary visual cortex during a postnatal critical period. J Neurosci *24*, 9598-9611.

Chaudhry, F.A., Reimer, R.J., Bellocchio, E.E., Danbolt, N.C., Osen, K.K., Edwards, R.H., and Storm-Mathisen, J. (1998). The vesicular GABA transporter, VGAT, localizes to synaptic vesicles in sets of glycinergic as well as GABAergic neurons. J Neurosci *18*, 9733-9750.

Chen, H., Fre, S., Slepnev, V.I., Capua, M.R., Takei, K., Butler, M.H., Di Fiore, P.P., and De Camilli, P. (1998). Epsin is an EH-domain-binding protein implicated in clathrin-mediated endocytosis. Nature *394*, 793-797.

Chen, R.Z., Akbarian, S., Tudor, M., and Jaenisch, R. (2001). Deficiency of methyl-CpG binding protein-2 in CNS neurons results in a Rett-like phenotype in mice. Nat Genet *27*, 327-331.

Chowdhury, S., Shepherd, J.D., Okuno, H., Lyford, G., Petralia, R.S., Plath, N., Kuhl, D., Huganir, R.L., and Worley, P.F. (2006). Arc/Arg3.1 interacts with the endocytic machinery to regulate AMPA receptor trafficking. Neuron *52*, 445-459.

Colas, D., Wagstaff, J., Fort, P., Salvert, D., and Sarda, N. (2005). Sleep disturbances in Ube3a maternal-deficient mice modeling Angelman syndrome. Neurobiol Dis *20*, 471-478.

Comery, T.A., Harris, J.B., Willems, P.J., Oostra, B.A., Irwin, S.A., Weiler, I.J., and Greenough, W.T. (1997). Abnormal dendritic spines in fragile X knockout mice: maturation and pruning deficits. Proc Natl Acad Sci U S A *94*, 5401-5404.

Condon, K.H., Ho, J., Robinson, C.G., Hanus, C., and Ehlers, M.D. (2013). The Angelman syndrome protein Ube3a/E6AP is required for Golgi acidification and surface protein sialylation. J Neurosci *33*, 3799-3814.

Cossart, R., Dinocourt, C., Hirsch, J.C., Merchan-Perez, A., De Felipe, J., Ben-Ari, Y., Esclapez, M., and Bernard, C. (2001). Dendritic but not somatic GABAergic inhibition is decreased in experimental epilepsy. Nat Neurosci *4*, 52-62.

Cottam, J.C., Smith, S.L., and Hausser, M. (2013). Target-specific effects of somatostatin-expressing interneurons on neocortical visual processing. J Neurosci *33*, 19567-19578.

Cremona, O., Di Paolo, G., Wenk, M.R., Luthi, A., Kim, W.T., Takei, K., Daniell, L., Nemoto, Y., Shears, S.B., Flavell, R.A.*, et al.* (1999). Essential role of phosphoinositide metabolism in synaptic vesicle recycling. Cell *99*, 179-188.

Dan, B., and Boyd, S.G. (2003). Angelman syndrome reviewed from a neurophysiological perspective. The UBE3A-GABRB3 hypothesis. Neuropediatrics *34*, 169-176.

Dani, V.S., Chang, Q., Maffei, A., Turrigiano, G.G., Jaenisch, R., and Nelson, S.B. (2005). Reduced cortical activity due to a shift in the balance between excitation and inhibition in a mouse model of Rett syndrome. Proc Natl Acad Sci U S A *102*, 12560-12565.

Dani, V.S., and Nelson, S.B. (2009). Intact long-term potentiation but reduced connectivity between neocortical layer 5 pyramidal neurons in a mouse model of Rett syndrome. J Neurosci *29*, 11263-11270.

Di Cristo, G., Wu, C., Chattopadhyaya, B., Ango, F., Knott, G., Welker, E., Svoboda, K., and Huang, Z.J. (2004). Subcellular domain-restricted GABAergic innervation in primary visual cortex in the absence of sensory and thalamic inputs. Nat Neurosci *7*, 1184-1186.

Di Paolo, G., Sankaranarayanan, S., Wenk, M.R., Daniell, L., Perucco, E., Caldarone, B.J., Flavell, R., Picciotto, M.R., Ryan, T.A., Cremona, O*., et al.* (2002). Decreased synaptic vesicle recycling efficiency and cognitive deficits in amphiphysin 1 knockout mice. Neuron *33*, 789-804.

Dichter, G.S. (2012). Functional magnetic resonance imaging of autism spectrum disorders. Dialogues in clinical neuroscience *14*, 319-351.

Dindot, S.V., Antalffy, B.A., Bhattacharjee, M.B., and Beaudet, A.L. (2008). The Angelman syndrome ubiquitin ligase localizes to the synapse and nucleus, and maternal deficiency results in abnormal dendritic spine morphology. Hum Mol Genet *17*, 111-118.

Durand, S., Patrizi, A., Quast, K.B., Hachigian, L., Pavlyuk, R., Saxena, A., Carninci, P., Hensch, T.K., and Fagiolini, M. (2012). NMDA receptor regulation prevents regression of visual cortical function in the absence of Mecp2. Neuron *76*, 1078-1090.

Eagleson, K.L., Bonnin, A., and Levitt, P. (2005). Region- and age-specific deficits in gamma-aminobutyric acidergic neuron development in the telencephalon of the uPAR(-/-) mouse. J Comp Neurol *489*, 449-466.

Egawa, K., Kitagawa, K., Inoue, K., Takayama, M., Takayama, C., Saitoh, S., Kishino, T., Kitagawa, M., and Fukuda, A. (2012). Decreased tonic inhibition in cerebellar

granule cells causes motor dysfunction in a mouse model of Angelman syndrome. Science translational medicine *4*, 163ra157.

Farrant, M., and Nusser, Z. (2005). Variations on an inhibitory theme: phasic and tonic activation of GABA(A) receptors. Nat Rev Neurosci *6*, 215-229.

Fukuda, T., Itoh, M., Ichikawa, T., Washiyama, K., and Goto, Y. (2005). Delayed maturation of neuronal architecture and synaptogenesis in cerebral cortex of Mecp2-deficient mice. Journal of neuropathology and experimental neurology *64*, 537-544.

Genton, P., Ferlazzo, E., and Thomas, P. (2008). Absence status epilepsy: delineation of a distinct idiopathic generalized epilepsy syndrome. Epilepsia *49*, 642-649.

Gibson, J.R., Bartley, A.F., Hays, S.A., and Huber, K.M. (2008). Imbalance of neocortical excitation and inhibition and altered UP states reflect network hyperexcitability in the mouse model of fragile X syndrome. J Neurophysiol *100*, 2615-2626.

Goebbels, S., Bormuth, I., Bode, U., Hermanson, O., Schwab, M.H., and Nave, K.A. (2006). Genetic targeting of principal neurons in neocortex and hippocampus of NEX-Cre mice. Genesis (New York, NY : 2000) *44*, 611-621.

Goncalves, J.T., Anstey, J.E., Golshani, P., and Portera-Cailliau, C. (2013). Circuit level defects in the developing neocortex of Fragile X mice. Nat Neurosci *16*, 903-909.

Gonchar, Y., Wang, Q., and Burkhalter, A. (2007). Multiple distinct subtypes of GABAergic neurons in mouse visual cortex identified by triple immunostaining. Front Neuroanat *1*, 3.

Graus-Porta, D., Blaess, S., Senften, M., Littlewood-Evans, A., Damsky, C., Huang, Z., Orban, P., Klein, R., Schittny, J.C., and Muller, U. (2001). Beta1-class integrins regulate the development of laminae and folia in the cerebral and cerebellar cortex. Neuron *31*, 367-379.

Greer, P.L., Hanayama, R., Bloodgood, B.L., Mardinly, A.R., Lipton, D.M., Flavell, S.W., Kim, T.K., Griffith, E.C., Waldon, Z., Maehr, R.*, et al.* (2010). The Angelman Syndrome protein Ube3A regulates synapse development by ubiquitinating arc. Cell *140*, 704-716.

Guo, Z.V., Li, N., Huber, D., Ophir, E., Gutnisky, D., Ting, J.T., Feng, G., and Svoboda, K. (2014). Flow of cortical activity underlying a tactile decision in mice. Neuron *81*, 179-194.

Gupta, A., Wang, Y., and Markram, H. (2000). Organizing principles for a diversity of GABAergic interneurons and synapses in the neocortex. Science *287*, 273-278.

Hagerman, R.J., Berry-Kravis, E., Kaufmann, W.E., Ono, M.Y., Tartaglia, N., Lachiewicz, A., Kronk, R., Delahunty, C., Hessl, D., Visootsak, J.*, et al.* (2009). Advances in the treatment of fragile X syndrome. Pediatrics *123*, 378-390.

Haglund, K., and Dikic, I. (2005). Ubiquitylation and cell signaling. The EMBO journal *24*, 3353-3359.

Halassa, M.M., Siegle, J.H., Ritt, J.T., Ting, J.T., Feng, G., and Moore, C.I. (2011). Selective optical drive of thalamic reticular nucleus generates thalamic bursts and cortical spindles. Nat Neurosci *14*, 1118-1120.

Hayashi, M., Raimondi, A., O'Toole, E., Paradise, S., Collesi, C., Cremona, O., Ferguson, S.M., and De Camilli, P. (2008). Cell- and stimulus-dependent heterogeneity of synaptic vesicle endocytic recycling mechanisms revealed by studies of dynamin 1-null neurons. Proc Natl Acad Sci U S A *105*, 2175-2180.

Hayashi, S., and McMahon, A.P. (2002). Efficient recombination in diverse tissues by a tamoxifen-inducible form of Cre: a tool for temporally regulated gene activation/inactivation in the mouse. Developmental biology *244*, 305-318.

Hays, S.A., Huber, K.M., and Gibson, J.R. (2011). Altered neocortical rhythmic activity states in Fmr1 KO mice are due to enhanced mGluR5 signaling and involve changes in excitatory circuitry. J Neurosci *31*, 14223-14234.

Hensch, T.K. (2005). Critical period plasticity in local cortical circuits. Nat Rev Neurosci *6*, 877-888.

Hensch, T.K., Fagiolini, M., Mataga, N., Stryker, M.P., Baekkeskov, S., and Kash, S.F. (1998). Local GABA circuit control of experience-dependent plasticity in developing visual cortex. Science *282*, 1504-1508.

Huang, H.S., Allen, J.A., Mabb, A.M., King, I.F., Miriyala, J., Taylor-Blake, B., Sciaky, N., Dutton, J.W., Jr., Lee, H.M., Chen, X.*, et al.* (2012). Topoisomerase inhibitors unsilence the dormant allele of Ube3a in neurons. Nature *481*, 185-189.

Huang, H.S., Burns, A.J., Nonneman, R.J., Baker, L.K., Riddick, N.V., Nikolova, V.D., Riday, T.T., Yashiro, K., Philpot, B.D., and Moy, S.S. (2013). Behavioral deficits in an Angelman syndrome model: effects of genetic background and age. Behavioural brain research *243*, 79-90.

Huber, K.M., Gallagher, S.M., Warren, S.T., and Bear, M.F. (2002). Altered synaptic plasticity in a mouse model of fragile X mental retardation. Proc Natl Acad Sci U S A *99*, 7746-7750.

Huguenard, J.R., and McCormick, D.A. (2007). Thalamic synchrony and dynamic regulation of global forebrain oscillations. Trends Neurosci *30*, 350-356.

Jang, H.J., Cho, K.H., Kim, M.J., Yoon, S.H., and Rhie, D.J. (2013). Layer- and cell-type-specific tonic GABAergic inhibition of pyramidal neurons in the rat visual cortex. Pflugers Archiv : European journal of physiology *465*, 1797-1810.

Jiang, B., Huang, S., de Pasquale, R., Millman, D., Song, L., Lee, H.K., Tsumoto, T., and Kirkwood, A. (2010). The maturation of GABAergic transmission in visual cortex requires endocannabinoid-mediated LTD of inhibitory inputs during a critical period. Neuron *66*, 248-259.

Jiang, Y.H., Armstrong, D., Albrecht, U., Atkins, C.M., Noebels, J.L., Eichele, G., Sweatt, J.D., and Beaudet, A.L. (1998). Mutation of the Angelman ubiquitin ligase in mice causes increased cytoplasmic p53 and deficits of contextual learning and long-term potentiation. Neuron *21*, 799-811.

Judson, M.C., Sosa-Pagan, J.O., Delcid, W.A., Han, J.E., and Philpot, B.D. (2013). Allelic specificity of Ube3a expression in the mouse brain during postnatal development. J Comp Neurol.

Kim, W.T., Chang, S., Daniell, L., Cremona, O., Di Paolo, G., and De Camilli, P. (2002). Delayed reentry of recycling vesicles into the fusion-competent synaptic vesicle pool in synaptojanin 1 knockout mice. Proc Natl Acad Sci U S A *99*, 17143-17148.

Kishino, T., Lalande, M., and Wagstaff, J. (1997). UBE3A/E6-AP mutations cause Angelman syndrome. Nat Genet *15*, 70-73.

Koh, T.W., Korolchuk, V.I., Wairkar, Y.P., Jiao, W., Evergren, E., Pan, H., Zhou, Y., Venken, K.J., Shupliakov, O., Robinson, I.M.*, et al.* (2007). Eps15 and Dap160 control synaptic vesicle membrane retrieval and synapse development. The Journal of cell biology *178*, 309-322.

Kuhnle, S., Mothes, B., Matentzoglu, K., and Scheffner, M. (2013). Role of the ubiquitin ligase E6AP/UBE3A in controlling levels of the synaptic protein Arc. Proc Natl Acad Sci U S A *110*, 8888-8893.

Kumar, S.S., and Buckmaster, P.S. (2006). Hyperexcitability, interneurons, and loss of GABAergic synapses in entorhinal cortex in a model of temporal lobe epilepsy. J Neurosci *26*, 4613-4623.

Lee, S., Kruglikov, I., Huang, Z.J., Fishell, G., and Rudy, B. (2013). A disinhibitory circuit mediates motor integration in the somatosensory cortex. Nat Neurosci *16*, 1662-1670.

Lee, S.H., Kwan, A.C., Zhang, S., Phoumthipphavong, V., Flannery, J.G., Masmanidis, S.C., Taniguchi, H., Huang, Z.J., Zhang, F., Boyden, E.S.*, et al.* (2012). Activation of specific interneurons improves V1 feature selectivity and visual perception. Nature *488*, 379-383.

Leung, H.T., and Ring, H. (2013). Epilepsy in four genetically determined syndromes of intellectual disability. Journal of intellectual disability research : JIDR *57*, 3-20.

Lewis, J.D., Meehan, R.R., Henzel, W.J., Maurer-Fogy, I., Jeppesen, P., Klein, F., and Bird, A. (1992). Purification, sequence, and cellular localization of a novel chromosomal protein that binds to methylated DNA. Cell *69*, 905-914.

Low, D., and Chen, K.S. (2010). Genome-wide gene expression profiling of the Angelman syndrome mice with Ube3a mutation. European journal of human genetics : EJHG *18*, 1228-1235.

Luthi, A., Di Paolo, G., Cremona, O., Daniell, L., De Camilli, P., and McCormick, D.A. (2001). Synaptojanin 1 contributes to maintaining the stability of GABAergic transmission in primary cultures of cortical neurons. J Neurosci *21*, 9101-9111.

Lyford, G.L., Yamagata, K., Kaufmann, W.E., Barnes, C.A., Sanders, L.K., Copeland, N.G., Gilbert, D.J., Jenkins, N.A., Lanahan, A.A., and Worley, P.F. (1995). Arc, a growth factor and activity-regulated gene, encodes a novel cytoskeleton-associated protein that is enriched in neuronal dendrites. Neuron *14*, 433-445.

Mabb, A.M., Judson, M.C., Zylka, M.J., and Philpot, B.D. (2011). Angelman syndrome: insights into genomic imprinting and neurodevelopmental phenotypes. Trends Neurosci *34*, 293-303.

Madisen, L., Zwingman, T.A., Sunkin, S.M., Oh, S.W., Zariwala, H.A., Gu, H., Ng, L.L., Palmiter, R.D., Hawrylycz, M.J., Jones, A.R.*, et al.* (2010). A robust and high-throughput Cre reporting and characterization system for the whole mouse brain. Nat Neurosci *13*, 133-140.

Mani, M., Lee, S.Y., Lucast, L., Cremona, O., Di Paolo, G., De Camilli, P., and Ryan, T.A. (2007). The dual phosphatase activity of synaptojanin1 is required for both efficient synaptic vesicle endocytosis and reavailability at nerve terminals. Neuron *56*, 1004-1018.

Marder, E., and Goaillard, J.M. (2006). Variability, compensation and homeostasis in neuron and network function. Nat Rev Neurosci *7*, 563-574.

Margolis, S.S., Salogiannis, J., Lipton, D.M., Mandel-Brehm, C., Wills, Z.P., Mardinly, A.R., Hu, L., Greer, P.L., Bikoff, J.B., Ho, H.Y.*, et al.* (2010). EphB-mediated degradation of the RhoA GEF Ephexin5 relieves a developmental brake on excitatory synapse formation. Cell *143*, 442-455.

Markram, H., Toledo-Rodriguez, M., Wang, Y., Gupta, A., Silberberg, G., and Wu, C. (2004). Interneurons of the neocortical inhibitory system. Nat Rev Neurosci *5*, 793-807.

Marr, D. (1980). Visual information processing: the structure and creation of visual representations. Philosophical transactions of the Royal Society of London Series B, Biological sciences *290*, 199-218.

McCormick, D.A., and Contreras, D. (2001). On the cellular and network bases of epileptic seizures. Annu Rev Physiol *63*, 815-846.

McCurry, C.L., Shepherd, J.D., Tropea, D., Wang, K.H., Bear, M.F., and Sur, M. (2010). Loss of Arc renders the visual cortex impervious to the effects of sensory experience or deprivation. Nat Neurosci *13*, 450-457.

Melone, M., Ciappelloni, S., and Conti, F. (2013). A quantitative analysis of cellular and synaptic localization of GAT-1 and GAT-3 in rat neocortex. Brain structure & function.

Milosevic, I., Giovedi, S., Lou, X., Raimondi, A., Collesi, C., Shen, H., Paradise, S., O'Toole, E., Ferguson, S., Cremona, O.*, et al.* (2011). Recruitment of endophilin to clathrin-coated pit necks is required for efficient vesicle uncoating after fission. Neuron *72*, 587-601.

Minelli, A., Brecha, N.C., Karschin, C., DeBiasi, S., and Conti, F. (1995). GAT-1, a high-affinity GABA plasma membrane transporter, is localized to neurons and astroglia in the cerebral cortex. J Neurosci *15*, 7734-7746.

Miura, K., Kishino, T., Li, E., Webber, H., Dikkes, P., Holmes, G.L., and Wagstaff, J. (2002). Neurobehavioral and electroencephalographic abnormalities in Ube3a maternal-deficient mice. Neurobiol Dis *9*, 149-159.

Morales, B., Choi, S.Y., and Kirkwood, A. (2002). Dark rearing alters the development of GABAergic transmission in visual cortex. J Neurosci *22*, 8084-8090.

Musumeci, S.A., Bosco, P., Calabrese, G., Bakker, C., De Sarro, G.B., Elia, M., Ferri, R., and Oostra, B.A. (2000). Audiogenic seizures susceptibility in transgenic mice with fragile X syndrome. Epilepsia *41*, 19-23.

Nielsen, D.M., Derber, W.J., McClellan, D.A., and Crnic, L.S. (2002). Alterations in the auditory startle response in Fmr1 targeted mutant mouse models of fragile X syndrome. Brain research *927*, 8-17.

Nimchinsky, E.A., Oberlander, A.M., and Svoboda, K. (2001). Abnormal development of dendritic spines in FMR1 knock-out mice. J Neurosci *21*, 5139-5146.

Nomura, Y. (2005). Early behavior characteristics and sleep disturbance in Rett syndrome. Brain & development *27 Suppl 1*, S35-s42.

Okaty, B.W., Miller, M.N., Sugino, K., Hempel, C.M., and Nelson, S.B. (2009). Transcriptional and electrophysiological maturation of neocortical fast-spiking GABAergic interneurons. J Neurosci *29*, 7040-7052.

Osterweil, E.K., Chuang, S.C., Chubykin, A.A., Sidorov, M., Bianchi, R., Wong, R.K., and Bear, M.F. (2013). Lovastatin corrects excess protein synthesis and prevents epileptogenesis in a mouse model of fragile X syndrome. Neuron *77*, 243-250.

Paluszkiewicz, S.M., Olmos-Serrano, J.L., Corbin, J.G., and Huntsman, M.M. (2011). Impaired inhibitory control of cortical synchronization in fragile X syndrome. J Neurophysiol *106*, 2264-2272.

Patel, A.B., Hays, S.A., Bureau, I., Huber, K.M., and Gibson, J.R. (2013). A target cell-specific role for presynaptic Fmr1 in regulating glutamate release onto neocortical fast-spiking inhibitory neurons. J Neurosci *33*, 2593-2604.

Pfeiffer, B.E., and Huber, K.M. (2007). Fragile X mental retardation protein induces synapse loss through acute postsynaptic translational regulation. J Neurosci *27*, 3120-3130.

Phend, K.D., Weinberg, R.J., and Rustioni, A. (1992). Techniques to optimize post-embedding single and double staining for amino acid neurotransmitters. J Histochem Cytochem *40*, 1011-1020.

Philpot, B.D., Espinosa, J.S., and Bear, M.F. (2003). Evidence for altered NMDA receptor function as a basis for metaplasticity in visual cortex. J Neurosci *23*, 5583-5588.

Pi, H.J., Hangya, B., Kvitsiani, D., Sanders, J.I., Huang, Z.J., and Kepecs, A. (2013). Cortical interneurons that specialize in disinhibitory control. Nature *503*, 521-524.

Pinto, L., Goard, M.J., Estandian, D., Xu, M., Kwan, A.C., Lee, S.H., Harrison, T.C., Feng, G., and Dan, Y. (2013). Fast modulation of visual perception by basal forebrain cholinergic neurons. Nat Neurosci *16*, 1857-1863.

Polo, S., Sigismund, S., Faretta, M., Guidi, M., Capua, M.R., Bossi, G., Chen, H., De Camilli, P., and Di Fiore, P.P. (2002). A single motif responsible for ubiquitin recognition and monoubiquitination in endocytic proteins. Nature *416*, 451-455.

Priebe, N.J., and Ferster, D. (2012). Mechanisms of neuronal computation in mammalian visual cortex. Neuron *75*, 194-208.

Qualmann, B., Roos, J., DiGregorio, P.J., and Kelly, R.B. (1999). Syndapin I, a synaptic dynamin-binding protein that associates with the neural Wiskott-Aldrich syndrome protein. Molecular biology of the cell *10*, 501-513.

Ramamoorthy, S., and Nawaz, Z. (2008). E6-associated protein (E6-AP) is a dual function coactivator of steroid hormone receptors. Nuclear receptor signaling *6*, e006.

Riday, T.T. (2013). Cortical experience-dependent plasticity and mesostriatal dopaminergic dysfunction in a mouse model of Angelman syndrome. In Curriculum in Neurobiology (University of North Carolina), pp. 155.

Ross, K.C., and Coleman, J.R. (2000). Developmental and genetic audiogenic seizure models: behavior and biological substrates. Neuroscience and biobehavioral reviews *24*, 639-653.

Rougeulle, C., Glatt, H., and Lalande, M. (1997). The Angelman syndrome candidate gene, UBE3A/E6-AP, is imprinted in brain. Nat Genet *17*, 14-15.

Routh, B.N., Johnston, D., and Brager, D.H. (2013). Loss of Functional A-Type Potassium Channels in the Dendrites of CA1 Pyramidal Neurons from a Mouse Model of Fragile X Syndrome. J Neurosci *33*, 19442-19450.

Rubenstein, J.L., and Merzenich, M.M. (2003). Model of autism: increased ratio of excitation/inhibition in key neural systems. Genes Brain Behav *2*, 255-267.

Sato, M., and Stryker, M.P. (2010). Genomic imprinting of experience-dependent cortical plasticity by the ubiquitin ligase gene Ube3a. Proc Natl Acad Sci U S A *107*, 5611-5616.

Scheffner, M., Huibregtse, J.M., Vierstra, R.D., and Howley, P.M. (1993). The HPV-16 E6 and E6-AP complex functions as a ubiquitin-protein ligase in the ubiquitination of p53. Cell *75*, 495-505.

Simler, S., Hirsch, E., Danober, L., Motte, J., Vergnes, M., and Marescaux, C. (1994). C-fos expression after single and kindled audiogenic seizures in Wistar rats. Neurosci Lett *175*, 58-62.

Skarnes, W.C., Rosen, B., West, A.P., Koutsourakis, M., Bushell, W., Iyer, V., Mujica, A.O., Thomas, M., Harrow, J., Cox, T.*, et al.* (2011). A conditional knockout resource for the genome-wide study of mouse gene function. Nature *474*, 337-342.

Slepnev, V.I., and De Camilli, P. (2000). Accessory factors in clathrin-dependent synaptic vesicle endocytosis. Nat Rev Neurosci *1*, 161-172.

Sloviter, R.S. (1987). Decreased hippocampal inhibition and a selective loss of interneurons in experimental epilepsy. Science *235*, 73-76.

Sohal, V.S., Zhang, F., Yizhar, O., and Deisseroth, K. (2009). Parvalbumin neurons and gamma rhythms enhance cortical circuit performance. Nature *459*, 698-702.

Spencer, C.M., Alekseyenko, O., Serysheva, E., Yuva-Paylor, L.A., and Paylor, R. (2005). Altered anxiety-related and social behaviors in the Fmr1 knockout mouse model of fragile X syndrome. Genes Brain Behav *4*, 420-430.

Stuss, D.P., Boyd, J.D., Levin, D.B., and Delaney, K.R. (2012). MeCP2 mutation results in compartment-specific reductions in dendritic branching and spine density in layer 5 motor cortical neurons of YFP-H mice. PLoS One *7*, e31896.

Sudhof, T.C. (2004). The synaptic vesicle cycle. Annu Rev Neurosci *27*, 509-547.

Tabuchi, K., Blundell, J., Etherton, M.R., Hammer, R.E., Liu, X., Powell, C.M., and Sudhof, T.C. (2007). A neuroligin-3 mutation implicated in autism increases inhibitory synaptic transmission in mice. Science *318*, 71-76.

Taniguchi, H., He, M., Wu, P., Kim, S., Paik, R., Sugino, K., Kvitsiani, D., Fu, Y., Lu, J., Lin, Y*., et al.* (2011). A resource of Cre driver lines for genetic targeting of GABAergic neurons in cerebral cortex. Neuron *71*, 995-1013.

Thibert, R.L., Conant, K.D., Braun, E.K., Bruno, P., Said, R.R., Nespeca, M.P., and Thiele, E.A. (2009). Epilepsy in Angelman syndrome: a questionnaire-based assessment of the natural history and current treatment options. Epilepsia *50*, 2369-2376.

Thibert, R.L., Larson, A.M., Hsieh, D.T., Raby, A.R., and Thiele, E.A. (2013). Neurologic manifestations of Angelman syndrome. Pediatric neurology *48*, 271-279.

Tronche, F., Kellendonk, C., Kretz, O., Gass, P., Anlag, K., Orban, P.C., Bock, R., Klein, R., and Schutz, G. (1999). Disruption of the glucocorticoid receptor gene in the nervous system results in reduced anxiety. Nat Genet *23*, 99-103.

Tuchman, R., Cuccaro, M., and Alessandri, M. (2010). Autism and epilepsy: historical perspective. Brain & development *32*, 709-718.

Turrigiano, G.G., and Nelson, S.B. (2004). Homeostatic plasticity in the developing nervous system. Nat Rev Neurosci *5*, 97-107.

Vierling-Claassen, D., Cardin, J.A., Moore, C.I., and Jones, S.R. (2010). Computational modeling of distinct neocortical oscillations driven by cell-type selective optogenetic drive: separable resonant circuits controlled by low-threshold spiking and fast-spiking interneurons. Frontiers in human neuroscience *4*, 198.

Wallace, M.L., Burette, A.C., Weinberg, R.J., and Philpot, B.D. (2012). Maternal loss of Ube3a produces an excitatory/inhibitory imbalance through neuron type-specific synaptic defects. Neuron *74*, 793-800.

Williams, C.A., Beaudet, A.L., Clayton-Smith, J., Knoll, J.H., Kyllerman, M., Laan, L.A., Magenis, R.E., Moncla, A., Schinzel, A.A., Summers, J.A.*, et al.* (2006). Angelman syndrome 2005: updated consensus for diagnostic criteria. Am J Med Genet A *140*, 413-418.

Wilson, N.R., Runyan, C.A., Wang, F.L., and Sur, M. (2012). Division and subtraction by distinct cortical inhibitory networks in vivo. Nature *488*, 343-348.

Wood, L., Gray, N.W., Zhou, Z., Greenberg, M.E., and Shepherd, G.M. (2009). Synaptic circuit abnormalities of motor-frontal layer 2/3 pyramidal neurons in an RNA interference model of methyl-CpG-binding protein 2 deficiency. J Neurosci *29*, 12440-12448.

Yan, Q.J., Asafo-Adjei, P.K., Arnold, H.M., Brown, R.E., and Bauchwitz, R.P. (2004). A phenotypic and molecular characterization of the fmr1-tm1Cgr fragile X mouse. Genes Brain Behav *3*, 337-359.

Yashiro, K., Riday, T.T., Condon, K.H., Roberts, A.C., Bernardo, D.R., Prakash, R., Weinberg, R.J., Ehlers, M.D., and Philpot, B.D. (2009). Ube3a is required for experience-dependent maturation of the neocortex. Nat Neurosci *12*, 777-783.

Ye, Z., McGee, T.P., Houston, C.M., and Brickley, S.G. (2013). The contribution of delta subunit-containing GABAA receptors to phasic and tonic conductance changes in cerebellum, thalamus and neocortex. Frontiers in neural circuits *7*, 203.

Yizhar, O., Fenno, L.E., Prigge, M., Schneider, F., Davidson, T.J., O'Shea, D.J., Sohal, V.S., Goshen, I., Finkelstein, J., Paz, J.T.*, et al.* (2011). Neocortical excitation/inhibition balance in information processing and social dysfunction. Nature *477*, 171-178.